OUKA
The University of Osaka
Institutional Knowledge Archive

Title	Enhancement of Light-Matter Interaction in Two-dimensional Exciton with Huygens Metasurface
Author(s)	Chen, Dingwei
Citation	大阪大学, 2026, 博士論文
Version Type	VoR
URL	https://doi.org/10.18910/105436
rights	
Note	

The University of Osaka Institutional Knowledge Archive : OUKA

https://ir.library.osaka-u.ac.jp/

The University of Osaka

Doctoral Dissertation

Enhancement of Light–Matter Interaction in Two-Dimensional Exciton with Huygens Metasurface

CHEN DINGWEI

January 2026

Department of Applied Physics,

Graduate School of Engineering,

The University of Osaka

Abstract

Two-dimensional (2D) transition metal dichalcogenides (TMDCs) represent a class of atomically thin semiconductors with tunable band structures, high carrier mobility, strong spin–orbit coupling, and remarkable excitonic characteristics. Compared with their bulk counterparts, 2D TMDCs exhibit a transition to direct bandgaps with giant exciton binding energies and efficient exciton–photon interactions. These unique features make them promising for optoelectronic and quantum photonic devices, including light emitters, detectors, and valleytronic elements. Nevertheless, their ultrathin thickness imposes an inherent limitation: the extremely small interaction volume leads to intrinsically weak absorption and emission, typically below the threshold required for practical device applications.

This dissertation aims to address this limitation by introducing a multiple coupling strategy that integrates degenerate critical coupling (DCC) and intermediate coupling between Mie resonances in dielectric metasurfaces and excitons in monolayers TMDCs. By establishing and experimentally validating this framework, the work demonstrates a substantial enhancement of both absorption and photoluminescence (PL) in 2D materials.

The optical properties of Mie resonators are first analyzed in detail, focusing on the electric and magnetic dipole (ED and MD) modes and their spectral degeneracy under the DCC condition. DCC enables perfect absorption when the radiative loss rate is matched to the intrinsic loss rate. While this phenomenon has been mainly achieved in the near-infrared and visible regions in previous studies, the present work extends it into the violet spectral range by employing rotated dielectric resonators. This extension verifies the universality of the DCC condition in high-index dielectric materials and expands its applicability to shorter wavelengths.

Building on this understanding, the dissertation further investigates hybrid photonics systems composed of monolayer TMDCs integrated with Mie-type dielectric metasurfaces. Monolayer WS_2 is employed as a representative 2D semiconductor in the visible regime, where its A-exciton resonance around 615 nm dominates the optical response. Both numerical simulations and experimental measurements reveal an intermediate coupling regime between the exciton and Mie modes, characterized by a Rabi splitting of approximately 81 meV and significant enhancement in both absorption and emission. The system exhibits a maximum absorptivity exceeding 0.78 and a PL intensity enhancement of over 18-fold, demonstrating efficient energy exchange between the excitons and Mie resonances. This work identifies and experimentally confirms the physical origin of Miexcitons—the hybridized quasi-particles arising from intermediate Mie–exciton coupling.

By tuning the structural parameters, the ED Mie mode can be brought into near-resonance with the excitonic transition, establishing the intermediate coupling that strengthens light–matter interaction. When the ED and MD modes are spectrally overlapped, these modes act cooperatively to further amplify the absorption and emission enhancement. Moreover, by adjusting the metasurface geometry, the Mie-resonance wavelength can be continuously tuned from the ultraviolet to the infrared, enabling broad compatibility with various 2D materials possessing different excitonic energies.

In conclusion, this dissertation establishes a comprehensive framework for Mie resonance–based exciton enhancement through DCC and intermediate coupling, across from violet to visible wavelengths range. The findings deepen the physical insight into hybrid 2D–dielectric photonic systems and provide practical design principles for future optoelectronic and quantum photonic devices that exploit the extraordinary optical properties of atomically thin semiconductors.

Contents

Abstract I

Introduction 1

Chapter 1 Introduction of two-dimensional materials 5

1.1 What is 2D materials? 6
1.2 2D Transition metal dichalcogenides 7
1.3 Preparation method of 2D TMDCs 10
1.4 Excitons 11
1.5 Optical properties of 2D WS_2: Absorption 14

Chapter 2 Optical properties of Mie resonators 19

2.1 Metasurface Overview 20
2.2 Mie scattering 22
2.3 Optical cavity of Mie resonators and Purcell effect 25
2.4 Degenerate critical coupling (DCC) 26
2.5 DCC in the violet light range 27
2.6 DCC in the visible light range 32

Chapter 3 Intermediate coupling in Miexcitons 37

3.1 Different effects of Mie modes on 2D WS_2 38
3.2 Strong coupling in light-matter interaction: Rabi splitting 39
3.3 Intermediate coupling 42
3.4 Enhancement effect of MD mode 44
3.5 Enhancement effect of ED mode: Miexciton 46
3.6 Enhancement effect of MD & ED modes 48

Chapter 4 Hybrid 2D material-dielectric 55

4.1 Transfer method of 2D TMDCs 56
4.2 Basic characterization of hybrid system 59
4.3 Absorption measurement of metasurface 64
4.4 Absorption measurement of WS_2-metasurface 67
4.5 Emission measurement of WS_2-metasurface 71
4.6 Extension for applications 78

Conclusion 81

Appendix 83

References 85

Acknowledgement 103

List of Publications 105

Introduction

Transition metal dichalcogenides (TMDCs) are among the most attractive two-dimensional (2D) materials owing to their adjustable bandgaps, high carrier mobility, strong spin–orbit coupling, and exceptional optoelectronic properties [1,2]. In the monolayer limit, most TMDCs undergo an indirect-to-direct bandgap transition and exhibit pronounced excitonic effects due to reduced dielectric screening and strong Coulomb interactions, enabling highly efficient exciton–photon coupling [3,4]. These distinctive properties render monolayer TMDCs promising candidates for a wide range of optoelectronic and valleytronic applications, including semiconductor lasers, light-emitting diodes, photodetectors, and information processing devices [5–8]. With the rapidly increasing demand for miniaturized, multifunctional, and high-performance optoelectronic systems, the development and integration of atomically thin TMDCs have attracted extensive attention.

Despite these advantages, a fundamental limitation of atomically thin TMDCs lies in their intrinsically weak optical absorption, typically in the range of only 2–12% for a free-standing monolayer [9–11]. The extremely small interaction volume severely restricts light–matter coupling efficiency and thus hampers their practical implementation in high-performance optoelectronic devices. To overcome this bottleneck, various strategies have been proposed to enhance the light–matter interaction and improve the optical absorption of monolayer TMDCs [12–16].

One widely adopted strategy is to integrate TMDCs with metallic or dielectric micro- and nanostructures, such as optical microcavities, nanohole arrays, and grating structures, to exploit plasmonic or photonic resonances for absorption enhancement [17–21]. However, in many of these designs, TMDCs are typically embedded within multilayer cavities, which significantly increases fabrication complexity and optical loss [9,21]. Moreover, a considerable fraction of reported enhancement schemes suffers from limitations such as cryogenic operating conditions, strong sensitivity to photonic environment tuning, or poor scalability for large-area integration [16,22] Among them, plasmonic nanostructures have been extensively studied for enhancing light–matter interactions in TMDCs by utilizing localized surface plasmon resonances to provide strong near-field confinement and field enhancement [23–25]. Although plasmonic platforms offer remarkable enhancement capabilities, their intrinsic Ohmic losses, relatively low-quality factors, and limited compatibility with large-scale integration significantly constrain their practical applicability [26,27] These drawbacks have stimulated growing interest in low-loss dielectric nanophotonic platforms as scalable alternatives.

In dielectric systems, low-loss optical confinement combined with high geometric tunability provides a promising route to enhancing light–matter interactions in monolayer TMDCs [28]. Recent studies have demonstrated Rabi splitting between TMDC excitons and high-Q dielectric resonances, such as quasi-bound states in the continuum, by constructing TMDC-based metasurfaces [29–31]. However, most of these demonstrations rely on bulk-like or embedded TMDCs, and the experimental realization of embedded structures is generally more challenging and less flexible for practical integration [32].

Motivated by the need for a low-loss, scalable, and universal absorption-enhancement platform for 2D TMDCs, this dissertation focuses on the realization and physical understanding of coupling in monolayer TMDCs integrated with all-dielectric metasurfaces. In this work, a crystalline silicon (c-Si) Huygens metasurface is designed as a robust photonic platform to enhance both the absorption and emission of a monolayer tungsten disulfide (WS_2), taken as a representative TMDCs. The absorption enhancement is primarily attributed to the intermediate coupling between WS_2 excitons and the electric dipole (ED) Mie resonance, forming Miexciton. Furthermore, the coupling strength is significantly amplified through degenerate critical coupling (DCC) between the ED and magnetic dipole (MD) modes, leading to pronounced absorption enhancement.

This dissertation is organized as follows.

Chapter 1 introduces the fundamental physical properties of 2D TMDCs, including their electronic band structures, excitonic characteristics, representative fabrication methods, and optical behaviors, providing the material foundation for the subsequent studies.

Chapter 2 presents the design principles and optical characteristics of dielectric Mie resonators and Huygens metasurfaces, with particular emphasis on electric and magnetic dipole resonances, degenerate critical coupling, and their roles in light manipulation and absorption enhancement.

Chapter 3 investigates the optical response of a WS_2 monolayer integrated with Si Mie resonators, focusing on the intermediate coupling regime between excitonic transitions and ED modes. The separate and combined contributions of ED and MD modes are analyzed in detail, and the emergence of Miexciton hybrid states is demonstrated.

Chapter 4 systematically studies the experimental realization of the WS_2–Huygens metasurface system, including monolayer transfer, structural and optical characterizations, absorption and PL enhancement, and power-dependent coupling behaviors. The robustness of the enhancement against incident angle variation and its applicability to other TMDC materials are also verified.

Through these investigations, this dissertation establishes a low-loss, scalable, and versatile all-dielectric platform for enhancing exciton–photon interactions in 2D TMDCs, providing

fundamental insights and practical guidance for the development of next-generation integrated optoelectronic and nanophotonic devices.

Chapter 1 Introduction of two-dimensional materials

Two-dimensional (2D) TMDCs are an important class of atomically thin semiconductors that feature tunable band structures, high carrier mobility, strong spin–orbit coupling, and excellent optoelectronic properties. In the monolayer limit, they transition into direct-bandgap materials with pronounced excitonic effects, enabling highly efficient exciton–photon interactions. These characteristics make them strong candidates for advanced optoelectronic systems, including light emitters, photodetectors, and valleytronic devices.

In this chapter, we introduce the fundamental properties of 2D TMDCs and their excitonic characteristics, followed by an overview of representative fabrication methods and optical behaviors. The atomic thickness of these materials imposes an inherent constraint: the extremely small interaction volume leads to weak light absorption, which is often insufficient for practical device applications. This limitation provides a key motivation for integrating TMDCs with metasurfaces to enhance and tailor their optical responses.

1.1 What is 2D materials?

In 2004, Andre Geim and Kostya Novoselov successfully exfoliated a stable monolayer carbon film graphene from bulk graphite using simple adhesive tape [33]. The low-cost fabrication method and graphene's extraordinary properties immediately triggered an explosive wave of academic interest, marking the beginning of the era of 2D materials. Only six years later, Geim and Novoselov were awarded the Nobel Prize in Physics, underscoring the profound importance of 2D materials in 21st-century materials research. Beyond graphene, the family of known 2D materials now includes transition metal dichalcogenides (TMDCs), MXenes, metal–organic frameworks, black phosphorus, and hexagonal boron nitride (h-BN), among others [34], as illustrated in Fig. 1.1.

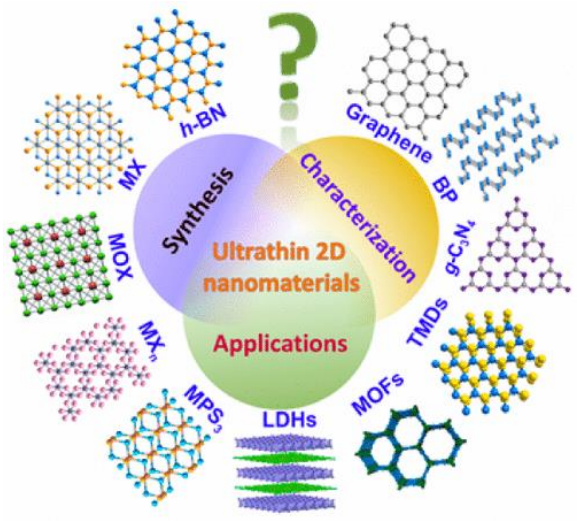

Figure 1.1 2D nanomaterials and their structure [34].

Due to their unique structural characteristics, 2D materials possess many novel physical properties compared to bulk materials:

a) **Extremely high surface-to-volume ratio.**

In colloidal dispersions, nearly all atoms in a 2D material are exposed, giving them advantages in catalytic reactions that bulk materials cannot match [35]. In solid-state systems, transfer techniques allow 2D materials to modify surface properties of chips with negligible thickness change, such as in the case of graphene-based transparent electrodes [36].

b) **Atomically thin, stable monolayers without dangling bonds.**

Because their surfaces are free of dangling bonds, 2D materials interact with other materials via van der Waals forces, eliminating lattice-mismatch constraints. Layer-by-

layer stacking of different 2D materials enables diverse device functionalities within an ultrathin footprint [37–39].

c) **Layer-dependent electronic structures.**
For example, monolayer MoS_2 is a direct-bandgap semiconductor, whereas multilayer MoS_2 exhibits an indirect bandgap that decreases as the number of layers increases [3,40].

d) **Highly tunable physical properties.**
Different classes of 2D materials exhibit distinct electronic behaviors, which can be further modulated through doping [41], layer-number control [42], strain engineering [43], and more. Similarly, their optical [40] and mechanical properties [44] can be tuned for specific applications, offering researchers vast design flexibility.

e) **Mechanical flexibility and compatibility with wearable and bio-integrated devices.**
Owing to their atomic thinness and exceptional in-plane mechanical strength, many 2D materials can withstand significant bending and stretching without performance degradation. This flexibility makes them ideal for next-generation wearable biosensors and conformal bio-interfaces capable of detecting physiological signals directly on soft, curved biological tissues [45,46].

The above summary covers only some common properties of 2D materials. Many others exhibit additional exotic characteristics, including topological insulating behavior [47], superconductivity [48], and more.

1.2 2D Transition metal dichalcogenides

Since the discovery of graphene, extensive efforts have been devoted to exploring low-dimensional layered materials. Among them, TMDCs have attracted significant attention in recent years. TMDCs refer to compounds composed of a transition metal and a chalcogen element (S, Se, or Te), as illustrated in Figure 1.2(a). They predominantly exhibit two structural motifs: a trigonal prismatic structure with D_{3h} point-group symmetry and an octahedral structure with C_{3v} symmetry. The corresponding monolayer configurations are shown in Figures 1.2(b) and (c).

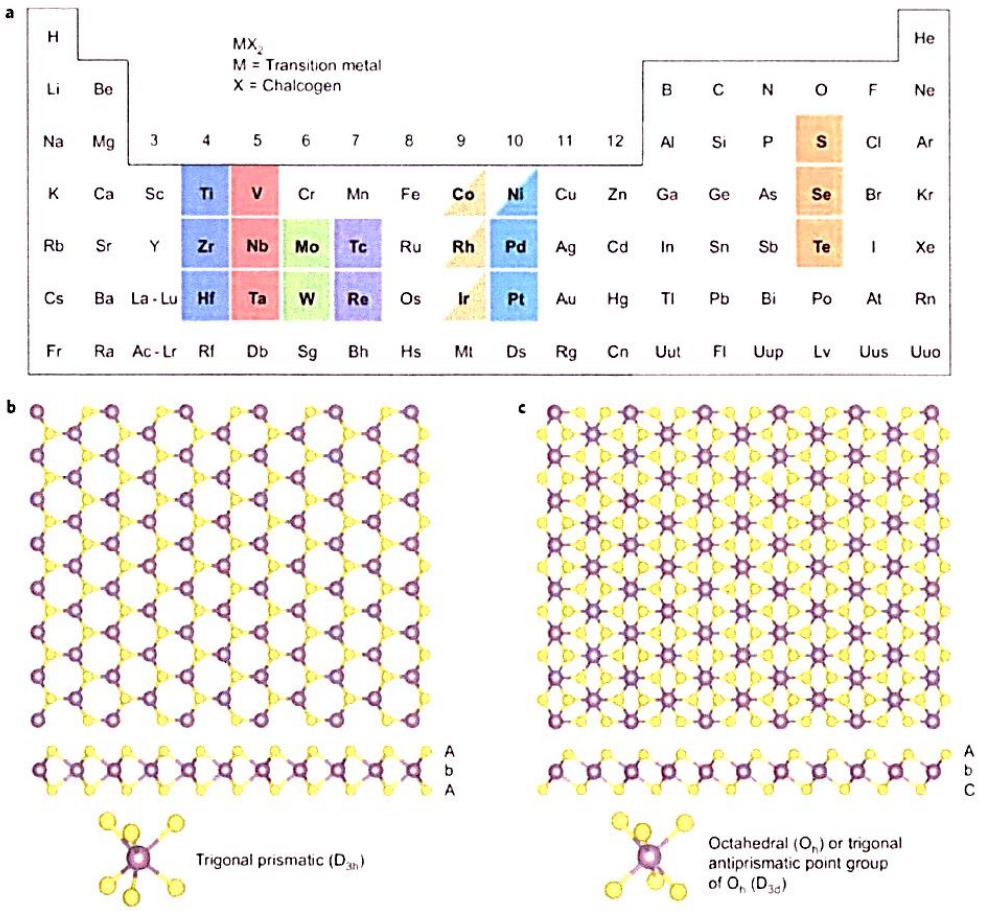

Figure 1.2 (a) Constituent elements of TMDCs; (b) and (c) two cellular structures of TMDCs respectively [49].

Individual TMDC layers are held together by van der Waals interactions. Differences in stacking order give rise to three structural polytypes—1T, 2H, and 3R—as shown in Figure 1.3. In this notation, the number denotes the number of layers in the basic stacking unit, and the letters represent trigonal, hexagonal, and rhombohedral arrangements. Variations in composition and crystal structure strongly influence the material properties. Most 2H-type TMDCs exhibit stable semiconducting behavior. The first monolayer TMDC semiconductor obtained experimentally was monolayer MoS_2, which was isolated by mechanical exfoliation in 2005 [50]. Owing to their unique optical and electronic characteristics, semiconducting TMDCs have rapidly become a major focus of research.

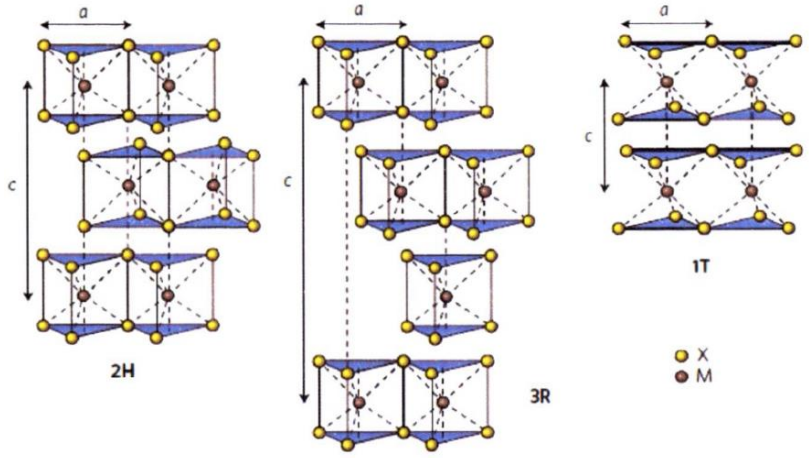

Figure 1.3 Common crystal structure of TMDCs [51].

Due to quantum confinement and changes in symmetry, the band structure of TMDCs varies with the number of layers. In particular, the bandgap decreases as the thickness increases, and most TMDC semiconductors undergo a transition from an indirect bandgap in the multilayer form to a direct bandgap in the monolayer limit [52]. In addition, the bandgap becomes smaller as the atomic number of the chalcogen element increases, as shown in Figure 1.4.

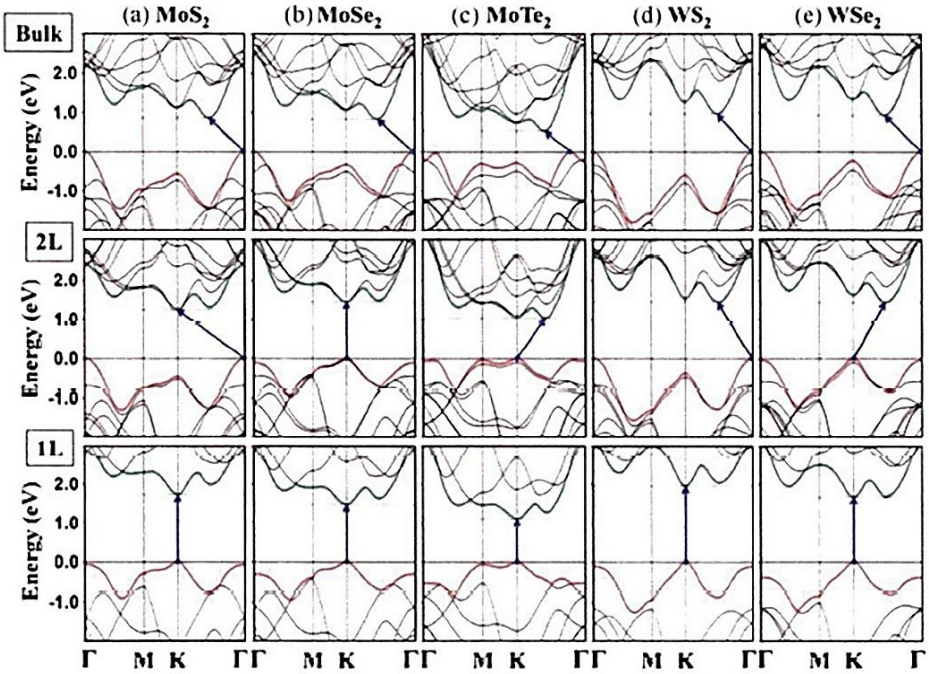

Figure 1.4 The band structure of a typical TMDCs semiconductor varies with the number of layers [52].

1.3 Preparation method of 2D TMDCs

Low-dimensional magnetic materials exhibit a wide range of properties that differ substantially from those of conventional materials. Once large-scale production becomes feasible, these materials may significantly influence the development of many optical, electronic, and magnetic devices. As a result, the synthesis and fabrication of low-dimensional materials have become crucial topics of research [53–57]. Over the years, fabrication techniques have advanced considerably, and many approaches are now available, each with its own advantages and limitations. These techniques are generally categorized into two major classes: bottom-up and top-down. As the names suggest, bottom-up methods build bulk materials from atoms or small molecules, while top-down methods break bulk crystals into thin layered structures. Representative examples include chemical vapor deposition for bottom-up growth and mechanical exfoliation for top-down fabrication.

Mechanical exfoliation, developed in 2004 [33], is the earliest and most widely used method for producing low-dimensional layered materials [58–62]. Novoselov and co-workers demonstrated that monolayer graphene can be isolated from bulk graphite using a very simple procedure. The modern version of this technique involves repeatedly attaching and peeling a piece of adhesive tape, such as Scotch tape, from the bulk crystal. Each peeling step produces thinner flakes. After several repetitions, thin layers become visible under an optical microscope. Because the adhesion between tape and layered materials is typically stronger than the adhesion to a silicon (Si) substrate, an additional transfer step is needed. The exfoliated flakes are first moved onto a transparent and flexible polydimethylsiloxane (PDMS) film and then transferred to the desired substrate. Mechanical exfoliation yields flakes with very high crystallinity and low defect density. However, the thickness and lateral size of the samples cannot be well controlled, and large-area production is not practical. These limitations have motivated the development of alternative fabrication techniques [58,63–67].

Liquid-phase exfoliation extends the concept of mechanical exfoliation. In this method, the bulk layered material is dispersed in a solvent that provides suitable solubility, dispersion stability, and a surface energy close to that of the crystal. High-power ultrasonication is then applied to exfoliate thin layers from the bulk structure. The resulting dispersion can be purified and used to prepare thin-film samples through filtration or spray coating [68]. Compared with mechanical exfoliation, this approach offers significantly higher throughput and enables large-scale production. However, the quality of the resulting flakes is lower, and solvent contamination must be considered. For materials that are prone to oxidation or degradation, finding an appropriate solvent becomes particularly challenging.

Vapor-phase deposition is a well-established technique in the semiconductor industry for growing thin-film materials. In principle, the method deposits high-temperature vapor species onto a substrate through condensation. Vapor-phase techniques are divided into physical vapor deposition (PVD) and chemical vapor deposition (CVD), depending on whether a chemical reaction occurs during the process.

PVD operates in a vacuum environment. A low-pressure, high-current arc discharge causes the target material to evaporate and form a vapor, which is then ionized by the discharge. Under an applied electric field, the ionized species accelerate toward the substrate and condense into a thin film. Magnetron sputtering, the main PVD method used in this work, follows this principle. In a vacuum chamber, an inert gas such as argon is introduced. A voltage is applied between the target and the substrate, ionizing the argon gas and forming a plasma. High-energy argon ions bombard the target material, ejecting atoms that then travel through the chamber and deposit on the substrate. PVD produces high-quality thin films, but large-scale production remains challenging and the fabrication cost is relatively high. As a result, it is still used primarily for laboratory-scale research.

1.4 Excitons

The concept of the exciton was introduced in studies of optical absorption in semiconductors. An exciton is a bound electron–hole pair formed through the Coulomb interaction between an electron and a hole [69]. Excitons participate in both absorption and emission processes in semiconductor materials. Analyzing exciton behavior provides deeper insight into optical absorption mechanisms and supports the development of new photovoltaic and optoelectronic devices.

Excitons may form through two main pathways: (i) direct photoexcitation with the simultaneous emission of a phonon, and (ii) bimolecular formation through the direct recombination of an electron and a hole. The attractive interaction between the electron and the hole lowers the total energy of the system, and the energy reduction is referred to as the exciton binding energy. Excitons are bosons, and at low temperatures they can condense into a new quantum phase known as the Bose–Einstein condensate state. Because excitons undergo collisions with other excitons and interact with phonons and crystal defects, their coherence is inherently limited.

Excitons can be categorized using different criteria. One common classification is based on the size of the exciton Bohr radius relative to the lattice constant as shown in Fig. 1.5. Wannier

excitons have Bohr radii much larger than the lattice constant [70], so the exciton can be treated as an independent quasiparticle whose internal structure resembles that of a hydrogen atom [71]. In contrast, Frenkel excitons have Bohr radii smaller than or comparable to the lattice constant. Their formation corresponds to an electronic excitation localized within a single atom or molecular site [71].

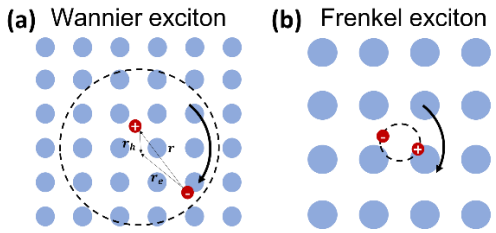

Figure 1.5 (a) Wannier exciton and (b) Frenkel exciton.

This work mainly focuses on Wannier excitons, because in most semiconductor materials the exciton Bohr radius is relatively large, as shown in Fig. 1.5(a). The Wannier exciton theory is introduced below. By considering the individual kinetic energies of the electron and the hole, together with their mutual interaction, the exciton Hamiltonian can be written as follows.

$$\hat{H} = -\frac{\hbar^2\nabla_e^2}{2m_e} - \frac{\hbar^2\nabla_h^2}{2m_h} + V(r_e - r_h) \tag{1.1}$$

where r_e and r_h denote the position vectors of the electron and hole, respectively, and ∇_e^2 and ∇_h^2 are the Laplacian operators acting on r_e and r_h. Here, m_e and m_h are the electron and hole effective masses. $\hbar$ is the reduced Planck constant, defined as $\hbar = h/2\pi$. The interaction potential V(r) describes the screened Coulomb attraction between the electron and hole. A center-of-mass frame is then adopted, in which the Hamiltonian is separated into a center-of-mass part and a relative-motion part. The center-of-mass coordinate and the relative coordinate are defined as

$$R = -\frac{m_e r_e + m_h r_h}{m_e + m_h}, r = r_e - r_h \tag{1.2}$$

After defining the total mass of the center-of-mass motion $M = m_e + m_h$ and the reduced mass $\mu = m_e m_h/M$, under the Born–Oppenheimer approximation in the center-of-mass frame, the motion of the electron–hole pair can be separated into a center-of-mass part and a relative-motion part as follows.

$$\left[-\frac{\hbar^2\nabla_R^2}{2M} - \frac{\hbar^2\nabla_r^2}{2\mu} + V(r)\right]\Psi = E\Psi \tag{1.3}$$

The relative and center-of-mass motions can be decoupled, so the relative-motion part can be written independently as follows.

$$\left[\frac{\hbar^2\nabla_r^2}{2\mu}+V(r)\right]\psi=\epsilon_b\psi \tag{1.4}$$

Among them, ϵ_b is the exciton binding energy. When V is absent, the attractive interaction between the electron and the hole leads to a negative ground-state binding energy, meaning that the formation of an exciton lowers the total energy of the system. By analogy to the hydrogen atom, the exciton binding energy is given by

$$E_{ex}=-\frac{e^2}{2a_{ex}\epsilon_0 n^2}+\frac{\hbar^2k^2}{2(m_e+m_h)},a_{ex}=-\frac{\hbar^2\epsilon_0}{e^2m_r} \tag{1.5}$$

In the center-of-mass frame, the exciton behaves as a whole, and its center-of-mass momentum remains constant and travels in a straight line until it undergoes scattering with phonons, impurities, other excitons, or free carriers.

The band structure of TMDCs undergoes significant changes as the number of layers varies. However, the A and B exciton transition energies at the K/K′ valleys remain essentially unchanged, as illustrated in Fig. 1.6. This behavior arises because, when the material thickness decreases—particularly upon reaching the monolayer limit—strong quantum confinement begins to emerge and the dielectric screening experienced by the exciton becomes markedly reduced. The reduction in screening increases the exciton binding energy. At the same time, this change in binding energy is compensated by the accompanying modification of the electronic band structure. As a result, the net A and B exciton transition energies remain nearly constant across different thicknesses.

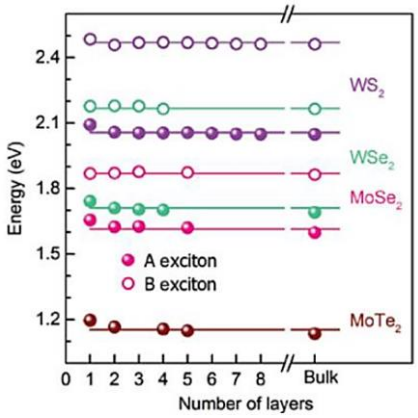

Figure 1.6 Relation between typical TMDCs semiconductor A, B exciton transition energy and layer numbers [72].

When the thickness approaches the monolayer limit, strong quantum confinement emerges along the out-of-plane direction in TMDCs monolayers. As a result, the electronic band structure

at the K and K′ valleys evolve from an indirect bandgap to a direct bandgap [73,74]. This transition significantly enhances optical transitions and leads to pronounced PL emission, a behavior that is rarely observed in their bulk counterparts. Consequently, TMDCs hold considerable promise for applications in various optoelectronic devices.

In addition, spin–orbit coupling [75,76] together with broken inversion symmetry lifts the degeneracy at the Dirac points, opening a valley-dependent bandgap and creating the characteristic upper and lower valley subbands [77]. The associated Dirac fermions acquire finite effective masses, which enables the formation of excitons. Under this framework, the Hamiltonian describing the electronic structure of typical TMDC monolayers at the K and K′ valleys can be expressed in the following form [77]:

$$\widehat{H} = at\left(\tau k_x \hat{\sigma}_x + k_y \hat{\sigma}_y\right) + \frac{\Delta}{2}\hat{\sigma}_z - \lambda\tau\frac{\hat{\sigma}_z - 1}{2}\hat{s}_z \tag{1.6}$$

where a is the lattice constant, t is the effective transition energy, $\tau = \pm 1$τ=±1 labels the K and K′ valleys, and (k_x, k_y) are the in-plane wavevector components measured from the valley center. $\hat{\sigma}_{x,y,z}$ are Pauli matrices acting on the band pseudospin basis, and Δ denotes the intrinsic bandgap. λ represents the spin–orbit coupling strength, while $\hat{s}_z$ is the Pauli matrix corresponding to the electron spin degree of freedom. The last term describes the valley-dependent spin splitting induced by spin–orbit coupling. The first and second terms in the Hamiltonian correspond to the Weyl-type contributions. Here, *at* (*at* = Lattice constant × Transition energy) characterizes the in-plane electronic structure of the material and can be derived from the symmetry of the wavevector group C_{3h} at the K point of the Brillouin zone [77]. The third term represents the intrinsic spin–orbit coupling. 2D TMDCs exhibit pronounced excitonic effects, with exciton binding energies ranging from approximately 0.3 to 1 eV [78,79].

1.5 Optical properties of 2D WS_2: Absorption

The optical characteristics of the hybrid system were evaluated with a three-dimensional finite-difference time-domain approach using a commercial electromagnetic analysis package (Lumerical Solutions, Inc.). In all simulations, a broadband plane-wave source was employed. The electric field of the excitation was oriented along the y axis in order to selectively excite the resonant modes that are relevant to the system under investigation. To record the reflected signal, a frequency-domain power monitor was positioned above the illumination plane. Another monitor was placed below the complete stack consisting of the monolayer transition metal dichalcogenide and the dielectric Mie resonator to quantify the transmitted component.

To ensure that the spatial distribution of the electromagnetic fields was captured with sufficient accuracy, a locally refined mesh region was introduced around the 2D material and the resonator. The side length of each Yee cell in this region was set to approximately 1.6 nm, which is small enough to resolve the rapid field variations that occur near the atomically thin semiconductor. The monolayer WS_2 film was aligned conformally with the upper surface of the resonator structure to reflect the actual device geometry.

In the direction normal to the substrate, perfectly matched layers were implemented as absorbing boundaries so that outgoing waves could exit the simulation domain without generating artificial reflections. Since the incident field is polarized in the y direction, anti-symmetric boundary conditions were applied along this axis. Symmetric conditions were applied along the x direction to reflect the mirror symmetry of the structure. This combination of symmetry planes significantly reduces the required computational domain. As a result, the total memory demand and simulation time decrease by roughly a factor of four when compared with models that rely solely on periodic boundaries.

The total absorption of each configuration was obtained from one minus the sum of the reflectance and transmittance. We use WS_2 as a representative material to investigate the fundamental properties of 2D TMDCs. The refractive index values used for the WS_2 monolayer film were derived from experimentally measured optical permittivity as shown in Fig. 1.7.

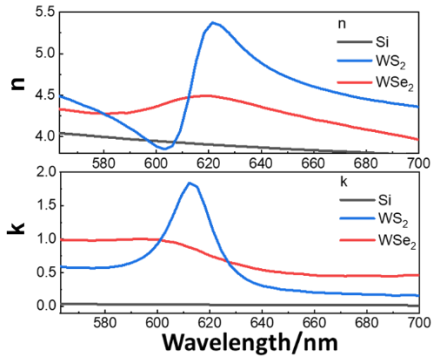

Figure 1.7 Refractive index *n* and extinction coefficient *k* of WS_2, WSe_2, and Si [80,81].

Using these parameters, we calculated the absorption spectra of monolayer WS_2 in two representative geometries to allow direct comparison as shown in Fig. 1.8. The first case corresponds to a suspended situation where the monolayer is surrounded by air. The resulting spectrum exhibits a maximum absorption close to 0.10 at approximately 615 nm. The relatively large peak value can be attributed to the absence of substrate related losses and interference effects.

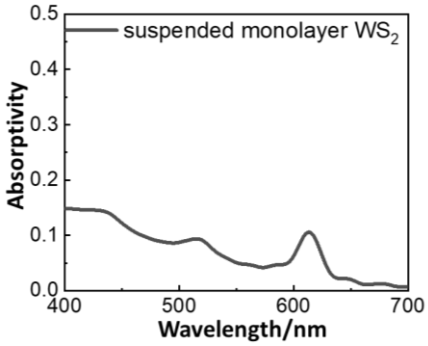

Figure 1.8 Absorption spectrum of suspended monolayer WS_2.

In contrast, when the monolayer lies directly on a Si substrate, evaluating its intrinsic absorption is more complicated. A simple subtraction between the absorption of the substrate alone and that of the substrate combined with the WS_2 layer is insufficient. This method does not correctly account for near field interactions, back reflected fields or other nanoscale optical coupling mechanisms that alter energy flow within the structure. To extract a more reliable representation of the absorption contributed specifically by the WS_2 monolayer, we adopted a power-monitor-based (PB) extraction method [82].

The reflection and transmission spectra were obtained through frequency-domain power (FDP) monitors positioned at selected locations within the simulation domain. These monitors record the electromagnetic power passing through their planes as a function of wavelength, allowing accurate evaluation of the transmitted and reflected components. Additional information on the operation of these monitors can be found in the Lumerical documentation. To determine the absorption associated with individual components of the structure, multiple frequency-domain power monitors were placed at the interfaces surrounding each material layer, as illustrated in Fig. 1.9. By comparing the optical power passing through the FDP monitor placed above a material layer with that recorded by the FDP monitor located immediately below it, the net power loss within that region can be obtained. This difference directly corresponds to the wavelength-dependent absorption of the Si resonator or the WS_2 monolayer. In other words, the intrinsic absorption of each component is determined from the reduction in transmitted power as light propagates between the two monitor planes.

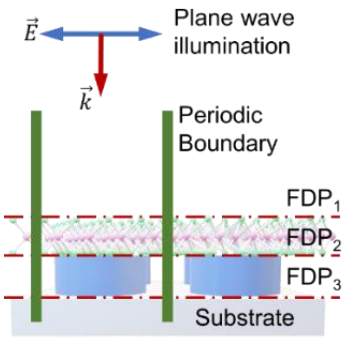

Figure 1.9 FDTD analysis of the absorption contributions within each component of the heterostructure. The diagram illustrates the configuration of the simulation domain. The electric field and wavevector are denoted by $\vec{E}$ and $\vec{k}$, respectively. The labels FDPx mark the locations of the frequency-domain power monitors used to evaluate energy flow throughout the structure.

After applying the PB extraction procedure, we were able to isolate the intrinsic absorption of the monolayer, effectively removing the influence of the underlying Si substrate. The computed spectrum of the full WS_2 on Si structure yields a peak absorption of around 0.04 at approximately 615 nm as summarized in Fig. 1.10 and serve as a reference for later discussions of light–matter interactions in the coupled Mie–exciton system.

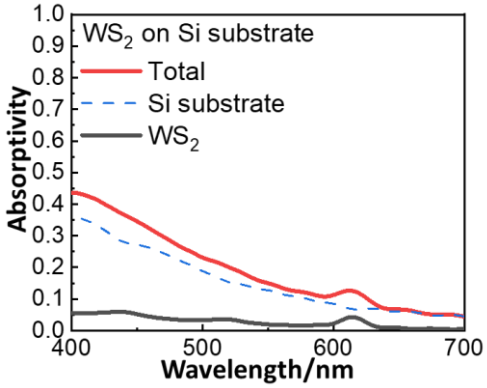

Figure 1.10 Decomposed absorption spectra of WS_2 and Si substrate.

Chapter 2 Optical properties of Mie resonators

This chapter systematically investigates the physical mechanism and design principles of all-dielectric perfect absorbers based on degenerate critical coupling (DCC). Starting from the fundamental theory of Mie resonances in high-index dielectric nanostructures, the electric dipole (ED) and magnetic dipole (MD) modes supported by Si Mie resonators are analyzed in detail. By engineering the geometrical parameters and relative spectral positions of these modes, their radiative and absorptive loss rates are precisely controlled to satisfy the DCC condition.

Through numerical simulations, perfect absorption originating from the DCC of the ED and MD modes is demonstrated. The influence of structural parameters, particularly the resonator height and in-plane rotation angle, on the resonance wavelengths and mode linewidths is clarified. Fabrication-induced deviations and their impact on absorption performance are systematically analyzed, and practical strategies for proximity effect correction and process optimization are proposed. These results establish an experimentally feasible dielectric Huygens metasurface platform capable of achieving near-unity absorption under realistic conditions, providing a solid electromagnetic and fabrication foundation for the exciton–metasurface hybrid systems investigated in subsequent chapters.

2.1 Metasurface Overview

With the continuous progress of optical research and the rapid development of micro-/nano-fabrication technologies, the performance requirements for optical systems have been steadily rising. On the one hand, we aim to integrate more optical components into compact optical architectures; on the other hand, we expect each component to deliver increasingly complex functionalities. As a result, the bulky size of traditional optical elements and the intrinsic limitations of conventional materials have gradually become major bottlenecks restricting the advancement of optical technologies.

Metamaterials are artificial media formed by periodic arrangements of subwavelength metallic or dielectric structures. Through resonant coupling with the electric or magnetic field of incident electromagnetic waves, metamaterials exhibit material responses that are unavailable in naturally occurring substances, enabling a variety of unconventional electromagnetic phenomena and functions. In electromagnetism, permittivity and permeability are the two most fundamental parameters characterizing a material's electromagnetic properties, describing its interactions with electric and magnetic fields, respectively. A material parameter space can be constructed according to the signs of these two parameters [83]. Owing to the transformative impact of metamaterials on next-generation information technologies, energy technologies, and microfabrication, *Science* listed metamaterials among the "Top 10 Scientific Breakthroughs of 2003" and as one of the 10 most important scientific advances of the first decade of this century.

However, three-dimensional metamaterial architectures typically suffer from complex fabrication processes, low integration compatibility, and significant Ohmic losses in metals, which hinder their practical deployment. Consequently, researchers shifted their attention to the 2D counterparts of metamaterials—metasurfaces [84,85]. The concept of metasurfaces was first proposed in 2001 by the group of Prof. Federico Capasso at Harvard University [86], where phase modulation for reflection and refraction was demonstrated. In general, metasurfaces consist of subwavelength antenna arrays made of metallic or dielectric building blocks arranged periodically, quasi-periodically, or randomly. By deliberately engineering the geometry and periodicity of these micro-/nano-structures on thin films, metasurfaces enable versatile manipulation of multiple optical degrees of freedom, including amplitude, phase, and polarization. Their ultrathin profiles, negligible electromagnetic loss, small pixel sizes, and relatively low fabrication complexity effectively overcome the shortcomings of conventional materials and three-dimensional metamaterials. As a result, metasurfaces have shown tremendous potential in metalenses [87–90], polarization detection [91–93], holographic imaging [94–96], vortex beam generation [97–100], nonlinear optics [101–103], sensing [104,105], and other fields.

Metasurfaces can be broadly categorized into three main types based on the primary degree of freedom they manipulate: amplitude-modulation metasurfaces, phase-modulation metasurfaces, and polarization-modulation metasurfaces. Amplitude-modulation metasurfaces manipulate the line shape of optical spectra within specific wavelength ranges, including transmission, reflection, absorption, and emission spectra. Transmission and reflection modulation is widely applied in filtering, sensing, structural coloration, and slow-light systems [106–109]. Absorption- and radiation-control metasurfaces often correspond to various types of perfect absorbers, with major applications in electromagnetic stealth, thermophotovoltaics, sensing, infrared camouflage, radiative cooling, and related fields [110–113].

Meanwhile, according to the material composition, metasurfaces can be divided into two major types: plasmonic (metallic) metasurfaces and dielectric metasurfaces [114] as illustrated in Fig. 2.1.

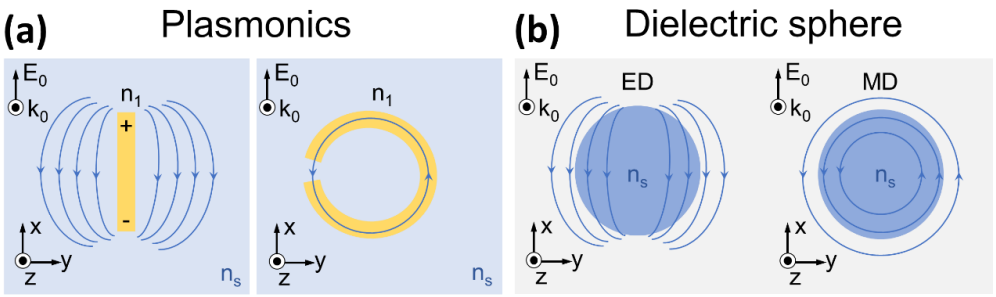

Figure 2.1 (a) Plasmonic resonators of metasurfaces and (b) dielectric resonators of metasurfaces.

Metallic metasurfaces support collective electron oscillations at metal–dielectric interfaces, i.e., surface plasmons. When the incident light frequency matches the oscillation frequency, plasmonic resonance is excited, producing strong local field enhancement [114–116]. Despite advantages such as high integration density, strong light confinement, and efficient hot-electron generation, plasmonic metasurfaces suffer from considerable optical loss originating from electron–electron and electron–phonon scattering in metals, which severely limits the performance of optical devices like lenses, holograms, and waveplates. In contrast, dielectric metasurfaces consist of periodically arranged high-index nanoparticles whose sizes are comparable to the operating wavelength, supporting Mie resonances instead of plasmonic ones. Owing to the large bandgaps of dielectric materials, optical loss is significantly reduced because sub-bandgap excitation does not generate free carriers, resulting in displacement currents rather than conduction currents. This enables strong electric-field localization while maintaining negligible absorption. With their low optical loss, dielectric metasurfaces offer markedly higher

quality factors, improved efficiency, and superior stability compared with plasmonic metasurfaces. Additionally, their fabrication is compatible with standard Complementary Metal–Oxide–Semiconductor (CMOS) processes, reducing fabrication difficulty and cost, thus facilitating real-world applications. Benefiting from these outstanding optical properties, all-dielectric metasurfaces have experienced rapid development across numerous research areas [117–121].

2.2 Mie scattering

Mie scattering describes the interaction between electromagnetic waves and particles whose characteristic size is comparable to the wavelength of the incident light. The rigorous analytical solution of this problem was first derived by Gustav Mie in 1908 for the case of a homogeneous spherical particle illuminated by a plane wave [122]. This theory provides an exact solution of Maxwell's equations and forms the theoretical foundation for understanding optical resonances in high-refractive-index dielectric nanoparticles and metasurfaces.

We consider a homogeneous spherical particle of radius R and relative permittivity ε_p, embedded in a homogeneous background medium with permittivity ε_b. A monochromatic plane wave with angular frequency ω is incident along the z-direction. The scattering geometry and coordinate system are illustrated in Fig. 2.2.

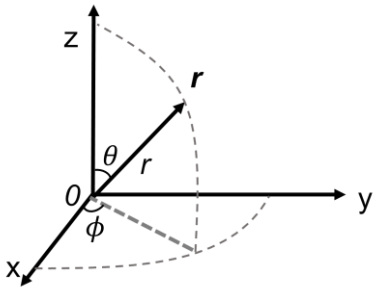

Figure 2.2 Schematic of the Mie scattering geometry in spherical coordinates. A dielectric sphere of radius r. The incident plane wave propagates along the +z direction. Here r is the radial distance, θ is the polar angle measured from the z-axis, and ϕ is the azimuthal angle in the x–y plane.

The time-harmonic Maxwell equations are [123]

$$\nabla \cdot \boldsymbol{E} = 0 \tag{2.1}$$

$$\nabla \cdot \boldsymbol{H} = 0 \tag{2.2}$$

$$\nabla \times \boldsymbol{E} = i\omega\mu\boldsymbol{H} \tag{2.3}$$

$$\nabla \times \boldsymbol{H} = -i\omega\varepsilon\boldsymbol{E} \tag{2.4}$$

Here $\boldsymbol{E}$ and $\boldsymbol{H}$ denote the complex electric and magnetic field phasors, ω is the angular frequency of the incident wave, i is the imaginary unit. ε and μ are the permittivity and permeability of the medium. The incident, scattered, and internal electric fields are denoted as $\boldsymbol{E_0}$, $\boldsymbol{E_s}$, and $\boldsymbol{E_p}$, respectively. Outside the particle, the total field is

$$\boldsymbol{E} = \boldsymbol{E_0} + \boldsymbol{E_s} \tag{2.5}$$

while inside the particle $\boldsymbol{E} = \boldsymbol{E_p}$. At the particle boundary $r = R$, the tangential components of the electric and magnetic fields satisfy the standard electromagnetic boundary conditions.

The incident, scattered, and internal fields are expanded using vector spherical wave functions. The scattered field can be written as [124,125]

$$\boldsymbol{E_s} = \sum_{n=1}^{\infty}\sum_{m=-n}^{n} E_0\left[a_n \boldsymbol{N}_{nm}^{(3)}(k_b r) + b_n \boldsymbol{M}_{nm}^{(3)}(k_b r)\right] \tag{2.6}$$

and the internal field as

$$\boldsymbol{E_P} = \sum_{n=1}^{\infty}\sum_{m=-n}^{n} E_0\left[c_n \boldsymbol{N}_{nm}^{(1)}(k_p r) + d_n \boldsymbol{M}_{nm}^{(1)}(k_p r)\right] \tag{2.7}$$

where $k_b = \sqrt{\varepsilon_b}k_0$, $k_p = \sqrt{\varepsilon_p}k_0$ and $k_0 = \omega/c$ is the free-space wave number.

$\boldsymbol{M}_{nm}$ and $\boldsymbol{N}_{nm}$ are the magnetic- and electric-type vector spherical harmonics, respectively.

Applying the boundary conditions at $r = R$, the scattering coefficients a_n and b_n are obtained as

$$a_n = \frac{m\psi_n(mx)\psi_n'(x) - \psi_n(x)\psi_n'(mx)}{m\psi_n(mx)\xi_n'(x) - \xi_n(x)\psi_n'(mx)} \tag{2.8}$$

$$b_n = \frac{\psi_n(mx)\psi_n'(x) - m\psi_n(x)\psi_n'(mx)}{\psi_n(mx)\xi_n'(x) - m\xi_n(x)\psi_n'(mx)} \tag{2.9}$$

where

$$x = k_b R \tag{2.10}$$

$$m = \sqrt{\frac{\varepsilon_p}{\varepsilon_b}} \tag{2.11}$$

$$\psi_n(z) = zj_n(z) \tag{2.12}$$

$$\xi_n(z) = zh_n^{(1)}(z) \tag{2.13}$$

with $j_n(z)$ and $h_n^{(1)}(z)$ being the spherical Bessel and Hankel functions, respectively. The scattering, extinction, and absorption cross sections of the particle are given by [126]

$$C_{sca} = \frac{2\pi}{k_b^2}\sum_{n=1}^{\infty}(2n+1)(|a_n|^2 + |b_n|^2) \tag{2.14}$$

$$C_{ext} = \frac{2\pi}{k_b^2}\sum_{n=1}^{\infty}(2n+1)Re(a_n + b_n) \tag{2.15}$$

$$C_{abs} = C_{ext} - C_{sca} \tag{2.16}$$

Correspondingly, the dimensionless efficiencies are defined as

$$Q_{sca} = \frac{C_{sca}}{\pi R^2}, \qquad Q_{ext} = \frac{C_{ext}}{\pi R^2}, \qquad Q_{abs} = \frac{C_{abs}}{\pi R^2} \tag{2.17}$$

These quantities fully characterize the optical scattering response of a dielectric nanoparticle. The lowest-order terms $n = 1$ in the Mie coefficients correspond to the electric and magnetic dipole modes: a_1 corresponding to electric dipole (ED) resonance, b_1 corresponding to magnetic dipole (MD) resonance. The electric dipole moment $\boldsymbol{p}$ and magnetic dipole moment $\boldsymbol{m}$ are given by

$$\boldsymbol{p} = \frac{6\pi i\varepsilon_b}{k_b^3} a_1 \boldsymbol{E_0} \tag{2.18}$$

$$\boldsymbol{m} = \frac{6\pi i}{k_b^3} b_1 \boldsymbol{H_0} \tag{2.19}$$

For the ED mode, charge displacement is induced along the direction of the incident electric field, generating a circulating magnetic field inside the particle. In contrast, the magnetic dipole (MD) mode originates from the circulating displacement currents inside the dielectric, which generate a MD aligned with the incident magnetic field as shown in 2.1(b).

As the particle size increases, higher-order multipoles $(n \geq 2)$, such as electric and magnetic quadrupoles, also become significant and contribute to the total scattering spectrum [124].

In high-refractive-index dielectric nanoparticles, such as Si, TiO_2, and GaP [127,128], both ED and MD resonances can be efficiently excited in the visible and near-infrared spectral ranges. Compared with plasmonic resonances in metals, Mie resonances exhibit significantly reduced ohmic loss and higher quality factors [26,27].

When individual dielectric resonators are periodically arranged to form a metasurface, their collective response can be described as the coupling of ED and MD modes. Furthermore, the interference between ED and MD modes can satisfy the Kerker conditions [129], leading to suppressed backward scattering or enhanced forward scattering, which is crucial for wavefront shaping, perfect transmission, and Huygens-type metasurfaces [117,118].

Therefore, Mie scattering and the associated multipolar resonances constitute the fundamental physical mechanism underlying dielectric metasurfaces and their applications in flat optics, nonlinear optics, nanolasers, and exciton–photon strong coupling systems.

2.3 Optical cavity of Mie resonators and Purcell effect

Although Mie scattering theory provides a rigorous classical solution to Maxwell's equations for dielectric particles, high-index Mie resonators can also be interpreted as optical cavities supporting discrete electromagnetic eigenmodes. In the cavity, the resonant modes of a dielectric nanoparticle or metasurface meta-atom act as confined photonic states with enhanced electromagnetic energy density in a subwavelength volume. Such a resonant system can strongly modify light–matter interaction by engineering the local density of optical states (LDOS), which is the key concept in cavity quantum electrodynamics (cavity-QED).

In cavity-QED, the spontaneous emission rate of a quantum emitter is not an intrinsic constant but depends on its photonic environment. When an emitter such as an exciton is placed inside or near an optical cavity, the available electromagnetic modes for radiation are altered, which can lead to either enhancement or suppression of spontaneous emission. This phenomenon is described by the Purcell effect.

For a dipole emitter coupled to a single cavity mode, the Purcell factor F_p, defined as the ratio between the spontaneous emission rate in the cavity and that in free space, can be expressed as

$$F_p = \frac{\Gamma}{\Gamma_0} = \frac{3}{4\pi^2} \left(\frac{\lambda}{n}\right)^3 \frac{Q}{V_m} \tag{2.20}$$

where Γ and Γ_0 are the radiative decay rates with and without the cavity, respectively, λ is the free-space wavelength, n is the refractive index of the surrounding medium, Q is the quality factor of the cavity resonance, and V_m is the effective mode volume of the cavity mode. This equation indicates that a large Purcell enhancement can be achieved by simultaneously maximizing the quality factor and minimizing the mode volume.

Mie resonators are particularly attractive in this context because they naturally provide strong field confinement and can support high-Q resonances, including ED, MD, and higher-order multipolar modes. Compared to plasmonic resonators, dielectric Mie resonators exhibit significantly reduced ohmic loss, enabling higher Q factors and thus potentially stronger Purcell enhancement. In metasurfaces composed of periodically arranged Mie resonators, the coupling between neighboring resonators can further modify the radiative leakage rate, giving rise to collective resonances and quasi-bound states in the continuum (quasi-BIC), which can achieve extremely high Q values. Mie resonators and metasurfaces can be regarded as a promising cavity-QED platform, where the radiative properties of excitons can be efficiently manipulated through engineered resonant modes. This cavity interpretation provides an essential foundation for understanding coupling in WS_2–metasurface systems discussed later.

2.4 Degenerate critical coupling (DCC)

In 2017, all-dielectric perfect absorbers based on degenerate critical coupling (DCC) were first proposed, enabling perfect absorption in monolayer nanostructures [130]. Following this pioneering work, a series of DCC-based perfect absorbers were rapidly demonstrated across a broad spectral range, including the visible region [131,132], the near-infrared region [133,134], and the terahertz regime [130,135], highlighting the wide applicability of the DCC mechanism for broadband photonic absorption control.

The incident beam can be decomposed into two sets of counter-propagating coherent beams, each with half the electric field amplitude. Among them, one of the coherent beams with no phase difference is regarded as even eigenexcitation coupled only to an even mode (e.g., ED mode) due to the same symmetry, while the second one with phase difference is considered as odd eigenexcitation coupled only to an odd mode (e.g., MD mode) as ahown in Fig 2.3.

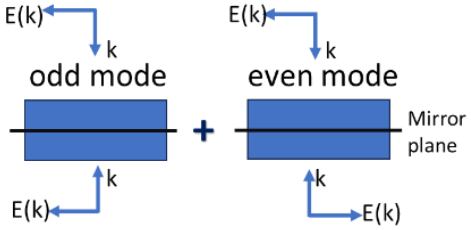

Figure 2.3 Schematic of two sets of counter-propagating coherent beams.

Consequently, Mie resonators are capable of simultaneously supporting ED and MD modes, which exhibit opposite symmetry [136,137]. More significantly, when orthogonal ED and MD resonances are simultaneously supported on a Si metasurface, the DCC of two modes is achieved at the same wavelength (namely, the so-called Huygens Si metasurface [136,138]). Based on coupled-mode theory, the total absorption of Mie resonance modes was derived from the independent contributions of the even and odd modes, which can be described as the sum of the absorption of ED and MD modes as follows [139]:

$$A = \frac{2\gamma_1\delta_1}{(\omega-\omega_1)^2+(\gamma_1+\delta_1)^2} + \frac{2\gamma_2\delta_2}{(\omega-\omega_2)^2+(\gamma_2+\delta_2)^2} \tag{2.21}$$

where ω, ω_1, and ω_2 represent the angular frequency of the incoming light, the even and odd modes; and γ_1, γ_2, δ_1, and δ_2 denote the radiative and intrinsic losses of the even and odd modes, respectively. The absorption of the even eigenexcitation reaches its maximum at resonance when the radiative loss of the ED mode matches its intrinsic loss ($\gamma_1 = \delta_1$). The absorption process for the MD mode follows the same process. In this context, the electric field distributions corresponding to different modes can also reach their maxima, thereby achieving the maximum enhancement effect for WS_2.

2.5 DCC in the violet light range

Numerical simulations of the rotated Mie resonators were performed using a commercial three-dimensional electromagnetic solver (Ansys Lumerical FDTD), which is based on the finite-difference time-domain (FDTD) method. A normally incident plane wave was used as the excitation source, with the incident electric field polarized along the *y*-direction. The reflection spectrum was collected by a monitor placed above the source, while the transmission spectrum was recorded by another monitor positioned below the entire structure consisting of the 2D material and the Mie resonator. The absorptivity was calculated as A = 1−R−T.

To ensure high numerical accuracy, a uniform mesh size of 1.6 nm was employed in the simulation region. Perfectly matched layers (PMLs) were applied along the *z*-direction to eliminate spurious reflections from the simulation boundaries. Since the incident field is polarized along the *y*-axis, anti-symmetric boundary conditions were imposed along the *y*-direction, while symmetric boundary conditions were applied along the *x*-direction. This symmetry configuration reduces the computational cost by at least a factor of four compared with simulations using full periodic boundary conditions.

Figure 2.4 illustrates the schematic of the unit cell of the proposed Mie resonator array. The Si resonators, with lateral dimensions w_x and w_y and height h, are periodically arranged on a quartz substrate with lattice constants p_x and p_y. The surrounding medium is air, and the electric field of the incident plane wave is polarized along the *x*-direction.

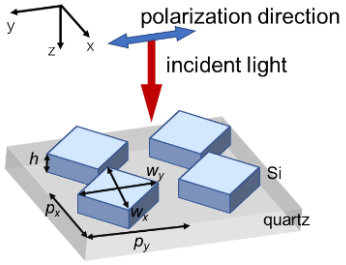

Figure 2.4 Schematic Si metasurface composed of Mie resonator arrays.

Figure 2.5 presents the simulated absorption spectral map of the Mie resonator array as the resonator height h varies from 40 to 90 nm. For the structure with h = 90 nm, two distinct resonance peaks appear at 449 nm and 488 nm.

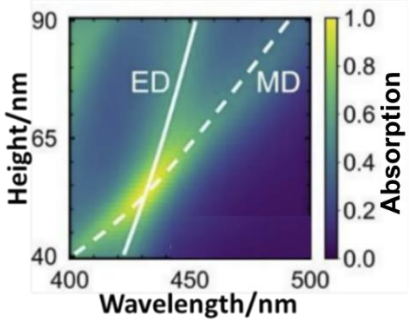

Figure 2.5 Absorption spectral map of the Metasurface.

The electric-field distribution at 449 nm, shown in Fig. 2.6(a), corresponds to the ED resonance, which originates from the collective polarization response of the Si resonator to the incident electromagnetic field. In contrast, the field profile at 488 nm in Fig. 2.6(b) reveals a MD resonance formed by a closed loop of displacement current inside the resonator.

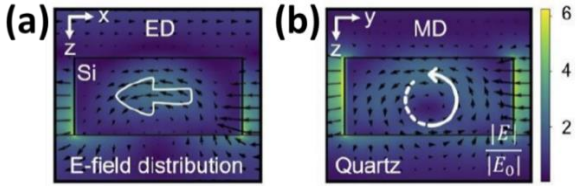

Figure 2.6 Electric field distributions in (a) the ED mode at 449 nm and in (b) the MD mode at 488 nm.

As the height *h* decreases, the MD resonance exhibits a more pronounced blue shift than the ED resonance. This behavior arises because the establishment of the displacement-current loop responsible for the MD mode requires sufficient phase retardation along the vertical direction, making the MD resonance highly sensitive to variations in *h*. Consequently, with decreasing *h*, the MD resonance progressively approaches the ED resonance in wavelength, and the two modes spectrally coincide at $h = 53$ nm. Notably, as the two resonances converge, the absorption of the Mie resonator array is significantly enhanced and reaches unity at the degeneracy condition. With further reduction of *h*, the MD resonance shifts to shorter wavelengths than the ED resonance, and the two modes become spectrally separated again.

To examine the influence of geometrical rotation on the damping rate γ of the ED resonance, the reflection spectra of identical Mie resonators with and without in-plane rotation are compared in Fig. 2.7. For clarity, the resonator material is assumed to be lossless in the simulations. As shown in Fig. 2.7(a), the reflection peak of the non-rotated resonators is considerably sharper than that of the rotated configuration displayed in Fig. 2.7(b), indicating a smaller radiative damping rate for the ED mode in the unrotated structure. In this work, the resonators are rotated by 45° to intentionally broaden the full width at half maximum (FWHM) of the resonance peak, corresponding to an increased γ.

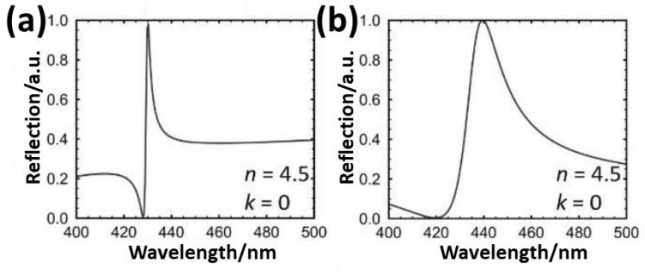

Figure 2.7 Reflection spectra of Mie resonators with a width of 140 nm, (a) unrotated and (b) rotated by 45°.

By continuously varying the rotation angle from 0° to 45° for resonators with $p_x = p_y = 220$ nm, the FWHM of the reflection peak is found to increase monotonically from 17.7 nm to 27.3

nm. This trend demonstrates that the damping rate of the ED mode can be continuously tuned through geometric rotation. It should be emphasized that this rotational modulation is fundamentally different from changing the polarization of normally incident illumination.

The reduced γ observed in the non-rotated structure arises from strong near-field coupling between adjacent resonators along the direction perpendicular to the incident electric-field polarization (y-direction), as illustrated in Fig. 2.8. Under this condition, a low-loss transverse electric dipole (TED) mode is excited, which radiates with a scattering profile analogous to that of the ED mode. The radiative linewidth of the ED resonance is thus suppressed as a result of destructive interference between the ED and TED modes. In contrast, once the resonators are rotated, the electromagnetic interaction between neighboring units along the y-direction is weakened due to the redistribution of the local field at the resonator corners (highlighted by the white dashed box). Moreover, rotation effectively disturbs the compact spatial arrangement, further diminishing inter-resonator coupling. As a consequence, the suppression effect induced by the TED mode is reduced, leading to a pronounced increase in the damping rate γ of the ED resonance for the rotated resonators.

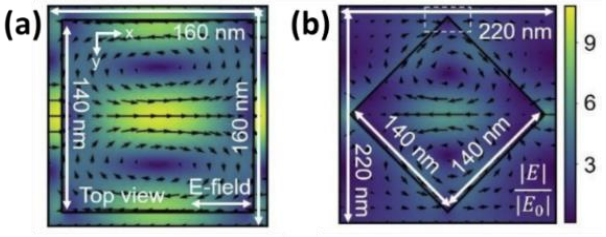

Figure 2.8 Top view of electric field distributions of (c) unrotated Mie resonators at 430 nm and (d) rotated Mie resonators at 439 nm.

Figure 2.9 presents the calculated absorption, transmission, and reflection spectra of the Si perfect absorber with a resonator height of h = 53 nm. Under this geometrical condition, DCC is realized, leading to near-unity absorption at a wavelength of 430 nm.

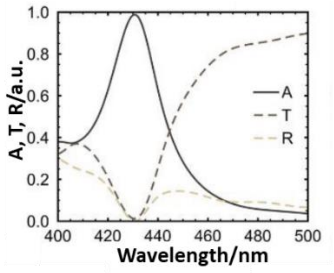

Figure 2.9 Absorption, transmission, and reflection spectra of rotated Si Mie resonators.

To experimentally validate the proposed perfect absorber, a corresponding sample was fabricated. The designed Si metasurface was fabricated on a silicon-on-quartz (SOQ) substrate

using a lift-off process. The fabrication procedure is schematically illustrated in Fig. 2.10. To precisely control the target thickness of the Si layer, the initial 150 nm-thick Si film was first thinned using a reactive ion etching (RIE) system (EIS-700, ELIONIX Inc.). A ZEP-520A electron-beam resist layer with a thickness of approximately 120 nm was then spin-coated onto the substrate, followed by soft baking on a hot plate at 180 °C for 2 minutes. Elliptical nanopatterns were subsequently defined by electron-beam lithography (ELS-100T, ELIONIX Inc.). The exposed resist was developed in ZEP-N50 developer (Zeon Corp.) for 30 s.

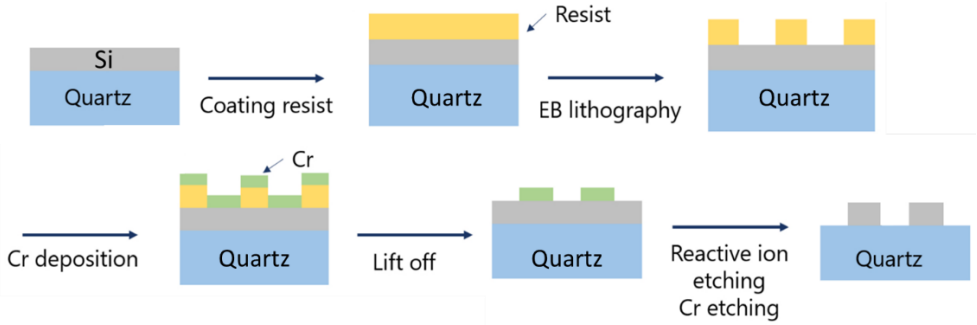

Figure 2.10 Flow diagram of fabrication process of Si metasurface.

After pattern development, a 20 nm-thick chromium film was deposited by electron-beam evaporation (UEP-2000 OT-H/C, ULVAC Inc.) to serve as a hard mask. The remaining resist was removed by immersing the sample in N-methyl-2-pyrrolidone (NMP). The patterned Si layer was then etched again using the RIE system to transfer the mask pattern into the Si. Finally, the Cr hard mask was removed with a commercial wet etchant (S-CLEAN S-24, SASAKI CHEMICAL CO., LTD.), completing the fabrication of the Si metasurface.

Figure 2.11(a) presents the measured absorption, transmission, and reflection spectra of the fabricated sample. The experimental results show that the absorption exceeds 70% at 430 nm. To clarify the origin of the reduced absorption compared with the ideal case, additional simulations were carried out. As shown in Fig. 2.11(b), the simulated spectra based on the experimentally realistic structure agree well with the measured results.

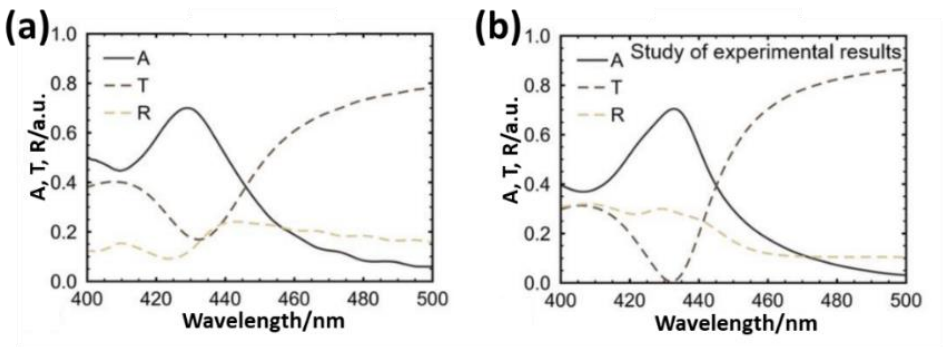

Figure 2.11 (a) Measured and (b) simulated transmission and reflection spectra of the sample.

According to the revised simulation model of the rotated Mie resonators, the primary reason for the reduced absorption is the smaller period in the fabricated sample relative to the ideal design. Specifically, p_y decreases from 260 nm in the ideal structure to 220 nm in the fabricated one, as adopted in the simulation of Fig. 2.10(b). A reduced period leads to a smaller radiative loss rate γ, which no longer perfectly matches the intrinsic loss δ at 430 nm. Consequently, the critical coupling condition between the ED and MD modes is not fully satisfied, resulting in a decrease in absorption.

A secondary contribution to the reduced absorption arises from slight geometric deviations of individual Mie resonators from the ideal design. The fabricated resonators exhibit a height of approximately 55 nm, which is about 2 nm larger than the designed value of 53 nm, giving rise to a small redshift of the MD resonance. In addition, the partial removal of the four edges of the resonators to a depth of roughly 10 nm induces a slight blueshift of the ED resonance. These structural imperfections prevent the ED and MD modes from being perfectly spectrally overlapped, leading to a modest broadening of the absorption peak and a further reduction in peak absorptance.

Because the characteristic dimensions of the proposed Mie resonators are on the order of 100 nm, the final fabrication quality is strongly dependent on the performance of the electron-beam lithography system. Nevertheless, further optimization remains feasible without changing the fabrication equipment. In the present study, the deviation in the array period is identified as the dominant factor affecting the optical response and should therefore be compensated at the layout design stage by anticipating proximity effects. The use of multilayer resist systems can effectively suppress electron backscattering, whereas proximity effect correction software enables spatial modulation of the exposure dose. In our fabrication, only a single-layer resist and uniform exposure dose were employed. With these improvements implemented, the absorption of the fabricated structure is expected to exceed 90%.

2.6 DCC in the visible light range

Figure 2.12 shows the structure of the cylindrical all-dielectric Si Mie resonator array used in the simulation of our study, with radius r, height h, and period p. Among them, $p = 2r + 110$ nm. The ED resonance is primarily governed by the radius r of the resonator and shows only weak dependence on its height h. In contrast, the MD mode arises from a circulating displacement current, and its formation is strongly determined by the resonator height. When the structure is too shallow, the phase retardation is insufficient to establish a closed displacement current loop,

thereby suppressing the MD resonance. These characteristics indicate that the spectral superposition of the ED and MD modes, namely the DCC condition, can be realized through coordinated tuning of *r* and *h* of the Si cylindrical Mie resonators [139,140].

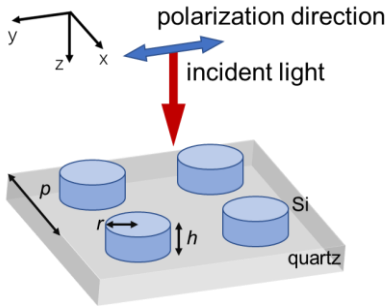

Figure 2.12 Schematic Si metasurface composed of Mie resonator arrays.

To clarify the evolution of the ED and MD modes, we performed systematic numerical simulations by varying *r* and *h*. Figure 2.13 shows the calculated absorption spectral map as a function of *h* and *r* from 55 to 115 nm, where the absorption is defined as $A = 1-T-R$. With increasing *h*, the MD mode exhibits a more pronounced red shift than the ED mode, indicating that their relative spectral positions can be continuously tuned via the resonator height. By properly selecting *h* and further fine-tuning *r*, the ED and MD resonances can be brought into spectral coincidence. For a period $p = 334$ nm, radius $r = 112$ nm, and height $h = 92$ nm, complete spectral overlap of the ED and MD modes is achieved, corresponding to the formation of a Si Huygens metasurface.

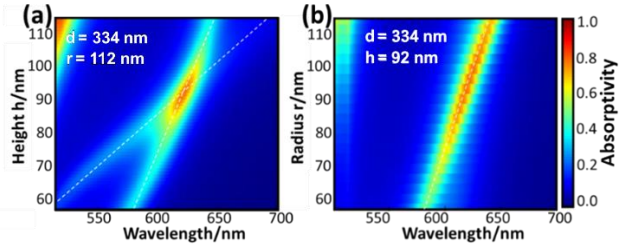

Figure 2.13 Absorption spectral mapping of the Si metasurface with variations in (a) *h* and (b) *r*.

To unambiguously identify the physical origin of the resonance appearing near 615 nm, a three-dimensional periodic model was established using the COMSOL Multiphysics electromagnetic solver to perform a multipole decomposition analysis [141]. The geometric configuration, material parameters, and electromagnetic boundary conditions were set identical to those adopted in the FDTD simulations to ensure strict consistency between the two numerical approaches. Based on the calculated near-field distributions, the Cartesian multipole moments were extracted, including the ED, MD, electric quadrupole (EQ), and magnetic quadrupole (MQ) contributions, as summarized in Fig. 2.14(a). The results demonstrate that, in the vicinity of 615

nm, the optical response is overwhelmingly governed by the ED and MD components, whereas higher-order multipoles contribute only weakly.

To further validate the multipole analysis, the far-field reflection spectrum was reconstructed from the extracted multipole moments and compared with the reflection spectrum obtained directly from full-wave FDTD simulations, as shown in Fig. 2.14(b). Excellent agreement is observed between the two spectra, with nearly identical resonance positions and overall spectral trends, despite minor discrepancies in the detailed line shapes. This strong consistency confirms the robustness and reliability of the multipole inversion procedure. More importantly, it provides clear evidence that the resonance near 615 nm predominantly originates from the coherent coupling and spectral superposition of the ED and MD modes, rather than from higher-order multipolar contributions.

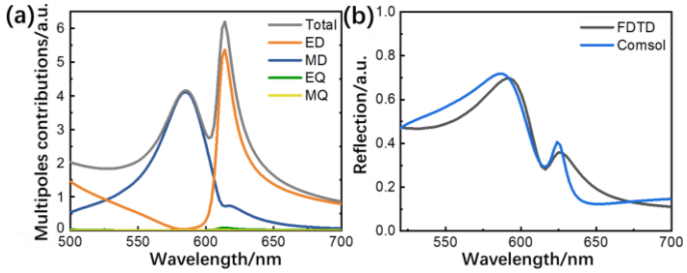

Figure 2.14 (a) Absolute magnitudes of the individual multipolar contributions to the scattered electric-field amplitude. (b) Comparison of the reflection spectra reconstructed by COMSOL-based multipole decomposition and those calculated directly using FDTD simulations.

We numerically calculated the absorption spectra of the Si Huygens metasurface, as shown in Fig. 2.15. The spectral crossing of the MD and ED modes is tuned to 607 nm, yielding a maximum absorptivity of 0.72. The Mie resonance wavelength was optimized to match the absorption peak of the WS_2 monolayer in order to maximize the light–matter interaction. In principle, metasurface absorbers with spectrally degenerate ED and MD modes can reach perfect absorption when the resonance condition $\omega_1 = \omega_2$ is satisfied under DCC [142–146].

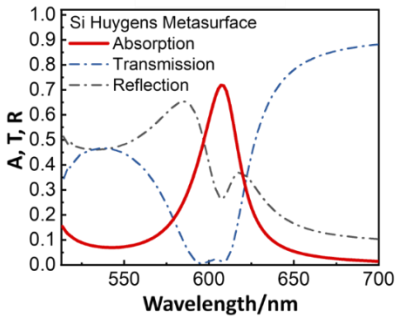

Figure 2.15 Absorption, transmission, and reflection spectra of Si Mie resonators.

However, in the visible region, achieving unity absorption with c-Si is difficult due to its limited intrinsic loss. Introducing materials with moderate refractive indices and higher absorption, such as amorphous silicon (a-Si), can relax this constraint and enable perfect absorption under DCC conditions [147]. Considering fabrication complexity, a-Si was not incorporated in the present simulations.

Chapter 3 Intermediate coupling in Miexcitons

Excitons in 2D transition metal dichalcogenides play a central role in light–matter interactions, yet their optical absorption remains weak at room temperature. This chapter investigates the optical response of a WS_2 monolayer integrated with Si Mie resonators, with a particular focus on the intermediate coupling regime that emerges between the excitonic transitions and the ED mode supported by the metasurface. We examine the separate contributions of the ED mode and the MD mode, followed by a detailed analysis of the combined ED–MD response.

In the case of ED mode, the system exhibits a clear anticrossing behaviour that originates from the coherent coupling between the exciton and the ED resonance. The coupling strength is further amplified by DCC, which enables efficient energy transfer into the excitonic channel and increases the WS_2 absorption. These results demonstrate the emergence of Miexciton and establish a versatile platform for controlling exciton–photon interactions in 2D semiconductors.

3.1 Different effects of Mie modes on 2D WS_2

To strengthen the light–matter interaction in monolayer WS_2, we place the 2D material on the dielectric metasurface as illustrated in Fig. 3.1 so that the excitonic response can be reinforced through superimposed–mode enhancement mechanisms. In this configuration, the resonant modes sustained by the metasurface, primarily the ED and MD modes, interact with the excitonic transitions of WS_2 and enable strong absorption modulation. As discussed earlier, the resonance wavelength of the Mie modes can be tuned by adjusting the height and radius of the Si cylinder, allowing us to align the Mie resonance with the excitonic transition of WS_2.

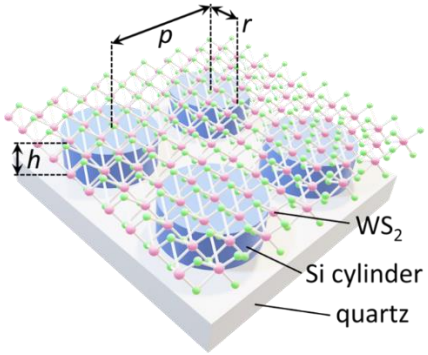

Figure 3.1 Schematic view of 2D WS_2 on Si metasurface comprising Si cylindrical Mie resonators.

To identify the optimal structural parameters for resonance–exciton coupling, we systematically varied the radius *r* of the Si cylindrical resonators and computed the corresponding absorption spectral maps, as shown in Fig. 3.2. By scanning *r*, we tracked the evolution of the resonance wavelengths associated with the MD and ED modes. Both resonances exhibit pronounced shifts with increasing radius, due to the sensitivity of the modal dispersion to the geometric dimensions. Both MD and ED modes could approach the WS_2 A-exciton wavelength, indicating a potential spectral overlap suitable for coupling.

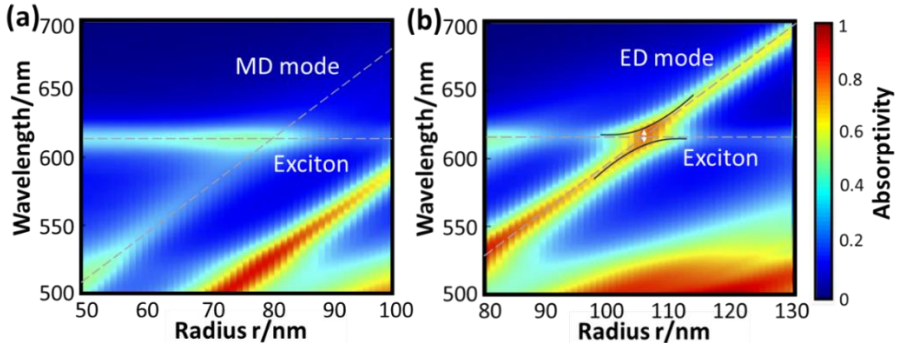

Figure 3.2 Absorption spectral map of metasurface and WS_2 placed on the it for (a) MD, (b) ED modes as a function of *r*.

Under the MD condition, as the wavelength is tuned toward the longer-wavelength region, the resonance peak intensity decreases because the material loss of Si and the structural loss become mismatched. At the same time, the absorption associated with the WS_2 exciton and the MD photonic resonance exhibits a clear spectral crossing: as the MD resonance is tuned across the exciton wavelength, the two features intersect in the dispersion map.

By contrast, the ED mode exhibits a distinctly different response within the same parameter regime: instead of a simple spectral crossing, a clear anticrossing behavior emerges. The resonant interaction between electronic transitions and confined electromagnetic fields can give rise to a reversible, coherent exchange of energy between light and matter. In this regime, the system no longer supports isolated eigenstates; instead, two energetically separated hybrid modes are formed, a phenomenon known as Rabi splitting.

3.2 Strong coupling in light-matter interaction: Rabi splitting

Depending on the interaction strength, the coupling can be categorized as weak, intermediate, and strong. In the weak-coupling regime, the Purcell effect modifies the radiative transition rate between two electronic levels in an atom or molecule [148]. This behavior can be demonstrated by placing a two-level emitter inside an optical cavity, which alters the LDOS. Because the emitter can radiate only into the cavity field, its emission is enhanced. However, when the interaction becomes sufficiently strong, not only the radiative rate but also the energy levels themselves are modified.

In general, strong coupling is characterized by a reversible coherent energy exchange between light and matter. Sometimes, it also happened in the intermediate coupling regime. The system forms two new hybrid modes with distinct energies, rather than maintaining its original pair of degenerate bare states as illustrated in Fig. 3.3. This Rabi splitting manifests experimentally as a characteristic double-peaked spectral feature or anticrossing phenomenon.

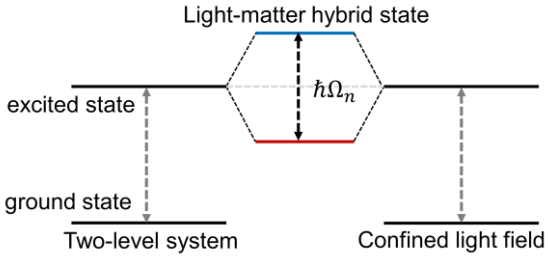

Figure 3.3 Schematic diagram of new hybrid states generated by strong coupling between a two-level system and a confined light field.

In our WS_2-metasurface setup, the ED mode and the excitons in monolayer WS_2 form two hybridized eigenmodes under strong or intermediate coupling, which are commonly denoted as ω_{-n} and ω_{+n} corresponding to the lower and upper polariton branches respectively, as shown in Fig. 3.4. The coupling strength can be quantified from the energy separation between the two polariton branches, expressed as $\Omega_n = \omega_{+n} - \omega_{-n}$, which represents the Rabi splitting. A larger Ω_n indicates stronger hybridization and a higher degree of coherent energy exchange between the excitonic and photonic components.

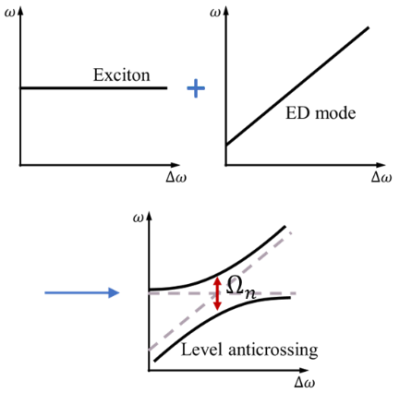

Figure 3.4 Schematic illustration of the coupling between the 2D exciton and the ED mode. The exciton–photon interaction strength is characterized by Rabi splitting Ω_n.

In the simplest conceptual framework, the Jaynes-Cummings model provides a generic description of a two-level emitter interacting with a quantized cavity field [149]. In the context of a 2D semiconductor on a metasurface the roles are replaced by the 2D exciton and a Mie mode supported by the metasurface. For a single two-level excitonic system under the influence of an electromagnetic mode of the metasurface, the Hamiltonian can be generalized as:

$$\hat{H} = \hbar\omega a^{\dagger}a + \frac{1}{2}\hbar\omega_0\sigma_z + \hbar g(a\sigma_+ + +a^{\dagger}\sigma_-) \tag{3.1}$$

where ω denotes the frequency of the metasurface photonic mode and $\omega_0 = (E_e - E_g)/\hbar$ is the exciton transition frequency between the ground state |g⟩ and excited state |e⟩. The operators $a^{\dagger}$ and a denote the creation and annihilation of photons in the resonant mode. Here, g denotes the exciton–photon coupling strength, which quantifies the coherent energy exchange between the exciton and the metasurface mode. The corresponding coupling energy is given by $\hbar g$, and in the lossless resonant case the Rabi splitting is $\Omega_n = 2g$, while σ_+, σ_-, and σ_z are the raising, lowering, and Pauli-Z operators defined as

$$\sigma_+ = \begin{pmatrix} 0 & 1 \\ 0 & 0 \end{pmatrix}, \sigma_- = \begin{pmatrix} 0 & 0 \\ 1 & 0 \end{pmatrix}, \sigma_z = \begin{pmatrix} 1 & 0 \\ 0 & -1 \end{pmatrix} \tag{3.2}$$

Compared to a classic micro-cavity, here the "cavity field" originates from the near-field confinement and resonant mode of the metasurface rather than a closed Fabry–Pérot resonator. This description remains broadly applicable because the essential physics (coherent exchange of energy between a discrete electronic transition and a confined photonic mode) is preserved. The coherent coupling strength g quantifies the exciton–photon interaction and can be expressed as

$$g = d\sqrt{\frac{\hbar\omega}{2\varepsilon_0 V_m}} \tag{3.3}$$

where d is the transition dipole moment of the exciton, ε_0 is the vacuum permittivity, and V_m is the effective mode volume. A smaller mode volume or a larger dipole moment gives rise to stronger coupling, which is typically achievable in dielectric metasurfaces with highly confined Mie-type modes.

In the ideal lossless limit, the hybrid system forms two new eigenstates. For photon number n_{ph}, the eigenstates are

$$|\pm\rangle_n = \frac{1}{\sqrt{2}}(\pm|e, n_{ph}\rangle + |g, n_{ph}+1\rangle) \tag{3.4}$$

with energies

$$E_{\pm,n} = \hbar\omega(n+\frac{1}{2}) \pm \hbar g\sqrt{n_{ph}+1} \tag{3.5}$$

The splitting between these two states constitutes the ideal Rabi splitting.

Real metasurfaces are open, radiative systems with intrinsic optical loss governed by the linewidth κ of the photonic resonance. Similarly, excitons in 2D semiconductors exhibit nonradiative and homogeneous broadening characterized by the linewidth γ. When these dissipative processes are included, the hybrid eigenfrequencies of the system become [150]

$$E_{L,U} = \frac{1}{2}(E_{exc} + E_{Mie} + i(\kappa+\gamma)) \pm \sqrt{g^2 - \frac{(\kappa-\gamma)^2}{4}} \tag{3.6}$$

where E_{exc} is the resonance energy of the bare exciton transition in the 2D semiconductor, and E_{Mie} is the resonance energy of the uncoupled photonic mode supported by the dielectric metasurface. g denotes the exciton–photon coupling strength. $E_{L,U}$ correspond to the complex eigenenergies of the lower and upper polariton branches, respectively. The observable energy separation between the upper and lower branches, that is, the effective Rabi splitting, is therefore

$$\hbar\Omega_n = 2\sqrt{g^2 - \frac{(\kappa - \gamma)^2}{4}} \tag{3.7}$$

3.3 Intermediate coupling

In practice, the coupling between an excitonic transition and an optical resonance is not always located in the ideal strong coupling regime. Depending on the relative magnitude of the coupling strength and the dissipation rates of both subsystems, the interaction can be classified into weak coupling, intermediate coupling, and strong coupling regimes. In the weak coupling regime, the coupling strength is much smaller than the total loss rates, and the system does not form new hybrid eigenstates. Instead, the main effect is an enhancement of the spontaneous emission rate due to the Purcell effect, which originates from the modification of the LDOS by the resonant photonic environment. In this regime, no clear mode splitting or anticrossing behavior is expected in the measured spectra.

When the coupling strength becomes comparable to the dissipation rates, the system can enter the intermediate coupling regime, where mode hybridization begins to emerge. A widely adopted definition of the intermediate coupling regime is given by the condition [4]

$$\frac{\gamma_{Mie} - \gamma_{ex}}{2} < 2g < \frac{\gamma_{Mie} + \gamma_{ex}}{2} \tag{3.8}$$

where γ_{Mie} and γ_{ex} represent the linewidths of the metasurface photonic mode and the exciton resonance, respectively, and g is the coherent coupling strength. Under this condition, the coupling is sufficiently strong to induce a measurable hybridization between the exciton and the photonic resonance, leading to the appearance of anticrossing features in energy–momentum or energy–detuning dispersion diagrams. However, the coupling is still not strong enough to fully overcome the dissipative processes, and the system remains partially dominated by radiative and nonradiative losses.

This intermediate coupling regime is particularly important for practical nanophotonic systems, because real dielectric metasurfaces are open radiative structures and excitons in 2D semiconductors typically exhibit substantial homogeneous and inhomogeneous broadening. Therefore, the coupling dynamics cannot always be described as a fully coherent Rabi oscillation, even though spectral splitting and anticrossing may still be observed. As demonstrated in previous studies on light-emitting plexcitonic systems [4], intermediate coupling can provide an optimal balance between hybridization and radiative outcoupling, enabling efficient PL enhancement while still retaining the characteristic mode repulsion behavior.

In contrast, in the strong coupling regime the coupling strength exceeds the combined damping rates of the exciton and the photonic mode. In this case, the exciton and photon undergo coherent and reversible energy exchange, leading to the formation of two well-separated polariton eigenmodes. Although strong coupling is often associated with pronounced Rabi splitting, it does not necessarily maximize photoluminescence intensity. This is because the formation of polaritonic states redistributes the excitonic oscillator strength into two branches, and part of the excitation energy can be trapped in nonradiative decay channels or dissipated through the lossy photonic resonance before being emitted as photons.

Compared with strong coupling, intermediate coupling is often more favorable for enhancing photoluminescence as shown in Fig.3.5. In this regime, the excitonic transition remains strongly involved in the hybrid state, maintaining a large excitonic fraction and thus preserving efficient optical absorption and exciton generation. Meanwhile, the presence of the resonant photonic mode significantly enhances the radiative decay rate through a Purcell-like mechanism, effectively providing an efficient emission channel for excitons. As a result, excitons can recombine more rapidly and radiate into the far field more efficiently. This explains why intermediate coupling can simultaneously exhibit anticrossing behavior and produce stronger photoluminescence enhancement than the fully developed strong coupling regime.

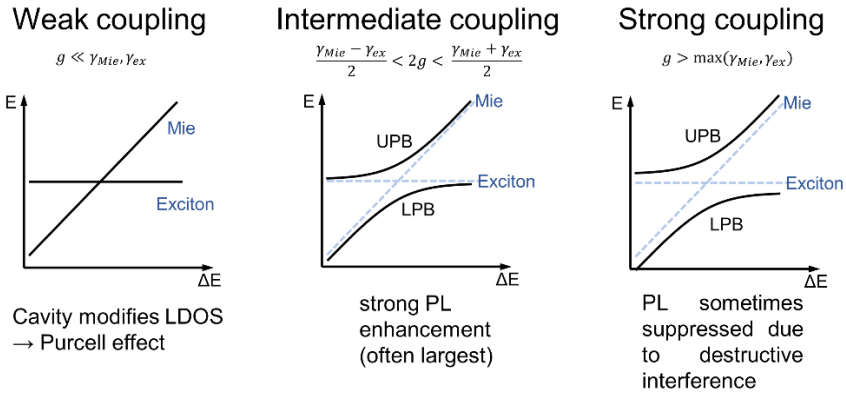

Figure 3.5 Schematic illustration of the different coupling.

Therefore, the observation of anticrossing and the corresponding mode splitting does not necessarily imply that the system is in the ideal strong-coupling regime. Instead, it may indicate intermediate coupling, where the coherent interaction is significant but still comparable to the damping rates. In our system, the experimentally observed anticrossing behavior suggests the formation of hybrid Miexciton states in the intermediate coupling regime. This regime is particularly advantageous for light-emitting applications, as it enables both mode hybridization and strong emission enhancement due to the increased LDOS and accelerated radiative recombination.

3.4 Enhancement effect of MD mode

For the representative geometry of Si cylinder with p = 270 nm, r = 80 nm, and h = 110 nm, the MD resonance becomes nearly aligned with the excitonic transition of monolayer WS_2, as marked in Fig. 3.6. Under this condition, placing WS_2 on the metasurface produces an enhanced and spectrally narrow absorption peak in red line, which differs from the individual spectra of the bare MD resonance in black line or the isolated WS_2 monolayer.

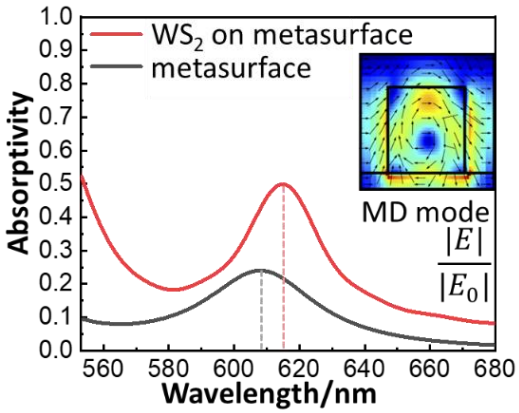

Figure 3.6 Absorption spectra at r = 80 nm of bare metasurface (black) and WS_2 placed on the metasurface (red) for MD modes.

To determine whether the enhanced absorption peak originates predominantly from the MD resonance or from the WS_2 exciton, we performed a systematic simulation in which the thickness of the WS_2 layer was artificially varied while monitoring the corresponding absorption spectra. Although, in practice, modifying the thickness of TMDC materials would also modify their intrinsic optical constants, here we intentionally vary only the geometric thickness while keeping the excitonic parameters unchanged. This allows us to isolate the effect of thickness on the spectral position of the hybrid peak. Figure 3.7 presents the simulated spectra obtained by artificially varying the thickness of the WS_2 and WSe_2 overlayers.

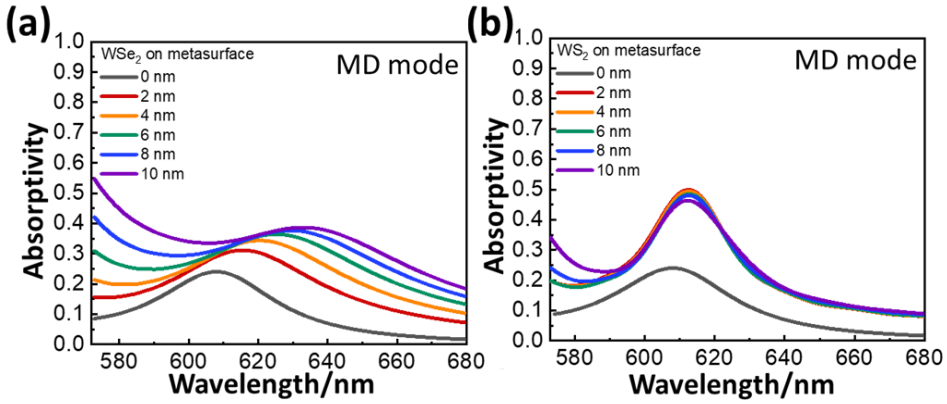

Figure 3.7 Absorption spectra of (a)WS_2, and (b)WSe_2 placed on the metasurface for MD modes with change of WS_2 and WSe_2 thickness.

For the case of WSe_2, which does not support an excitonic transition in this wavelength range, the absorption peak arises solely from the MD mode. As the WSe_2 overlayer becomes thicker, the peak exhibits a noticeable red shift shown in Fig. 3.7(a). This behavior reflects a well-known characteristic of dielectric-loaded Mie resonators: increasing the thickness of the surrounding dielectric modifies the effective refractive index experienced by the confined photonic mode, thereby shifting the resonance wavelength due to altered modal confinement and optical path length.

In contrast, the peak associated with WS_2 remains spectrally constant over the entire thickness range in Fig. 3.7(b). The absence of any observable shift indicates that the feature is anchored to the excitonic transition of WS_2 rather than to the metasurface resonance. Because the exciton energy is unaffected by the thickness variation used in our simulations, the spectral position of the peak remains unchanged, demonstrating that the enhanced absorption originates predominantly from the WS_2 exciton.

Using the PB extraction method, we quantified the contribution of each component to the total absorption shown in Fig. 3.8. The metasurface–WS_2 system exhibits a total absorption of 0.47 at the hybrid resonance. Among this value, approximately 0.27 originates from the WS_2 monolayer, whereas the remaining 0.20 is attributed to the MD mode of the Si resonator. This partitioning clearly indicates that a substantial fraction of the absorbed optical energy is funneled into the excitonic transition.

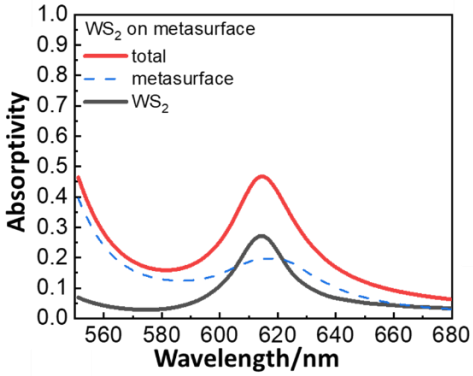

Figure 3.8 Decomposed absorption spectra of WS_2 on metasurface based on MD mode.

The enhancement mechanism is primarily driven by the strong tangential electric field component at the top surface of the resonator, where the WS_2 monolayer is located. Since the exciton population in TMDC monolayers is directly proportional to the local in-plane electric

field intensity [151,152], the MD mode creates a localized electromagnetic environment that significantly amplifies the excitonic absorption.

Despite this synergistic enhancement, the interaction also introduces a competing effect. The presence of WS_2 perturbs the MD resonance, slightly redistributing the electromagnetic field within the Si cylinder. As a result, the intrinsic absorption of the MD mode decreases by approximately 0.04. This reduction reflects the partial energy transfer from the photonic dipole mode into the excitonic channel, a characteristic signature of mode hybridization in dielectric–2D material heterostructures.

3.5 Enhancement effect of ED mode: Miexciton

As shown in Fig. 3.9, when the geometrical parameters of the Si cylinder are set to p = 320 nm, r = 105 nm, and h = 105 nm, the simulated absorption spectrum exhibits a dip characteristic of exciton-induced transparency (EIT). Two distinct absorption maxima, labeled A and B, appear at approximately 610 nm and 623 nm, respectively. These two peaks are clearly separated from both the intrinsic excitonic resonance of monolayer WS_2 and the bare ED photonic mode, demonstrating the formation of new hybrid eigenmodes referred to as Miexcitons. Remarkably, the absorption values of both features exceed 0.70.

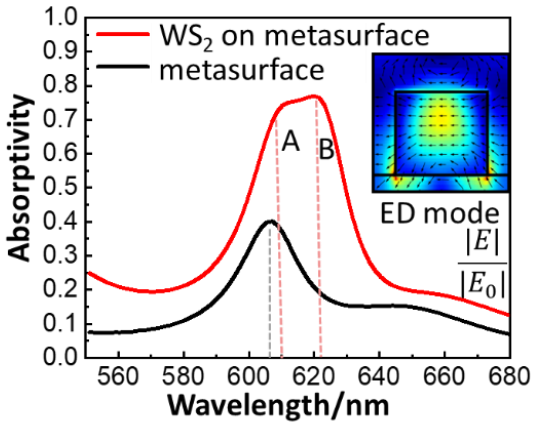

Figure 3.9 Absorption spectra at r = 105 nm of bare metasurface (black) and WS_2 placed on the metasurface (red) for ED modes.

The intrinsic WS_2 contribution, extracted using the PB method shown in Fig. 3.10 reaches as high as 0.55 at resonance, indicating a substantial enhancement of the excitonic absorption. Although the MD mode typically generates a larger tangential electric field at the position of the WS_2 monolayer, which is the conditions that would normally favor stronger interaction, the excitonic peak associated with the ED mode displays a significantly higher absorption.

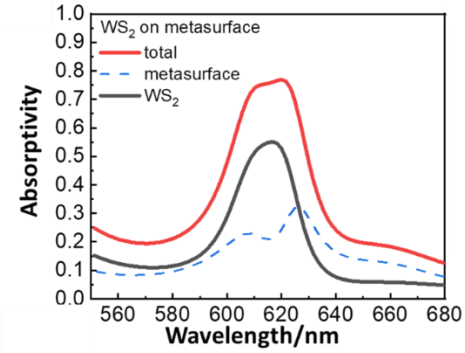

Figure 3.10 Decomposed absorption spectra of WS_2 on metasurface based on ED mode.

Under the present geometry, we therefore attribute the enhanced absorption primarily to the coherent coupling between the ED mode and the excitons. Such coupling enables recurrent energy exchange between photons confined within the resonator and the electronic excitations in WS_2, producing a pair of hybrid states named as Miexciton with redistributed electromagnetic energy density. This redistribution results in a substantial increase in the LDOS near the exciton resonance, which in turn elevates the absorption rate and strengthens the observed excitonic feature [4].

To quantitatively analyze the coupling behavior between the ED photonic mode and the WS_2 exciton, the corresponding resonance features were extracted through Lorentzian fitting, as presented in Fig. 3.11. The fitted absorption spectrum shows two resonance features: the first peak exhibits a linewidth w = 16.5 nm, a peak wavelength of 622.6 nm, and a maximum absorption of 0.41, while the second peak has a linewidth w = 24.4 nm, a peak wavelength of 609.68 nm, and a peak value of 0.53. These parameters provide the basis for determining the spectral separation associated with the hybridized system.

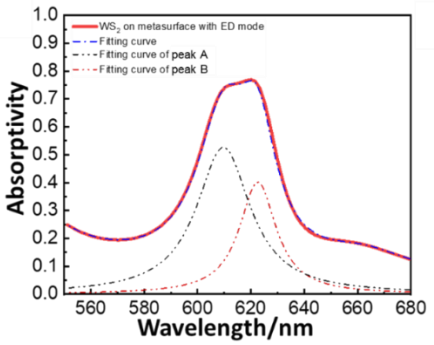

Figure 3.11 Fitting curves to the absorption peaks in Fig. 3.7 for WS_2 on the Si metasurface of ED mode.

From the dispersion analysis shown in Fig. 3.4 combined with peak position extracted from Fig. 3.10, the Rabi splitting energy is estimated to be $\Omega_n \approx 42$ meV. This value is smaller than either the intrinsic excitonic dissipation or the radiative loss of the photonic mode. Under conventional criteria, when the interaction rate is below the combined loss rate, the system does not enter the strong-coupling regime, and clear spectral splitting is typically suppressed [2,153]. However, our structure exhibits a pronounced anticrossing behavior between the ED mode and the exciton. This indicates that the system operates in an intermediate coherence regime, in which energy exchange is not fully reversible but is still sufficiently strong to reshape the optical response and generate hybridized absorption features.

It is worth noting that if the interaction strength were large enough to push the system into the strong-coupling regime, the resulting hybrid branches would shift further away from the original exciton energy. Such a shift would reduce the LDOS at the excitonic wavelength and consequently diminish the relative contribution of WS_2 to the total absorption—a behavior that has been reported in similar exciton–photon hybrid systems [4]. In contrast, the intermediate coupling achieved here retains a near-resonant LDOS enhancement, thereby maximizing the absorption associated with the monolayer WS_2.

3.6 Enhancement effect of MD & ED modes

Both the ED and MD resonances can individually enhance the absorption of monolayer WS_2 when their spectral positions overlap with its excitonic transition. This observation indicates that bringing the two resonances into close spectral proximity, while simultaneously matching them to the WS_2 exciton wavelength, provides an effective strategy for further improving light–matter interaction. Building on the dual-mode DCC concept introduced in Section 2.6, we designed a Si metasurface that enables the ED and MD modes to reinforce at the excitonic absorption wavelength.

By selecting an appropriate cylinder height h and adjusting the radius r with fine resolution, the spectral positions of the ED and MD resonances gradually approach each other. For the optimized geometry with $d = 334$ nm, $r = 112$ nm, and $h = 92$ nm, the two photonic modes of the Si Huygens metasurface become nearly coincident. Their merged resonance wavelength also aligns well with the intrinsic excitonic transition of monolayer WS_2. The corresponding absorption spectra of both the bare metasurface and the WS_2-integrated structure are shown in Fig. 3.12. Under these optimized parameters, the combined Mie resonance produces an intense

absorption peak at approximately 607 nm with a maximum value of 0.72. This resonance serves as the basis for maximizing the absorption of the WS_2 monolayer.

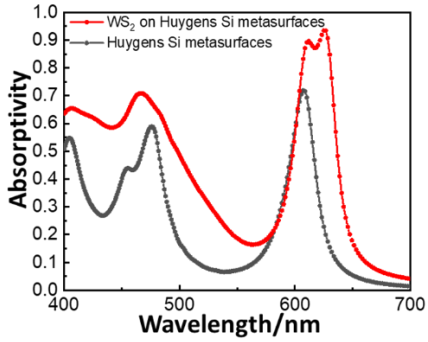

Figure 3.12 Absorption spectra of Huygens metasurface at h = 92 nm (black) and WS_2 placed on the metasurface (red).

When a monolayer of WS_2 is placed on the Si Huygens metasurface, the system exhibits two prominent absorption peaks at approximately 610 nm and 628 nm. These peaks have magnitudes of 0.90 and 0.93, respectively, which indicates that the absorption is close to unity. The appearance of two enhanced peaks indicates that the exciton still interacts with the ED resonances, which results in the formation of hybrid optical states with significantly increased coupling strength. Several spectral features arising from high-order or multipolar Mie resonances at shorter wavelengths are beyond the primary focus of this chapter and therefore are not examined in depth.

To quantitatively determine the resonance characteristics, the determination of the peak positions is given by the Lorentzian fitting as shown in Fig. 3.13. The linewidth of peak A w = 14.4 nm, while its peak amplitude is 0.65 at 627.5 nm; The peak B has a linewidth w of 18.62 nm, a peak position of 609.1 nm, and a peak value of 0.70.

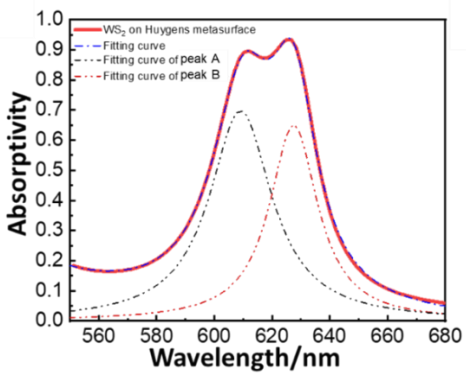

Figure 3.13 Fitting curves to the absorption peaks in Fig. 3.10 for WS_2 on the Si Huygens metasurface.

To quantitatively assess the enhancement of excitonic absorption in monolayer WS_2, the PB extraction method was employed to isolate the intrinsic absorption contribution. The extracted absorption spectrum of WS_2 placed on the Si Huygens metasurface is shown in Fig. 3.14(a). For comparison, we also evaluated the absorption of WS_2 supported on a planar Si–quartz film, as illustrated in Fig. 3.14(b). To ensure that the optical environments on both platforms remained consistent, the Si layer in the Si–quartz structure was designed with the thickness of 92 nm, identical to the height *h* of the Si cylinders used in the metasurface.

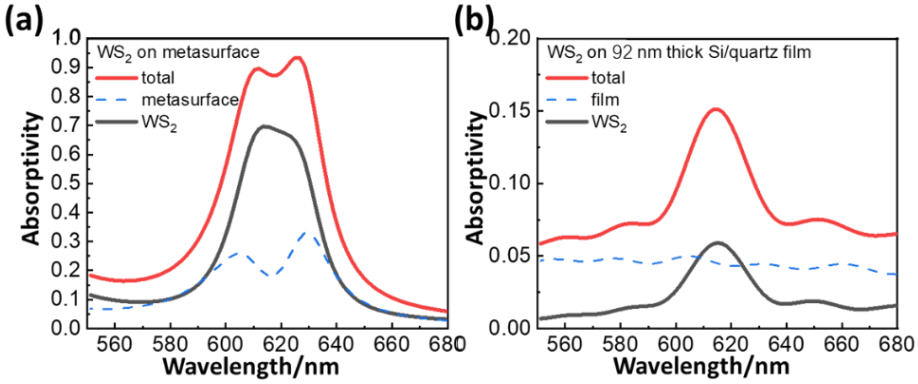

Figure 3.14 Decomposed absorption spectra of WS_2 on (c) Huygens metasurface, and (d) 92 nm-thick Si–quartz film. The Si cylinder height in (c) and the Si film thickness in (d) are kept identical.

A comparison among three configurations is presented in Fig. 3.15, which are WS_2 on the Si Huygens metasurface, WS_2 on the metasurface supporting only the ED mode, and WS_2 on the Si–quartz film. The corresponding peak absorption values extracted from PB analysis are 0.70 for the Huygens metasurface, 0.55 for the ED-mode metasurface, and 0.059 for the Si–quartz film.

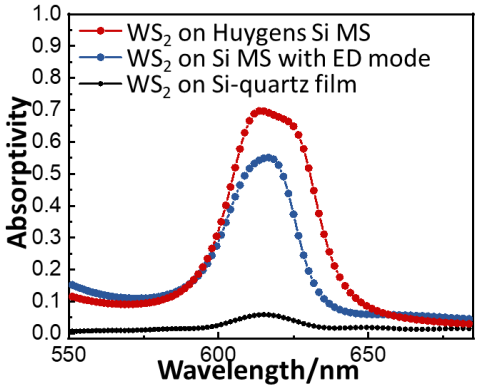

Figure 3.15 Extracted absorption spectra for WS_2 on Huygens metasurface, metasurface supporting ED mode and Si-quartz film in Fig. 3.8 and Fig. 3.12.

These results highlight the substantial advantage provided by the Huygens metasurface. The absorption of WS_2 on this structure increases by 0.64 compared with that on the Si–quartz film,

corresponding to an improvement of approximately twelve times. When benchmarked against WS_2 on a bare Si substrate and against the suspended monolayer in Fig.1.8 and 1.10, the enhancement factors reach eighteen-fold and seven-fold, respectively. This systematic comparison demonstrates that simultaneous excitation of the ED and MD resonances significantly amplifies the light–matter interaction and establishes the Si Huygens metasurface as a highly efficient platform for excitonic absorption engineering. Under the DCC condition, the presence of the MD mode provides an additional channel for coherent interaction with the exciton, which results in a further increase of approximately 0.15 in peak absorption relative to the ED-only structure.

To investigate the physical origin of the enhanced absorption, we simulated absorption spectral maps of the WS_2 monolayer together with the Mie resonances of the dielectric metasurface, as presented in Fig. 3.16. From the combined analysis of Figs. 3.13 and 3.16, we extracted the Rabi splitting strength Ω_n increasing to approximately 57 meV. This value is larger than the splitting of about 42 meV observed when the exciton couples only to the ED mode.

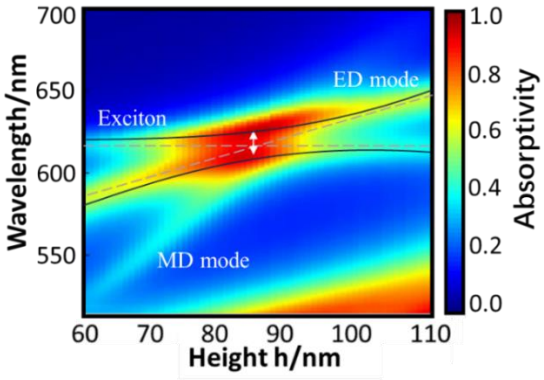

Figure 3.16 Absorption spectral map of WS_2 on the metasurface as a function of height *h*.

The enhancement can be traced to the introduction of the MD mode, which couples predominantly to the upper polariton mode (UPM) and thereby modifies the photonic environment on the exciton as shown in Fig. 3.17. Although both branches originate from the same exciton–ED coupling, they possess distinct electromagnetic field profiles, symmetries, and radiation characteristics. The MD mode has a very specific field distribution: it carries a strong tangential electric field, with a fixed phase relation determined by the Mie-type MD. As a result, the MD mode can only couple efficiently to the polariton branch whose spatial field distribution matches this symmetry. In practice, this is typically the more photonic branch (often the UPM), whose electric field near the resonator exhibits a similar tangential pattern and non-zero overlap with the MD mode. Thus, the MD mode does not couple to both branches simultaneously; instead, it selectively couples to the branch with the appropriate field symmetry and spatial overlap.

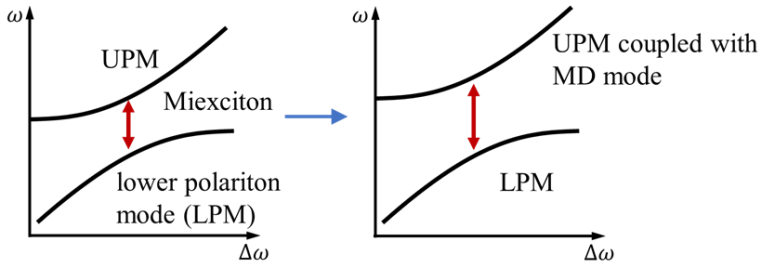

Figure 3.17 Schematic illustration of the reason for enhancement of coupling between the 2D exciton and the ED mode.

Three principal mechanisms might result in the increased splitting. First, interference between the ED and MD radiation channels suppresses radiative loss and thus raises the effective quality factor of the photonic resonance. According to the usual expression 3.7 for coupling, a decrease of the photonic loss term κ increases the measured splitting even if the intrinsic coupling constant g remains unchanged. Based on the fitting parameters in Fig. 3.18, the loss difference $\kappa - \gamma$ was extracted as 16.8 meV, while for the ED-mode-only case, the loss difference is 28.6 meV. This reduction in loss difference indicates improved balance between the photonic dissipation rate and the excitonic nonradiative loss. As a result, the spectral splitting becomes more pronounced, and the hybridization strength increases accordingly.

Second, the ED–MD hybrid supermode concentrates a stronger local electric field at the WS_2 plane shown in Fig. 3.17 compared with inset of Fig. 3.8. This enhanced the interaction with the excitonic transition and consequently increased the degree of coherent coupling between the exciton and the ED mode [154]. Meanwhile, the analysis also suggests that the ED mode plays the leading role in determining the local electric-field strength near the WS_2 layer. The spatial distribution of the electric-field intensity in the *xz*-plane at representative wavelengths is presented in Fig. 3.18. At 560.45 nm, the Mie resonance exhibits a characteristic MD profile, while at 616.74 nm, the field distribution is consistent with an ED mode. These results are in agreement with the dispersion behavior shown in Fig. 2.12, where the ED and MD resonances converge within this spectral interval.

At 584.31 nm, the calculated field distribution clearly indicates a hybrid state in which features of both the ED and MD modes are present. Near the absorption wavelength of WS_2, a similar hybridization occurs; however, the electric-field pattern is dominated by characteristics of the ED mode. This indicates that the ED resonance provides the primary contribution to the field enhancement at the exciton energy. Such concentration of electromagnetic energy near the WS_2 monolayer further intensifies the coherent exciton–photon interaction, thereby amplifying the excitonic absorption.

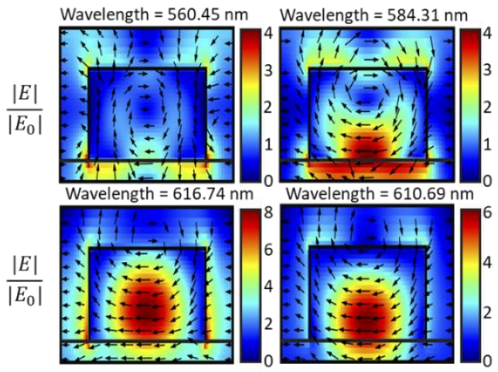

Figure 3.18 Schematic illustration of the reason for enhancement of coupling between the 2D exciton and the ED mode.

Third, genuine tri-mode hybridization redistributes modal weights among the three oscillators; the new eigenstates are different linear combinations of exciton, ED and MD, pushing the polaritonic branches further apart in energy.

These results demonstrate that designing the ED and MD resonances to overlap spectrally with the WS_2 exciton significantly enhances the absorption efficiency. The DCC strategy enables a more coherent exchange of energy between the photonic modes and excitons, therefore increasing the total absorption. This effect leads to the formation of hybrid states with substantially strengthened light–matter interaction and near-unity absorption performance.

Chapter 4 Hybrid 2D material-dielectric

This chapter systematically investigates the transfer, optical characterization, and light–matter interaction properties of monolayer WS_2 integrated with a Si Huygens metasurface. The WS_2–Huygens metasurface system is established as a tunable and robust platform for investigating and enhancing exciton–photon interactions in 2D materials, providing solid experimental and theoretical foundations for future optoelectronic and photonic applications.

A surface-energy-assisted transfer strategy was developed to realize the integration. Raman and PL mapping confirmed the successful placement and structural integrity of the transferred monolayer, accompanied by pronounced enhancement. By spectrally matching the Mie resonance of the metasurface with the excitonic transition of WS_2, clear Rabi splitting was observed in the absorption spectra, demonstrating the formation of Miexciton hybrid states. PL measurements revealed an average 18-fold emission enhancement, which is attributed to the combined effects of near-field excitation enhancement and LDOS modification by the metasurface. Power-dependent PL further uncovered a coupling transition from exciton–Mie to trion–Mie interactions at higher excitation densities. In addition, angle-resolved simulations and extension to other TMDC materials demonstrated that the absorption enhancement is robust against incident-angle variation and broadly applicable across different 2D semiconductors.

4.1 Transfer method of 2D TMDCs

The transfer of 2D materials onto target substrates is a crucial step in device fabrication and heterogeneous structure assembly. Conventional transfer approaches primarily include mechanical exfoliation and polymer-assisted deterministic placement. Mechanical exfoliation using adhesive tapes produces high-quality flakes and remains one of the most widely adopted methods for fundamental studies. However, for practical integration, polymer-assisted transfer techniques such as PDMS-based dry stamping have become dominant. In typical PDMS-assisted transfer, the 2D flake is first exfoliated onto a viscoelastic PDMS surface, and subsequently released onto the desired substrate through controlled mechanical peeling. This method offers good spatial control and minimal chemical contamination, and it is compatible with a wide variety of 2D materials.

Despite these advantages, transferring 2D materials onto optical metasurfaces remains challenging. Metasurfaces usually consist of arrays of high–aspect-ratio nanostructures, creating a topography with significant height variations. The inherent stiffness of PDMS causes poor conformal contact with such uneven surfaces, leading to incomplete release, trapped bubbles, or mechanical damage to the 2D layer. As a result, standard PDMS stamping cannot reliably achieve uniform transfer onto nanostructured substrates.

To overcome the difficulties, we first adopt a dry-release transfer method based on poly (propylene) carbonate (PPC) films [155]. This strategy takes advantage of the temperature dependence of PPC's viscosity, which provides tunable adhesion for picking up and releasing ultrathin flakes. As illustrated in Fig. 4.1, the PPC-assisted transfer process consists of two major steps: a picking-up step and a dropping-down step. In the picking-up stage, the 2D material is brought into gentle contact with a PPC-coated stamp at a temperature where the polymer becomes sufficiently soft to conform to the flake surface and adhere to it. During the dropping-down stage, the system is heated to a temperature at which PPC weakens its adhesion to the 2D material while maintaining mechanical integrity. This enables controlled release of the WS_2 monolayer onto the metasurface without introducing significant stress or fractures.

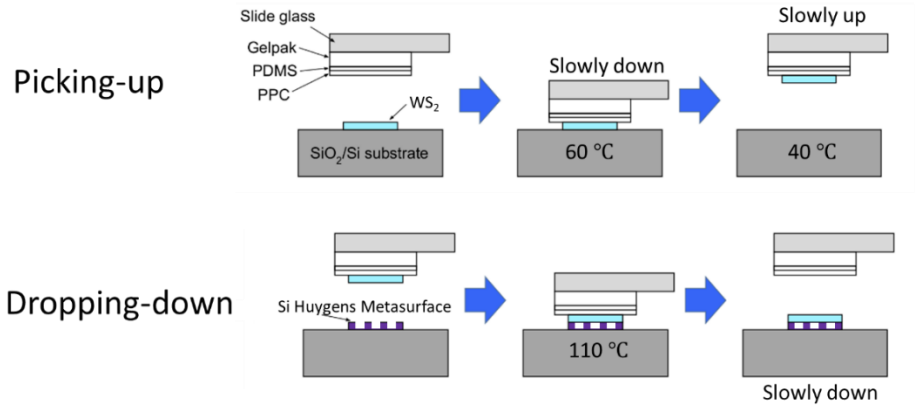

Figure 4.1 Flow diagram of dry-release transfer method of WS_2.

However, during the experimental trials, we found that the adhesion strength of PPC during the dropping-down stage was comparable to the adhesion between WS_2 and the metasurface. This resulted in an unstable release process and made the transfer considerably challenging. In addition, the monolayer WS_2 flakes used here were prepared via mechanical exfoliation, and their lateral dimensions were relatively small. To visualize the entire flake during transfer, a low-magnification objective was required, but this inevitably reduced the visibility of the monolayer region and further increased the difficulty of accurate alignment and placement. Another limitation of the PPC-assisted method arises from polymer residues. The release of PPC onto nanostructured metasurfaces often leaves behind thin but persistent polymer contaminants. Such residues are difficult to remove due to the high-aspect-ratio geometry of the metasurface, and they may interfere with subsequent optical measurements or degrade device performance. These practical issues reduce the reliability of the PPC dry-release process when applied to metasurface-supported 2D materials.

Given the limitations encountered with PPC-assisted dry transfer, we ultimately adopted a different strategy. A commercially grown monolayer WS_2 film (See more detail in Appendix) on a sapphire substrate [156] was employed, which effectively resolved the issue of insufficient flake size associated with mechanically exfoliated samples. In addition, we utilized a surface-energy-assisted transfer technique for 2D materials [157], which avoids the weak-adhesion issue between WS_2 and the metasurface encountered in the PPC transfer process.

The complete transfer procedure is illustrated in Fig. 4.2. First, a thin polystyrene (PS) supporting layer was spin-coated onto the WS_2 monolayer and subsequently baked at 80–90 °C for 15 minutes to solidify the polymer film. A small droplet of deionized water was then placed on the PS-coated surface. Owing to the surface-energy contrast between hydrophobic WS_2 and the hydrophilic sapphire substrate, water is thermodynamically capable of penetrating the

interface. However, spontaneous intercalation does not occur because the as-grown WS_2 film adheres strongly to the substrate. To initiate the process, a sharp probe was used to gently introduce microcracks at the edge of the PS/WS_2 stack. These cracks provided entry points for the water molecules, which rapidly infiltrated the interface and lifted the WS_2 film from the sapphire substrate. Once detached, the WS_2/PS stack floated on the water surface. (See video from https://doi.org/10.1364/OL.579124.)

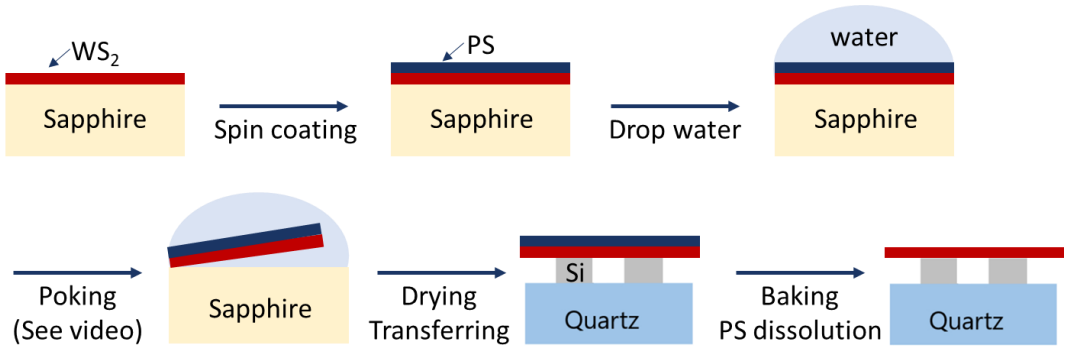

Figure 4.2 Flow diagram of surface-energy-assisted transferring process of WS_2.

After removing the water droplet with a lint-free tissue, the floating stack was carefully retrieved with tweezers and brought into contact with the Si metasurface. The sample was then baked at 80 °C for one hour to eliminate residual moisture. A subsequent annealing step at 150 °C for 30 minutes softened the PS film, relaxed wrinkles, and improved conformal contact with the metasurface topography. Finally, the PS support layer was dissolved in toluene, leaving behind a clean, uniformly transferred WS_2 monolayer.

This water-assisted intercalation method, combined with the PS support layer, provides a reliable route for transferring large-area CVD-grown WS_2 onto nanostructured metasurfaces. It avoids the adhesion mismatch and polymer residues associated with PPC-based processes, while ensuring high transfer yield of the monolayer film.

However, transferring the WS_2 monolayer onto the metasurface presented an additional practical challenge. The size mismatch between the metasurface and the sapphire substrate, combined with the presence of vertically structured cylindrical resonators, introduced significant mechanical stress during the transfer process. This stress led to partial tearing and fragmentation of the monolayer WS_2 within the metasurface region, as shown in Fig. 4.3. Several broken fragments reached lateral dimensions of up to 8 μm, which is still larger than incident light spot size of 2 μm used in the optical measurements. In comparison, the WS_2 film transferred onto the quartz substrate, although subject to a similar size mismatch, remained largely intact and continuous. The absence of high-aspect-ratio features on the quartz surface prevented the stress

concentration observed in the metasurface case, resulting in a much more uniform and unbroken monolayer.

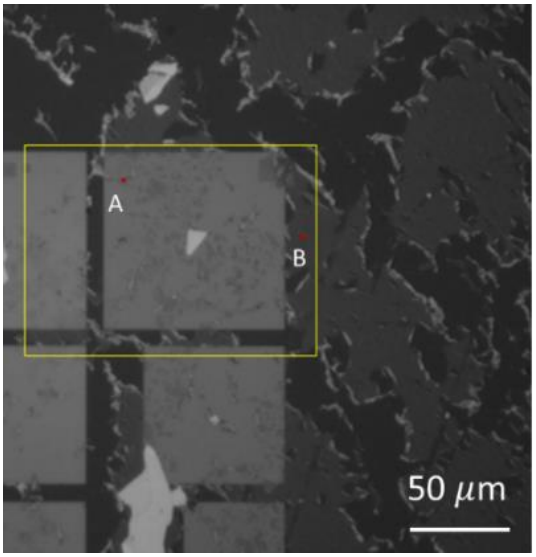

Figure 4.3 Optical microscopy image of WS_2 transferred onto the metasurface.

4.2 Basic characterization of hybrid system

To evaluate the structural integrity of the transferred monolayer and verify its successful placement on the metasurface, both Raman and PL measurements were performed. Raman and PL spectra were acquired using a laser Raman microscope system (Raman 11) with a 532 nm continuous-wave laser as the excitation source. The laser beam was focused onto the sample through a 50× objective lens, yielding a spot size of approximately 1–2 μm. For Raman measurements, the excitation power was fixed at 1 mW and the integration time was set to 60 s. PL spectra were recorded under excitation powers ranging from 0.05 mW to 5 mW, while maintaining identical exposure times for all measurements to enable reliable power-dependent analysis. All optical emission measurements, including both Raman scattering and PL, were conducted under normal-incidence geometry. The experimental setups are schematically illustrated in Fig. 4.4.

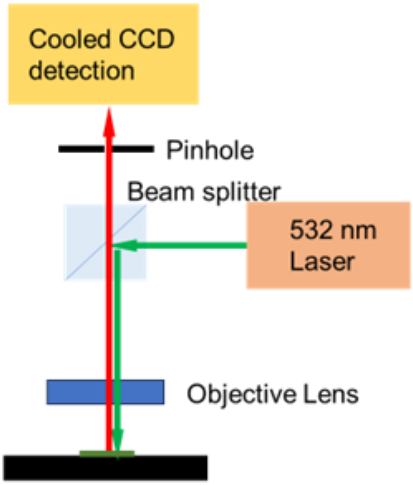

Figure 4.4 Schematic of the Raman and PL spectra measurement setup.

Raman scattering measurements were conducted at two representative locations: one on the metasurface and the other on the adjacent quartz region. The Raman spectra are presented in Fig. 4.5(a), where the red and black curves correspond to points A and B in Fig. 4.3, respectively. To clearly show the peak position comparation, we normalized the Raman spectrum shown in Fig. 4.5(b). Two prominent Raman modes of WS_2 are clearly observed at 339 cm^{-1} and 404 cm^{-1}, corresponding to the in-plane E^1_{2g} mode and the out-of-plane A_{1g} mode. The measured peak separation of 65 cm^{-1} is consistent with reported values for monolayer WS_2 [158], confirming that the transferred process is successed for the monolayer WS_2 of sufficient size for optical testing. A Si -related Raman peak at 505 cm^{-1} is also visible in the spectrum collected from the metasurface area.

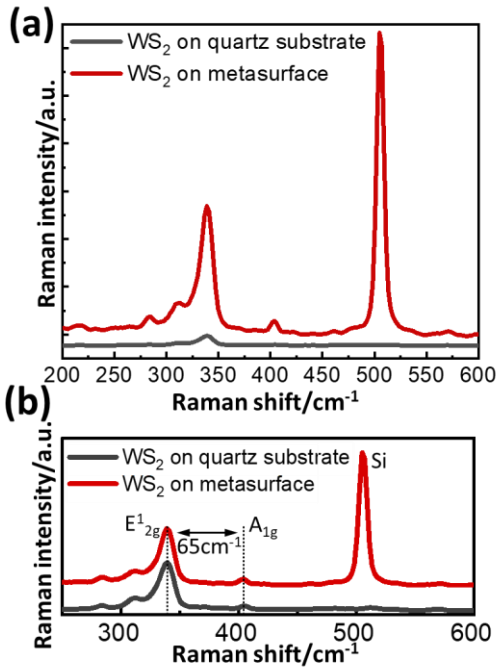

Figure 4.5 (a) Raman spectra of WS_2 on quartz substrate (black line) and metasurface (red line), and (b) normalized Raman spectra.

The Raman signal intensity is significantly enhanced at the metasurface location. To remove the enhancement effect caused by PL, we normalize the noise floor as much as possible, as shown in Figure 4.6, showing 14-fold and 20-fold increases for the two characteristic modes. This enhancement is attributed to the strong local field concentration and modified scattering environment produced by the Mie resonators.

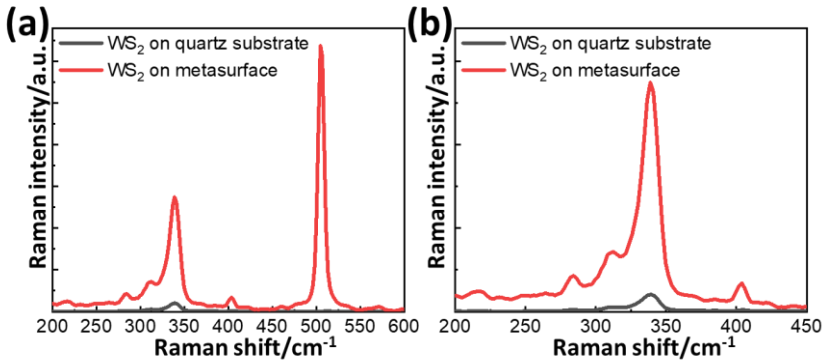

Figure 4.6 Normalized Raman spectra from Fig. 4.5.

Similar levels of enhancement were repeatedly observed at different positions across the metasurface shown in Fig. 4.7, indicating that the Raman amplification is spatially uniform over the successfully transferred monolayer WS_2.

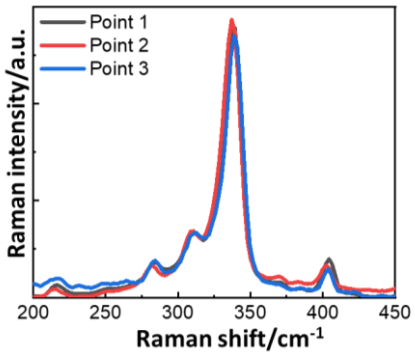

Figure 4.7 Normalized Raman spectra in different point of WS_2 on the metasurface.

For near-field–enhanced Raman scattering, it is commonly assumed that the total enhancement factor G can be decomposed into two independent contributions corresponding to the excitation process and the emission process. Under this approximation, the overall enhancement can be expressed as [159]:

$$G \approx \frac{|E_{loc}(\omega_i)|^2}{|E_0|^2} \times \frac{|E_{loc}(\omega_s)|^2}{|E_0|^2} \times \frac{\Gamma_{rad}(\omega_s)}{\Gamma_0(\omega_s)} \tag{4.1}$$

ω_i denotes the angular frequency of the incident pump light and ω_s denotes the angular frequency of the Stokes emission. $E_{loc}(\omega)$ is the local electric field experienced at the WS_2 position, whereas E_0 is the amplitude of the incident plane-wave field used as a reference. The ratio $\frac{\Gamma_{rad}(\omega_s)}{\Gamma_0(\omega_s)}$ describes the radiative rate at the emission wavelength relative to that in free space. It indicates that the phonon–photon interaction probability can be significantly enhanced by the strong local electromagnetic fields provided by the Mie resonators at both the excitation and emission wavelengths, such as through higher-order resonant modes, thereby leading to an increased Raman scattering intensity. In our simulations the product of the two local-field factors $\frac{|E_{loc}(\omega_i)|^2}{|E_0|^2} \times \frac{|E_{loc}(\omega_s)|^2}{|E_0|^2}$ is approximately 5.06. The experimentally measured Raman enhancements of approximately 14 and 20 times therefore demand an additional emission-side amplification factor. Another important origin of the Raman intensity increases lies in the modification of the local density of optical states (LDOS) and the associated change in radiation directivity, which together facilitate more efficient out-coupling of the scattered photons [160].

The disparity between the enhancement factors of the two Raman modes can be attributed to their different Raman tensor symmetries. Specifically, the E^1_{2g} mode primarily couples to in-

plane electric field components, whereas the A_{1g} mode is mainly sensitive to out-of-plane fields [161]. Because Mie-type resonators generate localized near fields with different relative strengths of the in-plane ($E_{\parallel}$) and out-of-plane ($E_{\perp}$) components at the excitation wavelength, those Raman modes whose tensors are better aligned with the dominant local field components experience stronger enhancement. This interpretation is further corroborated by the simulated electric field distribution at 532 nm shown in Fig. 4.8. At the WS_2 position, the out-of-plane field component is clearly stronger than the in-plane component, which is consistent with the experimentally observed larger enhancement of the A_{1g} mode.

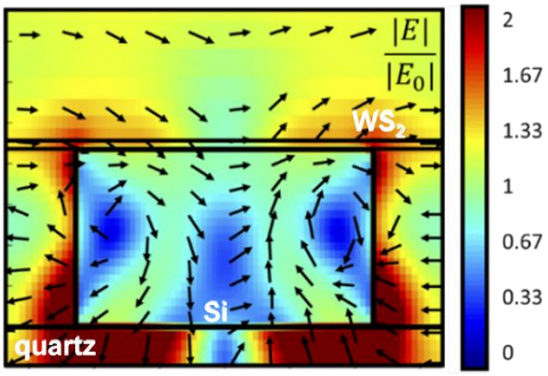

Figure 4.8 Normalized electric field distributions of higher-order Mie mode in the x – z plane. E_0 is the amplitude of the incident electric field.

Raman mapping measurements were conducted to confirm the successful transfer and to examine the spatial distribution of the monolayer WS_2. Figure 4.9 (a) presents the Raman intensity map of the characteristic Si peak, while Fig. 4.9 (b) displays the Raman intensity distribution of the WS_2 monolayer. Their spatial overlap is shown in Fig. 4.9 (c), clearly revealing that the WS_2 flake is positioned on the metasurface area. To further verify the presence and uniformity of the transferred monolayer WS_2, PL mapping was performed, as shown in Fig. 4.9 (d). Owing to the relatively high excitation power and extended exposure time during the PL measurement, most regions exhibiting PL signals appear overexposed and saturated in the mapping image. Nevertheless, the strong and continuous PL response across the metasurface region unequivocally confirms both the existence and the spatial distribution of the monolayer WS_2. Although partial fragmentation of the WS_2 film occurred during the transfer process, the PL intensity in the central region remains significantly higher than that at the edges. This observation indicates that the subsequent absorption and PL enhancement discussed below cannot be attributed to edge-related effects, but instead arise from the intrinsic light–matter interaction within the metasurface region.

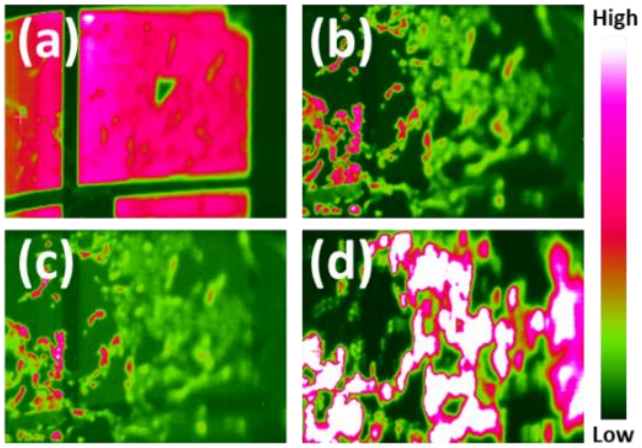

Figure 4.9 (a–c) Spatial Raman and PL mapping of monolayer WS_2 transferred onto a Si metasurface. (a) Raman intensity map of the Si-related peak at 505 cm^{-1}, where the high-intensity (pink) region indicates the location of the Si metasurface. (b) Raman intensity map of monolayer WS_2, obtained by combining the intensities of the in-plane E^1_{2g} mode and the out-of-plane A_{1g} mode, showing the spatial distribution of the WS_2 flake. (c) Spatial overlap map generated by superimposing the Raman maps in (a) and (b). (d) PL intensity map collected from the same region as shown in (c). The color scale represents the Raman/PL intensity.

4.3 Absorption measurement of metasurface

Our previous work has demonstrated that both ED and MD resonances contribute effectively to the enhancement of light absorption in WS_2. When the structural parameters are tuned to p = 334 nm, r = 112 nm, and h = 92 nm, the metasurface satisfies the DCC condition, under which the ED and MD modes spectrally overlap. At this degeneracy point, a Huygens metasurface is formed, enabling constructive interference between the electric and magnetic responses and thereby providing an optimal platform for amplifying the absorption of the WS_2 monolayer.

For the absorption measurements, a supercontinuum white-light source (SuperK COMPACT, NKT Photonics) was employed as the broadband illumination source and focused onto the sample through a 20× objective lens, yielding a focal spot diameter of approximately 2 μm. The total optical power in the visible spectral range from 450 to 850 nm exceeded 20 mW and was kept constant for all measurements to ensure consistent experimental conditions and reliable comparison among different samples. Reflection and transmission spectra were recorded under normal-incidence geometry. The detailed optical measurement setups are schematically shown in Fig. 4.10.

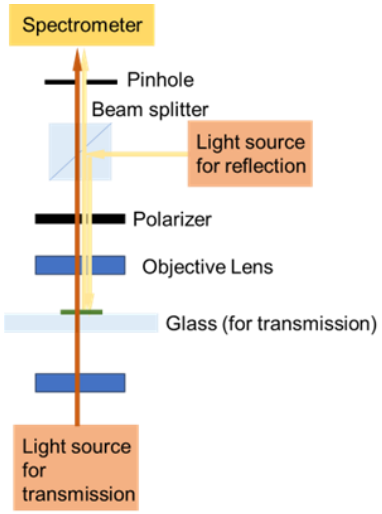

Figure 4.10 Schematic of the absorption spectra.

To realize the formation of Miexciton hybrid states and enable reliable extraction of the Rabi splitting, it is necessary to spectrally align the photonic resonance of the metasurface, denoted as ω_{Mie}, with the excitonic resonance ω_{ex} of monolayer WS_2. This condition corresponds to zero detuning, defined as $\Delta = \omega_{Mie} - \omega_{ex} = 0$, under which exciton–photon coupling is maximized and the energy separation between the upper and lower hybrid branches reaches its maximum value [150]. At zero detuning, the splitting energy directly reduces to $\Omega_n = 2g$, where g denotes the coherent coupling strength. This relation provides a clear and direct criterion for identifying and quantifying Rabi splitting.

Based on both electromagnetic simulations and experimental characterization, the excitonic resonance position of monolayer WS_2 was precisely determined. The simulated absorption spectrum of monolayer WS_2 reveals a pronounced A-exciton absorption peak near 615 nm shown in Fig. 1.8 and Fig. 1.10. This result was further validated experimentally by measuring the reflection spectrum of WS_2 on a sapphire substrate, as shown in Fig. 4.11, where a distinct reflection feature associated with excitonic absorption is observed at the same wavelength.

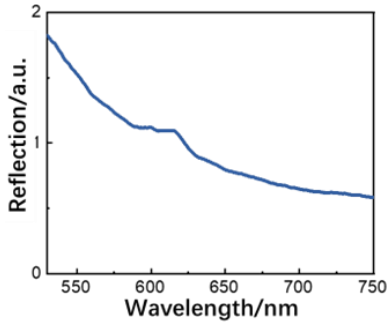

Figure 4.11 Reflection spectrum of monolayer WS_2 on the sapphire substrate.

During fabrication, however, the electron-beam lithography (EBL) process can introduce slight deviations in the structural dimensions due to proximity effects, resist heating, and charge accumulation, which may induce unintended shifts in the resonance wavelength. To compensate for these effects, a series of metasurface samples were fabricated with systematically varied exposure doses and cylinder diameters. Among these, the sample whose experimentally measured Mie resonance was centered at 615 nm was selected for the coupling experiments. Consequently, the photonic Mie resonance was experimentally matched to the WS_2 excitonic transition, ensuring the validity and accuracy of direct Rabi splitting extraction from the measured absorption spectra.

Figure 4.12 presents the experimentally measured reflectance, transmittance, and absorption spectra. The absorptivity was obtained as $A = 1 - R - T$. A pronounced Mie-resonant absorption peak is observed at 615 nm with a maximum value of 0.70.

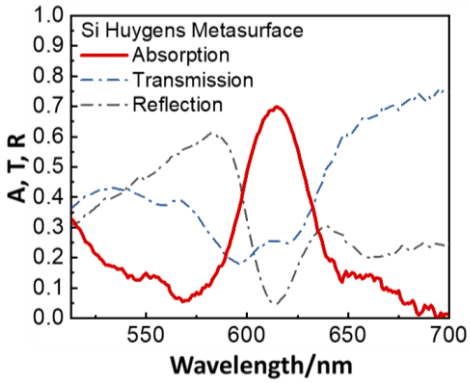

Figure 4.12 Experimental reflectance, transmittance, and absorption spectra of Mie resonators based on MD & ED modes.

To further verify the fabricated structural parameters, focused ion beam (FIB) imaging was employed to characterize the geometry of the metasurface, as shown in the Fig. 4.13. The FIB image was acquired at a tilt angle of 30°, from which the structural dimensions were estimated to be $r \approx 114$ nm, $p \approx 334$ nm, and $h \approx 86$ nm.

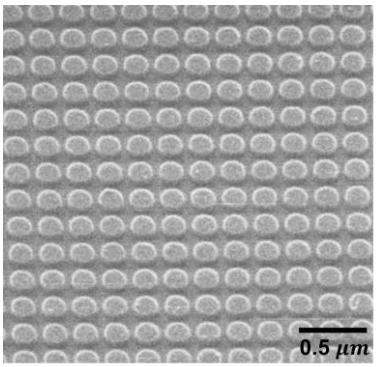

Figure 4.13 Focused ion beam (FIB) image of the sample.

Based on these values, the experimentally measured resonance spectrum was subsequently fitted, as presented in Fig. 4.14. Although the fabricated height is slightly smaller than the nominal design value, leading to a minor deviation from the ideal spectral overlap between the ED and MD modes, the two resonances still remain nearly degenerate.

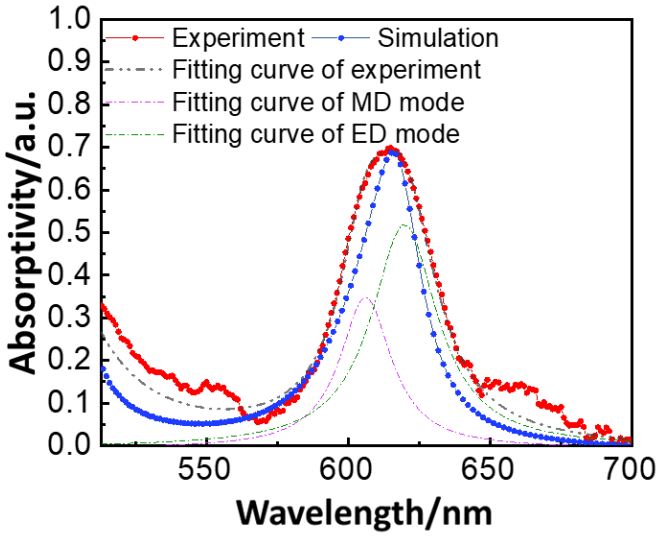

Figure 4.14 Comparison of experimental and simulated absorption spectrum, with the experimental peak fitted using contributions from different Mie modes.

Numerical simulations were then carried out using the FIB-derived geometric parameters with slight fine-tuning to account for fabrication uncertainties. As shown in Fig. 4.14, for r = 114.20 nm, h = 86.40 nm, and p = 334.00 nm, the simulated Mie resonance peak appears at 615 nm with an absorptivity of 0.69, in excellent agreement with the experimental data in terms of both resonance wavelength and peak amplitude. The slightly lower simulated absorption compared with the experimental value suggests that the extracted parameters may not fully represent the exact physical structure but provide a reasonable approximation. Moreover, the experimentally observed resonance remains broader than the simulated counterpart. In addition to fabrication tolerances, this spectral broadening and the minor discrepancies are attributed to surface roughness, which introduces additional scattering losses.

4.4 Absorption measurement of WS_2-metasurface

We subsequently integrated monolayer WS_2 onto the optimized Huygens Si metasurface. Based on our previous numerical optimization, the structural parameters p = 334 nm, r = 112 nm, and h = 92 nm were selected to achieve maximum excitonic absorption enhancement. To validate

the simulation results, we experimentally measured the reflectance and transmittance spectra of the fabricated sample and derived the corresponding absorption, as presented in Fig. 4.15. The experimental spectrum also exhibits a clear double-peak absorption feature, with maxima located at 600 nm and 616 nm. Both peaks reach an absorptivity of approximately 0.84. Compared with the simulated results, the experimental resonances show an overall blue shift and a slight reduction in peak intensity, which can be attributed to fabrication-induced dimensional deviations and additional material losses.

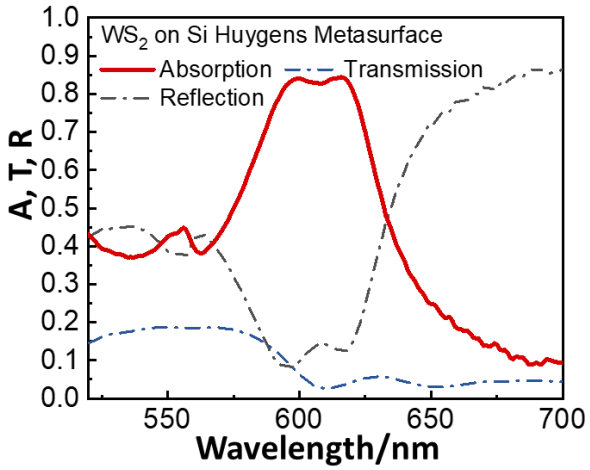

Figure 4.15 Measured reflectance, transmittance, and absorption spectra for WS_2 on the Huygens metasurface.

Since the condition of zero detuning $\omega_{Mie} = \omega_{ex}$ is satisfied, the Rabi splitting energy can be directly obtained from the energy separation between the two hybrid peaks. Experimentally, the peak separation increases from 13 nm, corresponding to approximately 42 meV, to 16 nm, which corresponds to about 54 meV. This increase indicates that the Rabi splitting strength is further enhanced in the fabricated structure.

To determine the coupling regime between the WS_2 exciton and the Mie resonances, Lorentzian fitting was applied to the experimentally measured absorption spectrum shown in 4.15. As illustrated in Fig. 4.16(a), two distinct hybrid absorption peaks were resolved at wavelengths of 619 nm and 595 nm, corresponding to photon energies of 2.00 eV and 2.08 eV, respectively. The energy separation between these two hybrid modes yields a Rabi splitting energy of Ω_n = 80.8 meV, indicating the formation of exciton–photon hybrid states.

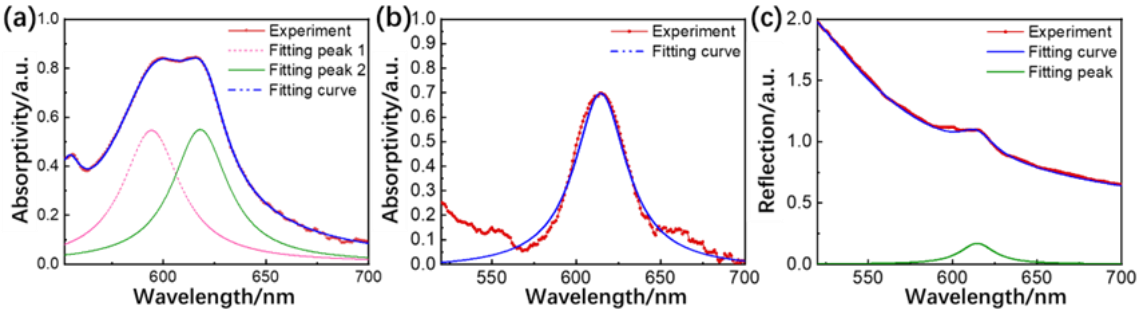

Figure 4.16 Comparison between experiment and fitted absorption spectra in (a) Fig. 4.15, (b) absorption in Fig. 4.12, and (c) reflection in Fig. 4.11.

To evaluate the dissipation rates of the uncoupled constituents, Lorentzian fitting was further performed on the bare spectra of the individual systems, as shown in Fig. 4.16(b) and Fig. 4.16(c). The half-width at half maximum w of the monolayer WS_2 exciton resonance is 25 nm, while that of the bare metasurface resonance is 38 nm. These linewidths correspond to energy damping rates of γ_1 = 82.0 meV for the exciton and γ_2 = 124.6 meV for the Mie mode, respectively. These parameters account for the total dissipation, including both radiative and nonradiative loss channels.

According to the criterion for intermediate coupling [4],

$$\frac{|\gamma_1 - \gamma_2|}{2} < 2g < \frac{\gamma_1 + \gamma_2}{2} \tag{4.2}$$

where $2g = \Omega_n$, the experimentally extracted splitting energy $2g = \Omega_n = 80.8$ meV satisfies this inequality. This result unambiguously confirms that the WS_2–Mie hybrid system operates in the intermediate exciton–photon coupling regime.

Furthermore, absorption spectral mapping was carried out by systematically varying the resonator radius *r*, as shown in Fig. 4.17. Based on our previous studies, both hybrid absorption peaks exhibit a blue shift as the cylinder height decreases. Therefore, to isolate the influence of the lateral dimension, the height was fixed at h = 86.40 nm, as determined from the FIB measurements and the preceding simulations, while the radius was continuously tuned. This approach enabled us to track the evolution of the hybrid modes as a function of geometric confinement.

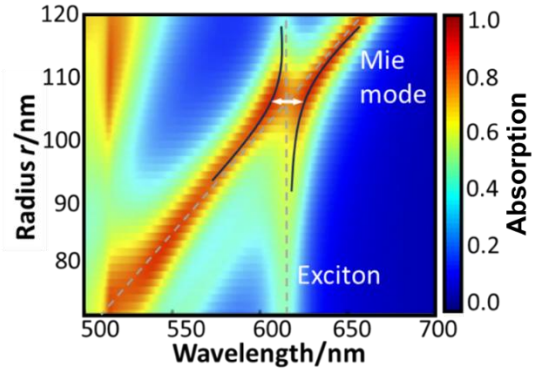

Figure 4.17 Absorption spectral map of WS_2 on metasurface as a function of resonator radius *r*.

The resulting dispersion map clearly reveals the emergence of mode splitting as the ED resonance is tuned through the excitonic transition. A pronounced Rabi splitting is observed, with the maximum splitting energy Ω_n reaching approximately 40 meV at an optimal radius of r =107 nm. These observations provide direct evidence of coherent exciton–photon interaction in the WS_2–metasurface system and validate the geometric tunability of the coupling strength.

The Rabi splitting energy Ω_n is quantitatively described by the expression 3.7.

Based on the dispersion map in Fig. 4.17, the resonator radius *r* corresponding to the best spectral agreement between simulation and experiment in Fig. 4.15 was identified. Using this optimized radius and setting the cylinder height to h = 101 nm, the simulated absorption spectra shown in Fig. 4.18 were obtained. Although the spectral positions of the two hybrid peaks are well reproduced by the simulation, their amplitudes are slightly lower than those observed experimentally, with simulated peak absorptivity of 0.78 and 0.77, respectively.

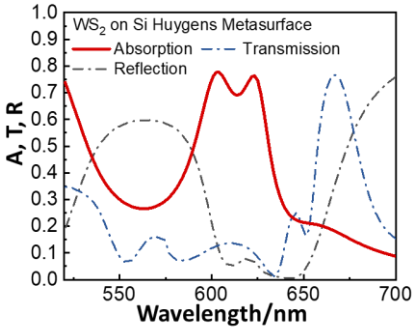

Figure 4.18 Simulated absorption spectra after parameter adjustment.

To further quantify the intrinsic contribution of the WS_2 layer, the PB extraction method was employed. As shown in Fig. 4.19, this power-flux-based extraction enables direct evaluation of the total absorption spectrum of WS_2 on the metasurface while excluding substrate contributions. From the extracted spectrum, the intrinsic absorption of WS_2 exhibits two pronounced peaks with

magnitudes of 0.62 and 0.66, respectively. These values confirm that the dominant portion of the enhanced absorption in the hybrid system originates from the excitonic response of the WS_2 monolayer.

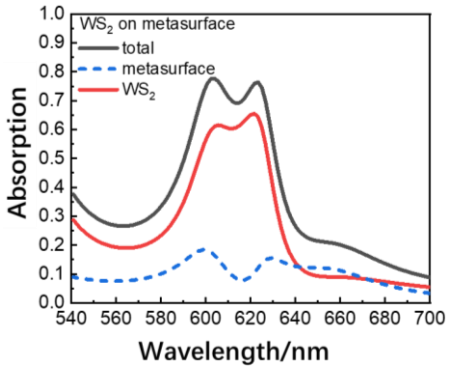

Figure 4.19 Decomposed absorption spectrum of WS_2 on metasurface.

In the experiment, surface roughness introduced during the fabrication of the Si cylinders increases both the radiative loss κ and the nonradiative loss γ of the Mie resonances. This additional dissipation leads to broadened linewidths of the hybrid absorption peaks, which in turn enhances their spectral overlap and contributes to an apparent increase in the peak absorptivity. Moreover, when the ED and MD resonances are not perfectly spectrally matched in the simulations, a characteristic shoulder associated with the ED mode appears on the long-wavelength side near 650 nm in Fig. 4.17. This feature is absent in the experimentally measured spectra, indicating that the ED and MD modes in the fabricated sample are more closely matched than in the corresponding simulation case shown in Fig. 4.18. This observation further suggests that the experimentally realized splitting strength approaches the value predicted for the original optimized design.

Because the variation in the splitting magnitude is proportional to the relative contribution of WS_2 absorption to the total Miexciton absorption, this analysis implies that the WS_2 intrinsic absorption in the experiment exceeds the simulated value of 0.62. Meanwhile, although microscope characterization reveals partial fragmentation of the transferred WS_2 monolayer, the experimentally observed absorption enhancement and peak separation remain in good agreement with the simulation results. This consistency indicates that the fragmented morphology exerts only a minor influence on the exciton–photon coupling strength and does not substantially degrade the formation of Miexciton hybrid states.

4.5 Emission measurement of WS_2-metasurface

To further verify that the intrinsic light–matter interaction of the monolayer WS_2 is substantially enhanced by the metasurface, PL measurements were conducted, as shown in Fig. 4.20. Under identical excitation and collection conditions, the monolayer WS_2 integrated on the Si metasurface (red curve) exhibits a pronounced emission peak centered at 614 nm, and the same WS_2 monolayer transferred onto a flat quartz substrate (black curve) shows a PL peak at 615 nm. The nearly unchanged peak position indicates that the electronic band structure of WS_2 is well preserved after the transfer process. In contrast, the PL intensity is enhanced on the metasurface. By averaging the PL intensity over three representative locations while deliberately avoiding local hot-spot maxima, an average enhancement factor of approximately 18 is obtained. This substantial enhancement unambiguously demonstrates that the metasurface strongly amplifies the excitonic radiative emission of WS_2, primarily through the combined effects of local electromagnetic field enhancement and modified photonic density of states.

In addition, it is worth noting that PL enhancement is not always expected to monotonically increase with stronger light–matter coupling. Previous studies on exciton–plasmon hybrid systems have shown that the emission behavior strongly depends on the coupling regime [161]. For instance, in Ag nanoparticle–TMDC heterostructures, Purcell-enhanced emission was observed in the weak coupling regime, whereas in the strong coupling regime an electromagnetically induced transparency (EIT)-like response emerged together with pronounced PL suppression. This indicates that although strong coupling enables the formation of hybrid polaritonic states, the radiative emission can be reduced due to coherent interference and the redistribution of oscillator strength into non-emissive channels.

In the present WS_2–Si metasurface system, the experimentally observed anticrossing behavior indicates that the interaction is beyond the purely weak coupling limit, while the strong PL enhancement suggests that the system does not enter the regime where destructive interference dominates the emission process. Therefore, the large enhancement factor observed here is consistent with an intermediate coupling scenario, where mode hybridization and enhanced local density of optical states coexist, allowing efficient radiative recombination while still exhibiting clear exciton–photon interaction features.

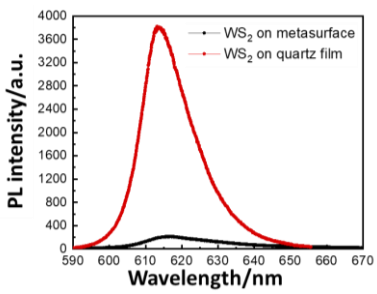

Figure 4.20 PL spectra of monolayer WS_2 on a quartz film (black line) and metasurface (red line).

The observed PL enhancement originates primarily from two mechanisms. First, the excitation efficiency is markedly improved due to the strong near-field localization induced by the overlapping Mie resonances of the Si metasurface, which locally amplify the electric field at the position of the WS_2 monolayer. Numerical simulations reveal that the normalized local electric field amplitude at the WS_2 layer reaches approximately 1.50 at the excitation wavelength of 532 nm on the metasurface, compared with only 0.85 on a flat quartz substrate. Similarly, at the emission wavelength, the local field amplitude is enhanced to about 1.55 on the metasurface, in contrast to 0.83 on quartz, as illustrated in Fig. 4.8 and Fig. 4.21, respectively.

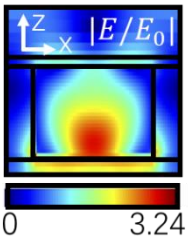

Figure 4.21 Normalized electric field distributions in the x – z plane at the emission wavelength (614 nm).

Figure 4.22(a) presents the simulated electric field intensity distribution of the monolayer WS_2 supported on a quartz substrate at the excitation wavelength, while Fig. 4.22(b) shows the corresponding distribution at the emission wavelength. In both cases, the maximum normalized electric field intensities in the reflected region are approximately 0.85 and 0.83, respectively, whereas the electric field amplitude inside the WS_2 layer remains around 0.65. These relatively modest field values indicate limited near-field confinement and weak light–matter interaction for WS_2 on the bare quartz substrate. In contrast, the metasurface-supported WS_2 exhibits substantially higher local field intensities at both excitation and emission wavelengths, as discussed above. These pronounced enhancements of the local field intensity at both the excitation and emission wavelengths significantly increase the effective excitation rate and the radiative recombination probability of excitons in WS_2 [151,152].

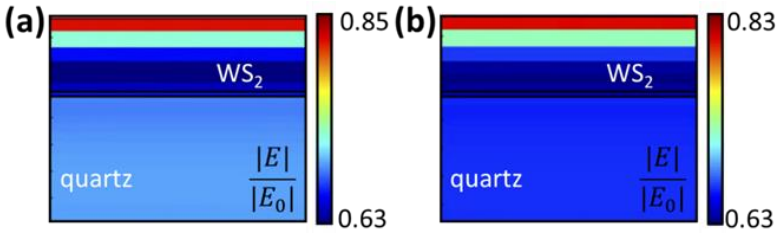

Figure 4.22 (a) Normalized electric field distributions of WS_2 on quartz film in the x – z plane at pump wavelength and (b) emission wavelength, respectively.

Second, the metasurface profoundly modifies the spontaneous emission channels by reshaping the LDOS. As shown in Fig. 4.23(a), the LDOS at the WS_2 position on the quartz substrate is approximately 124, whereas it increases to 327 on the metasurface, as displayed in Fig. 4.23(b). The LDOS distribution exhibits a pronounced central hotspot accompanied by in-plane side lobes, indicating the opening of additional radiative decay channels associated with ED-type Mie resonances [162]. Such LDOS redistribution is a hallmark of intermediate light–matter coupling and is known to markedly enhance the radiative decay rate in 2D semiconductors [4,163].

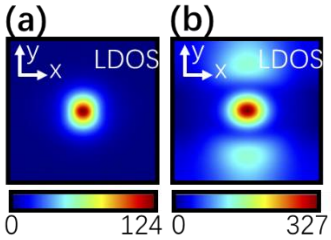

Figure 4.23 Simulated LDOS maps in the x – y plane at the emission wavelength for WS_2 on (a) the quartz film and (b) the metasurface, respectively.

It is also noteworthy that although a clear mode splitting is observed in the absorption spectra under the intermediate-coupling regime, the PL spectrum exhibits only a single dominant emission peak. The PL response of a coupled exciton–photon system does not necessarily display two well-resolved polaritonic branches, even when clear mode splitting is observed in absorption. The complementary polaritonic branch remains weak, which can be attributed to several factors, including rapid exciton thermalization through the exciton reservoir, spectral linewidth overlap of the hybrid states, and polarization-selective out-coupling efficiency [164,165].

In the present structure, the absence or strong suppression of the upper polariton branch in the PL spectrum cannot be attributed primarily to nonradiative decay. This is because the total optical loss rates, extracted from Lorentzian fitting of the absorption spectra, are of the same order of magnitude as the measured Rabi splitting energy shown in Fig.4.16. This confirms that both hybrid modes remain within a coherently coupled regime and are not overdamped by dissipation.

Instead, several physical mechanisms may account for the weak visibility of one polariton branch in PL while preserving coherent coupling. The dominant contributions are discussed below.

a) Rapid thermalization mediated by the exciton reservoir.

Under strong or intermediate coupling, the WS_2 exciton interacts with the Mie resonant mode to form two hybrid eigenstates, namely the upper and lower polariton branches (LPB), as schematically illustrated in Fig. 4.24(a). Under non-resonant optical excitation, excitons are initially generated in high-energy electronic states and subsequently undergo ultrafast energy

relaxation toward lower-energy states through scattering with phonons and interactions with the exciton reservoir, as illustrated schematically in Fig. 4.24(b). During this relaxation cascade, a large fraction of the excitonic population is funneled into the LPB. It is important to emphasize that this process represents a redistribution of population rather than genuine nonradiative loss: the excitons are not annihilated, and the coherent exciton–photon coupling is preserved throughout the relaxation dynamics. However, the consequence of this rapid thermalization is a highly asymmetric population distribution between the two polaritonic branches, in which the LPB becomes strongly populated and therefore dominates the radiative emission, while the upper polariton branch (UPB) remains only weakly occupied and emits very weakly at room temperature.

Such polariton population imbalance is a well-established phenomenon in microcavity exciton–polaritons and plasmon–exciton (plexciton) systems, where efficient phonon-assisted relaxation and reservoir-mediated scattering preferentially populate the lower branch [164,166,167]. In the present monolayer WS_2 system, the large exciton binding energy, strong exciton–phonon coupling, and the presence of an intermediate-to-strong exciton–photon coupling regime further accelerate this relaxation pathway. As a result, the PL spectrum is dominated by LPB emission even though clear mode splitting is observed in absorption, providing a consistent physical explanation for the apparent absence of the UPB in PL.

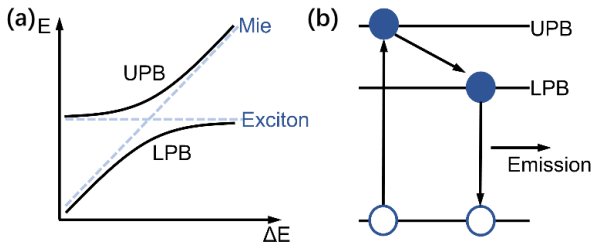

Figure 4.24. (a) Schematic illustration of the coupled WS_2 – Mie system, (b) band diagram of relaxation process.

b) Linewidth overlap and spectral masking

When the intrinsic linewidths of the excitonic and photonic resonances become comparable to or exceed the magnitude of the Rabi splitting, the two polariton branches inevitably undergo substantial spectral overlap. In the present system, the linewidths extracted from Lorentzian fitting are on the same order of magnitude as the experimentally observed Rabi splitting energy as shown in Fig. 4.16, which implies that the spectral separation between the UPB and LPB is insufficient to fully overcome their intrinsic broadening. As a result, the two

hybrid branches cannot be clearly resolved as distinct emission features in the photoluminescence spectra.

Because PL detection inherently reflects intensity-weighted emission, the strong overlap between the broadened polariton resonances leads to the appearance of a single dominant emission peak, even though the underlying hybrid mode splitting remains observable in absorption, reflection, or scattering measurements. This behavior is a hallmark of the intermediate-coupling regime, in which the excitonic and photonic damping rates are comparable to the coherent coupling strength. In this regime, coherent exciton–photon interaction persists and reshapes the optical response of the system, yet the spectral resolution of individual polariton branches in PL is fundamentally limited by dissipation-induced broadening.

c) Polarization-selective out-coupling

In the present system, the metasurface simultaneously supports ED and MD resonances with distinct polarization characteristics, corresponding to predominantly in-plane (TE-like) and out-of-plane (TM-like) electric-field components, respectively [165]. Because the optical transition dipole moment of the WS_2 exciton lies primarily within the plane of the monolayer, it couples efficiently only to the in-plane electric-field component of the resonant modes. Consequently, the polaritonic branch associated with a mode dominated by out-of-plane (TM-like) polarization experiences much weaker coupling to the exciton dipole and, moreover, radiates less efficiently into the far field [165]. This polarization-selective coupling and radiation leads to one of the hybrid branches becoming optically dark in the detected PL signal, even though it remains present in the coupled dispersion and is clearly manifested in absorption or scattering spectra [82,166].

To directly verify this polarization-selective out-coupling effect, polarization-resolved and angle-resolved PL measurements could be performed [164,167]. By selectively analyzing the emission along different polarization directions or at different collection angles, it would be possible to access polariton branches that are weak or invisible in conventional PL measurements due to their polarization mismatch with the in-plane exciton dipole or their predominantly out-of-plane radiation character. Such measurements would provide further experimental validation of the polarization-dependent emission channels and offer deeper insight into the anisotropic coupling dynamics and radiation behavior in the hybrid WS_2–metasurface system.

To further investigate the influence of light–matter coupling on the photoluminescence behavior, we performed power-dependent PL measurements of monolayer WS_2 on both quartz and the metasurface. For WS_2 on the quartz substrate, PL spectra were recorded under 532 nm

excitation at laser powers of 0.05 mW, 0.5 mW, and 2 mW, as shown in Fig. 4.25(a). Each spectrum was fitted using a two-peak Lorentzian model [168], revealing two well-resolved emission components centered at approximately 615 nm and 629 nm, corresponding to the neutral exciton (X) and negatively charged trion (X^-), respectively. The trion emission originates from the binding of a neutral exciton with an additional free electron to form a charged excitonic complex. Its presence on a nominally undoped substrate is mainly attributed to unintentional electron doping induced by surface defects, adsorbed molecules, or polymer residues remaining after the transfer process [169,170]. In our samples, fragmentation and edge damage introduced during the transfer may also contribute to such doping effects. As the excitation power increases, the peak positions remain nearly unchanged, while the relative intensities evolve markedly: the trion peak increases whereas the exciton peak becomes relatively weaker, indicating that photo-doping and enhanced free-carrier density at higher excitation levels promote exciton-to-trion conversion. This behavior suggests that the power-dependent PL on quartz mainly reflects a redistribution of carrier populations [168].

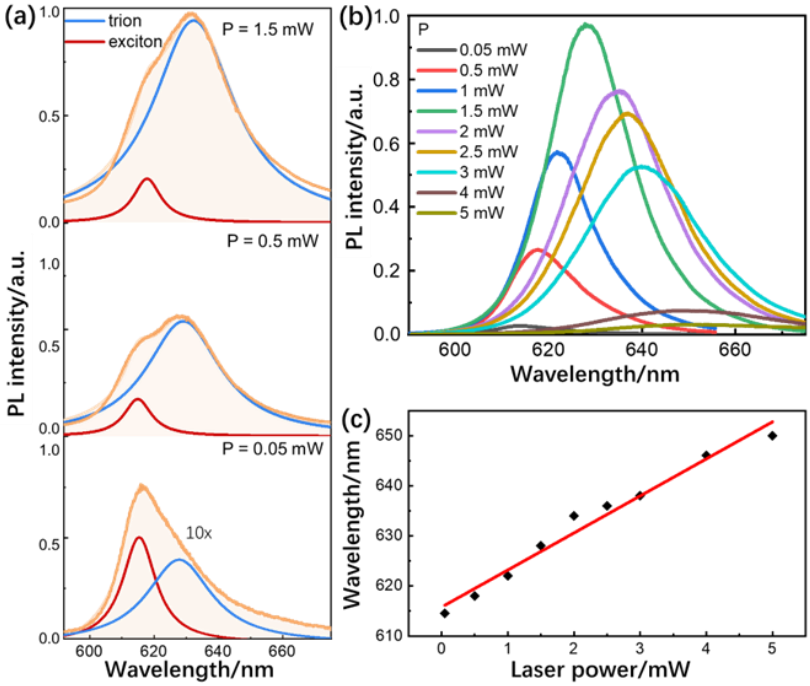

Figure 4.25. PL spectra measured for WS_2 monolayer on (a) quartz film and (b) metasurface at different excitation laser powers, (c) peak positions extracted from (b) as a function of laser power.

In contrast, WS_2 integrated with the metasurface exhibits a distinctly different power-dependent PL response, as shown in Fig. 4.25(b), with the excitation power varied from 0.05 mW to 5 mW. The PL peak position undergoes a pronounced redshift with increasing excitation power, and the shift follows an approximately linear dependence with a slope of ≈7.3 nm/mW, as

summarized in Fig. 4.25(c). This behavior can be attributed to the combined effects of band-gap renormalization (BGR) induced by high photo-generated carrier densities [171] and a power-dependent evolution of the light–matter hybridization. At low excitation powers, the Mie resonance predominantly couples to the neutral exciton, whereas at higher carrier densities it progressively couples more strongly to the trion state [168]. The strong near-field enhancement provided by the metasurface leads to locally higher absorption and carrier density for the same incident power, thereby amplifying both the BGR effect and the relative trion population. As a result, the emission gradually shifts toward a trion-dominated polaritonic branch, corresponding to an effective transition from exciton–Mie to trion–Mie coupling. Possible thermal effects were carefully examined and excluded as the dominant mechanism: after high-power illumination, the PL peak position rapidly recovers upon returning to low excitation power, indicating that the observed redshift is not governed by heating.

Meanwhile, the integrated PL intensity on the metasurface first increases with excitation power and then decreases at higher powers, exhibiting a clear saturation behavior. The maximum PL enhancement occurs at 628 nm, where trion emission dominates. Compared with the low-power spectrum at 0.05 mW (peak at 614 nm), the PL intensity at 1.5 mW is enhanced by approximately 37 times on the metasurface, whereas WS_2 on quartz shows only about a 12-fold enhancement under similar conditions. This pronounced enhancement therefore indicates that, in addition to exciton–Mie coupling, a strong trion–Mie coupling channel is activated at elevated excitation powers. Notably, the PL lineshape on the metasurface exhibits only a weak asymmetry rather than two well-resolved peaks of comparable intensity, implying that exciton–Mie and trion–Mie couplings do not dominate simultaneously. Instead, the system evolves from an exciton-dominated regime at low power to a trion-dominated regime at higher power. Future time-resolved spectroscopy is expected to provide deeper insight into the ultrafast carrier dynamics and the dynamic transition between exciton–Mie and trion–Mie coupling in this hybrid system.

4.6 Extension for applications

During the transfer of monolayer WS_2 onto a nanostructured substrate, it is generally difficult to achieve a perfectly flat and strain-free configuration due to the presence of surface topography and unavoidable mechanical deformation. Such local bending or wrinkling may introduce variations in the effective incident angle of the excitation light at different regions of the monolayer. To evaluate whether these transfer-induced angular deviations could affect the absorption enhancement, we performed angle-resolved absorption simulations.

The incident angle θ is defined as the angle between the incident wave vector and the surface normal of the metasurface. By varying θ, we simulated the absorption spectra of the WS_2-integrated Huygens metasurface and obtained angle-dependent absorption mappings for both the total system absorption and the intrinsic WS_2 absorption component as shown in Fig. 4.26. The simulation results show that the absorption peak positions remain nearly unchanged as the incident angle increases. Even at a relatively large incident angle of 30°, the intrinsic WS_2 absorption remains higher than 0.60.

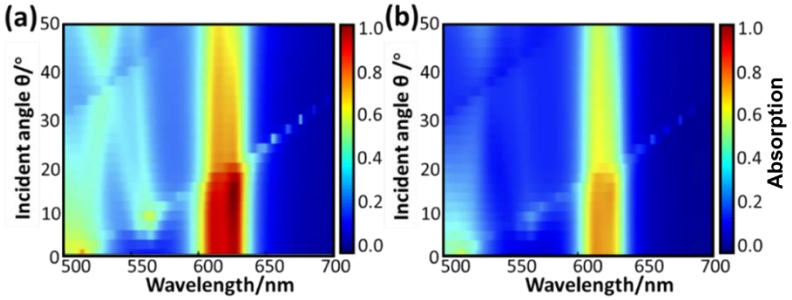

Figure 4.26. Angle-resolved absorption mapping of monolayer WS_2 integrated on the Si Huygens metasurface: (a) total optical absorption of the hybrid system; (b) intrinsic absorption contribution from the WS_2 monolayer under varying incident angles θ.

These results demonstrate that the absorption enhancement provided by the Huygens metasurface is robust against variations in the angle of incidence. Therefore, moderate local bending or angular deviations of the transferred WS_2 monolayer do not significantly degrade the optical enhancement effect. This angular stability further confirms the practical reliability of our metasurface platform for realistic device configurations where perfect planar transfer is difficult to achieve.

To verify the generality of the proposed absorption-enhancement strategy for 2D TMDC materials, we further extended the realization of DCC states to other representative TMDCs in the visible spectral range. This confirms that the designed metasurface can serve as a versatile platform for enhancing light–matter interaction in a broad class of 2D semiconductors.

As representative examples, we aligned the excitonic absorption peak wavelengths of several typical TMDC monolayers. Figures 4.27(a)–(c) show the simulated absorption spectra of MoS_2, WSe_2, and $MoSe_2$ placed on Si substrates, with their main excitonic peaks located at 644.33 nm, 741.84 nm, and 771.56 nm, respectively. Since the excitonic resonance of MoS_2 lies at a shorter wavelength than that of WS_2, spectral matching with the Si -based Mie resonance can be readily achieved, making the attainment of the DCC state comparatively straightforward.

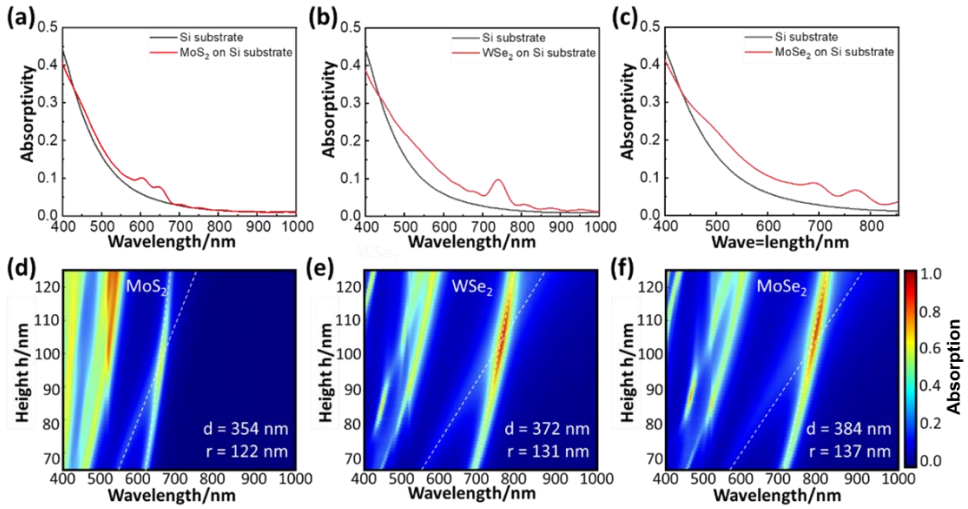

Figure 4.27. (a)–(c) Absorption spectra of bare Si substrates covered with different monolayer TMDCs, MoS_2, WSe_2, and $MoSe_2$, respectively. (d)–(f) Height-dependent absorption spectral maps of the corresponding Si metasurfaces. The spectral overlap between the ED and MD resonances is engineered to coincide with the excitonic absorption peaks of each TMDC materials.

In contrast, for TMDC materials operating in the longer-wavelength region such as WSe_2 and $MoSe_2$, it becomes increasingly difficult to realize mode matching using c-Si due to its reduced confinement capability and dispersion limitations at near-infrared wavelengths. To keep the fabrication process simple and avoid redesigning the metasurface geometry, we employed a-Si, which possesses a higher intrinsic optical loss than c-Si, as the resonator material. This effectively red-shifts and broadens the Mie resonance, enabling DCC-state formation at the desired wavelengths.

The corresponding absorption spectral mappings as a function of the Mie cylinder height *h* are presented in Figs. S4.27(d)–(f), clearly demonstrating successful coupling and absorption enhancement for MoS_2, WSe_2, and $MoSe_2$. These results further highlight the adaptability of the proposed metasurface platform across a wide wavelength range and various 2D TMDC materials.

Conclusion

2D TMDCs constitute a unique class of atomically thin semiconductors that combine tunable band structures, strong excitonic effects, and rich light–matter interaction physics. In the monolayer limit, their direct bandgaps and large exciton binding energies enable efficient exciton–photon coupling, making them promising candidates for next-generation optoelectronic and photonic devices operating in the visible spectrum. However, the atomic-scale thickness of monolayer TMDCs imposes an intrinsic limitation on their optical absorption, which typically remains far below the level required for high-performance applications. Overcoming this fundamental bottleneck is therefore a central challenge in the development of practical TMDC-based optoelectronic systems.

In this dissertation, we address this challenge by integrating monolayer TMDCs with carefully designed all-dielectric metasurfaces to enhance light–matter interactions in a low-loss, scalable, and spectrally versatile manner. Compared with plasmonic platforms, dielectric metasurfaces provide strong optical confinement without introducing significant Ohmic losses, while offering high flexibility in tailoring resonant modes through geometry. Building on these advantages, this work systematically explores the coupling between excitonic transitions in TMDCs and Mie resonances supported by Si metasurfaces.

First, we established the physical framework of Mie resonances and DCC in dielectric metasurfaces, and extended their operational regime into the violet light range. By engineering ED and MD resonances in Si Huygens metasurfaces, we demonstrated that spectrally degenerate ED and MD modes can be achieved through precise geometrical design, enabling DCC conditions and near-unity absorption. This extension to the violet spectral region is particularly important, as it expands the applicability of dielectric metasurface platforms beyond the conventional visible and near-infrared ranges.

Using WS_2 as a representative TMDCs, we numerically demonstrated that coherent coupling between excitons and the ED Mie resonance leads to the formation of hybrid Miexciton states, manifested by a clear anticrossing behavior and a Rabi splitting. When the ED and MD modes are spectrally overlapped under the DCC condition, the coherent interaction strength is further enhanced, increasing the Rabi splitting to about 57 meV and significantly boosting absorption. Under optimized geometrical parameters, the absorption of the WS_2 monolayer reaches approximately 0.70, with a total absorption approaching 0.90 in simulations. Importantly, this DCC-assisted enhancement strategy was shown to be extendable to other TMDCs in the visible

spectrum, including WSe_2, MoS_2, and $MoSe_2$, establishing a universal absorption-enhancement platform for 2D materials.

Beyond numerical investigations, we experimentally realized the integration of monolayer WS_2 with a Si Huygens metasurface and validated the predicted enhancement mechanisms. The fabricated structures exhibit intermediate coupling, giving rise to experimentally observable Miexciton signatures and a measured absorption exceeding 0.84, in good agreement with simulations. Under optimized conditions, the ED and MD modes overlap in experiment, fulfilling the DCC principle and further reinforcing the coherent coupling. This enhanced light–matter interaction not only boosts absorption but also leads to an average PL enhancement of approximately 18 times, attributed to strong near-field excitation and an increased LDOS. Furthermore, PB measurements reveal signatures of coupling between Mie resonances and trion states at higher excitation densities, suggesting the emergence of trion–Mie hybrid modes in carrier-rich regimes.

Overall, this dissertation establishes an all-dielectric Huygens metasurface as a robust and versatile platform for enhancing excitonic responses in monolayer TMDCs. By combining intermediate coupling with DCC, strong absorption and emission enhancement are achieved. The demonstrated platform offers a low-loss, scalable, and material-universal strategy for tailoring light–matter interactions in atomically thin semiconductors, opening new opportunities for applications in photodetection, light emission, optical sensing, and imaging. Future work will focus on further optimizing fabrication accuracy, exploring dynamic tunability, and extending these concepts toward integrated and actively controlled TMDC-based photonic devices.

Appendix

Commercial WS_2 Monolayer Films

For the experiments in this thesis, commercially obtained high-quality 2D WS_2 monolayer films were used. The monolayer films were purchased from Ossila Ltd., a vendor specializing in two-dimensional materials and TMDCs.

The specific product used is a high-purity WS_2 monolayer film (CAS No. 12138-09-9) grown on a sapphire substrate. According to the supplier's catalogue, the film has a confirmed chemical composition of WS_2 with >99% purity, and exhibits optical transparency >97% with coverage exceeding 95%. The nominal size of the purchased samples is 1 cm × 1 cm.

Growth of the monolayer material is accomplished via CVD directly on the sapphire substrate. The catalogue indicates that the monolayer is transparent, continuous, and directly grown on the substrate, allowing for both characterization and direct device fabrication or subsequent transfer to other substrates if needed. The monolayer thickness is consistent with WS_2 atomic layer dimensions (~0.7–1 nm) reported in literature, and the product is suitable for optical, electrical, and spectroscopic studies (e.g., Raman, PL).

The WS_2 monolayer films from Ossila are widely used as standard 2D material references in research due to their reproducible quality and availability, providing a reliable baseline for studies involving 2D semiconductors when synthesis capabilities are not available locally.

Abbreviations

2D – Two-dimensional

TMDCs – transition metal dichalcogenides

DCC – degenerate critical coupling

PL – photoluminescence

ED – electric dipole

MD – magnetic dipole

TED – transverse electric dipole

EQ – electric quadrupole

MQ –magnetic quadrupole

Si – silicon

c-Si – crystalline silicon

a-Si – amorphous silicon

h-BN – hexagonal boron nitride

WS_2 – tungsten disulfide

PDMS – polydimethylsiloxane

PPC – poly (propylene) carbonate

PS – polystyrene

FWHM – full width at half maximum

EBL – electron-beam lithography

PVD – physical vapor deposition

CVD – chemical vapor deposition

PB – power-monitor-based

FDP – frequency-domain power

CMOS – Complementary Metal–Oxide–Semiconductor

FDTD – finite-difference time-domain

PMLs – Perfectly matched layers

LPB –lower polariton branches

UPB – upper polariton branches

plexciton – plasmon–exciton

BGR – band-gap renormalization

UPM – upper polariton mode

LDOS – local density of optical states

References

1. K. Ozawa, H. Sugimoto, D. Shima, T. Hinamoto, M. Karimi Habil, Y. J. Lee, S. Raza, K. Imaeda, K. Ueno, M. L. Brongersma, and M. Fujii, "Routing Light Emission from Monolayer MoS2 by Mie Resonances of Crystalline Silicon Nanospheres," ACS Appl. Opt. Mater. **3**, 375–382 (2025).

2. E. Maggiolini, L. Polimeno, F. Todisco, A. Di Renzo, B. Han, M. De Giorgi, V. Ardizzone, C. Schneider, R. Mastria, A. Cannavale, M. Pugliese, L. De Marco, A. Rizzo, V. Maiorano, G. Gigli, D. Gerace, D. Sanvitto, and D. Ballarini, "Strongly enhanced light–matter coupling of monolayer WS_2 from a bound state in the continuum," Nat. Mater. **22**, 964–969 (2023).

3. K. F. Mak, C. Lee, J. Hone, J. Shan, and T. F. Heinz, "Atomically Thin MoS_2: A New Direct-Gap Semiconductor," Phys. Rev. Lett. **105**, 136805 (2010).

4. J. SUN, H. Hu, D. Zheng, D. Zhang, Q. Deng, S. Zhang, and H. Xu, "Light-Emitting Plexciton: Exploiting Plasmon–Exciton Interaction in the Intermediate Coupling Regime," ACS Nano **12**, 10393–10402 (2018).

5. K. F. Mak and J. Shan, "Photonics and optoelectronics of 2D semiconductor transition metal dichalcogenides," Nat. Photonics **10**, 216–226 (2016).

6. F. Xia, H. Wang, D. Xiao, M. Dubey, and A. Ramasubramaniam, "Two-dimensional material nanophotonics," Nat. Photonics **8**, 899–907 (2014).

7. T. Mueller and E. Malic, "Exciton physics and device application of two-dimensional transition metal dichalcogenide semiconductors," NPJ 2D Mater. Appl. **2**, 29 (2018).

8. D. Kufer and G. Konstantatos, "Highly Sensitive, Encapsulated MoS_2 Photodetector with Gate Controllable Gain and Speed," Nano Lett. **15**, 7307–7313 (2015).

9. I. Epstein, B. Terrés, A. J. Chaves, V.-V. Pusapati, D. A. Rhodes, B. Frank, V. Zimmermann, Y. Qin, K. Watanabe, T. Taniguchi, H. Giessen, S. Tongay, J. C. Hone, N. M. R. Peres, and F. H. L. Koppens, "Near-Unity Light Absorption in a Monolayer WS_2 Van der Waals Heterostructure Cavity," Nano Lett. **20**, 3545–3552 (2020).

10. Y. Tian, Z. Guo, Z. Liu, H. Lin, X. Li, J. Chen, S. Deng, and F. Liu, "Efficiently enhanced the visible-light absorption of monolayer WS_2 by constructing an asymmetric Fabry-Perot cavity," Mater. Today Nano **14**, 100112 (2021).

11. N. Ansari, E. Mohebbi, and F. Gholami, "Enhancement of light absorption in a WS_2 monolayer using spacer and Au layers," J. Appl. Phys. **127**, 063101 (2020).

12. M. Iwanaga, X. Yang, V. Karanikolas, T. Kuroda, and Y. Sakuma, "Prominently enhanced luminescence from a continuous monolayer of transition metal dichalcogenide on all-dielectric metasurfaces," Nanophotonics **13**, 95–105 (2024).

13. H. Li, G. Wei, H. Zhou, H. Xiao, M. Qin, S. Xia, and F. Wu, "Polarization-independent near-infrared superabsorption in transition metal dichalcogenide Huygens metasurfaces by degenerate critical coupling," Phys. Rev. B **105**, 165305 (2022).

14. S. Lepeshov, M. Wang, A. Krasnok, O. Kotov, T. Zhang, H. Liu, T. Jiang, B. Korgel, M. Terrones, Y. Zheng, and A. Alú, "Tunable Resonance Coupling in Single Si Nanoparticle–Monolayer WS_2 Structures," ACS Appl. Mater. Interfaces **10**, 16690–16697 (2018).

15. N. Bernhardt, K. Koshelev, S. J. U. White, K. W. C. Meng, J. E. Fröch, S. Kim, T. T. Tran, D.-Y. Choi, Y. Kivshar, and A. S. Solntsev, "Quasi-BIC Resonant Enhancement of Second-Harmonic Generation in WS_2 Monolayers," Nano Lett. **20**, 5309–5314 (2020).

16. L. Huang, A. Krasnok, A. Alú, Y. Yu, D. Neshev, and A. E. Miroshnichenko, "Enhanced light–matter interaction in two-dimensional transition metal dichalcogenides," Rep. Prog. Phys. **85**, 046401 (2022).

17. X. Wang, J. Wang, Z.-D. Hu, T. Sang, and Y. Feng, "Perfect absorption of modified-molybdenum-disulfide-based Tamm plasmonic structures," Appl. Phys. Express **11**, 062601 (2018).

18. H. Lu, X. Gan, D. Mao, Y. Fan, D. Yang, and J. Zhao, "Nearly perfect absorption of light in monolayer molybdenum disulfide supported by multilayer structures," Opt. Express **25**, 21630–21636 (2017).

19. Y. Long, H. Deng, H. Xu, L. Shen, W. Guo, C. Liu, W. Huang, W. Peng, L. Li, H. Lin, and C. Guo, "Magnetic coupling metasurface for achieving broad-band and broad-angular absorption in the MoS_2 monolayer," Opt. Mater. Express **7**, 100–110 (2017).

20. S. Lepeshov, A. Krasnok, and A. Alù, "Enhanced excitation and emission from 2D transition metal dichalcogenides with all-dielectric nanoantennas," Nanotechnology **30**, 254004 (2019).

21. C. Ma, X. Li, P. Huang, X. Liu, J. Yan, Z. Zheng, J. Yao, C. Du, Y. Liu, X. Li, B. Guan, and K. Chen, "Enhanced Optical Absorption and Emission from Monolayer WS_2 Integrated onto a TiO_2 Nanohole Array," Adv. Opt. Mater. **13**, 2402015 (2025).

22. Q. Li, J. Lu, P. Gupta, and M. Qiu, "Engineering Optical Absorption in Graphene and Other 2D Materials: Advances and Applications," Adv. Opt. Mater. **7**, 1900595 (2019).

23. K. Imaeda, J. Yue, H. Takeuchi, and K. Ueno, "Plasmon Dephasing and Near-Field Enhancement of Periodical Arrays of Au Nanogap Dimers," J. Phys. Chem. C **128**, 5659–5666 (2024).

24. Z. Lu, J. Ji, H. Ye, H. Zhang, S. Zhang, and H. Xu, "Quantifying the ultimate limit of plasmonic near-field enhancement," Nat. Commun. **15**, 8803 (2024).

25. L. Huang, A. Krasnok, A. Alú, Y. Yu, D. Neshev, and A. E. Miroshnichenko, "Enhanced light–matter interaction in two-dimensional transition metal dichalcogenides," Rep. Prog. Phys. **85**, 046401 (2022).

26. J. Zhou, P. A. D. Gonçalves, F. Riminucci, S. Dhuey, E. S. Barnard, A. Schwartzberg, F. J. García de Abajo, and A. Weber-Bargioni, "Probing plexciton emission from 2D materials on gold nanotrenches," Nat. Commun. **15**, 9583 (2024).

27. L. Greten, R. Salzwedel, T. Göde, D. Greten, S. Reich, S. Hughes, M. Selig, and A. Knorr, "Strong Coupling of Two-Dimensional Excitons and Plasmonic Photonic Crystals: Microscopic Theory Reveals Triplet Spectra," ACS Photonics **11**, 1396–1411 (2024).

28. H. Shinomiya, H. Sugimoto, T. Hinamoto, Y. J. Lee, M. L. Brongersma, and M. Fujii, "Enhanced Light Emission from Monolayer MoS_2 by Doubly Resonant Spherical Si Nanoantennas," ACS Photonics **9**, 1741–1747 (2022).

29. S. You, Y. Zhang, M. Fan, S. Luo, and C. Zhou, "Strong light–matter interactions of exciton in bulk WS_2 and a toroidal dipole resonance," Opt. Lett. **48**, 1530–1533 (2023).

30. C. Gao, S. You, Y. Zhang, L. Wang, H. Duan, H. He, Q. Xie, and C. Zhou, "Strong coupling between excitons and quasi-bound states in the continuum mode with stable resonance wavelength in the near-infrared region," Appl. Phys. Lett. **124**, 051701 (2024).

31. T. Weber, L. Kühner, L. Sortino, A. Ben Mhenni, N. P. Wilson, J. Kühne, J. J. Finley, S. A. Maier, and A. Tittl, "Intrinsic strong light-matter coupling with self-hybridized bound states in the continuum in van der Waals metasurfaces," Nat. Mater. **22**, 970–976 (2023).

32. I. A. M. Al-Ani, K. As'Ham, L. Huang, A. E. Miroshnichenko, and H. T. Hattori, "Enhanced Strong Coupling of TMDC Monolayers by Bound State in the Continuum," Laser Photon. Rev. **15**, 2100240 (2021).

33. K. S. Novoselov, A. K. Geim, S. V Morozov, D. Jiang, Y. Zhang, S. V Dubonos, I. V Grigorieva, and A. A. Firsov, "Electric Field Effect in Atomically Thin Carbon Films," Science (1979) **306**, 666–669 (2004).

34. C. Tan, X. Cao, X.-J. Wu, Q. He, J. Yang, X. Zhang, J. Chen, W. Zhao, S. Han, G.-H. Nam, M. Sindoro, and H. Zhang, "Recent Advances in Ultrathin Two-Dimensional Nanomaterials," Chem. Rev. **117**, 6225–6331 (2017).

35. D. Deng, K. S. Novoselov, Q. Fu, N. Zheng, Z. Tian, and X. Bao, "Catalysis with two-dimensional materials and their heterostructures," Nat. Nanotechnol. **11**, 218–230 (2016).

36. S. Pang, Y. Hernandez, X. Feng, and K. Müllen, "Graphene as Transparent Electrode Material for Organic Electronics," Adv. Mater. **23**, 2779–2795 (2011).

37. K. S. Novoselov, A. Mishchenko, A. Carvalho, and A. H. Castro Neto, "2D materials and van der Waals heterostructures," Science (1979) **353**, aac9439 (2016).

38. Y. Gong, J. Lin, X. Wang, G. Shi, S. Lei, Z. Lin, X. Zou, G. Ye, R. Vajtai, B. I. Yakobson, H. Terrones, M. Terrones, B. K. Tay, J. Lou, S. T. Pantelides, Z. Liu, W. Zhou, and P. M. Ajayan, "Vertical and in-plane heterostructures from WS_2/MoS_2 monolayers," Nat. Mater. **13**, 1135–1142 (2014).

39. T. Georgiou, R. Jalil, B. D. Belle, L. Britnell, R. V Gorbachev, S. V Morozov, Y.-J. Kim, A. Gholinia, S. J. Haigh, O. Makarovsky, L. Eaves, L. A. Ponomarenko, A. K. Geim, K. S. Novoselov, and A. Mishchenko, "Vertical field-effect transistor based on graphene–WS_2

heterostructures for flexible and transparent electronics," Nat. Nanotechnol. **8**, 100–103 (2013).

40. A. Molina-Sánchez, K. Hummer, and L. Wirtz, "Vibrational and optical properties of MoS_2: From monolayer to bulk," Surf. Sci. Rep. **70**, 554–586 (2015).

41. L. Yang, K. Majumdar, H. Liu, Y. Du, H. Wu, M. Hatzistergos, P. Y. Hung, R. Tieckelmann, W. Tsai, C. Hobbs, and P. D. Ye, "Chloride Molecular Doping Technique on 2D Materials: $WS2_2$ and MoS_2," Nano Lett. **14**, 6275–6280 (2014).

42. G. A. Tritsaris, B. D. Malone, and E. Kaxiras, "Optoelectronic properties of single-layer, double-layer, and bulk tin sulfide: A theoretical study," J. Appl. Phys. **113**, 233507 (2013).

43. Y. Ma, Y. Dai, M. Guo, L. Yu, and B. Huang, "Tunable electronic and dielectric behavior of GaS and GaSe monolayers," Phys. Chem. Chem. Phys. **15**, 7098–7105 (2013).

44. D. G. Papageorgiou, I. A. Kinloch, and R. J. Young, "Mechanical properties of graphene and graphene-based nanocomposites," Prog. Mater. Sci. **90**, 75–127 (2017).

45. J. V Vaghasiya, C. C. Mayorga-Martinez, and M. Pumera, "Wearable sensors for telehealth based on emerging materials and nanoarchitectonics," npj Flex. Electron. **7**, 26 (2023).

46. D. Akinwande, C. J. Brennan, J. S. Bunch, P. Egberts, J. R. Felts, H. Gao, R. Huang, J.-S. Kim, T. Li, Y. Li, K. M. Liechti, N. Lu, H. S. Park, E. J. Reed, P. Wang, B. I. Yakobson, T. Zhang, Y.-W. Zhang, Y. Zhou, and Y. Zhu, "A review on mechanics and mechanical properties of 2D materials—Graphene and beyond," Extreme. Mech. Lett. **13**, 42–77 (2017).

47. L. A. Walsh and C. L. Hinkle, "van der Waals epitaxy: 2D materials and topological insulators," Appl. Mater. Today **9**, 504–515 (2017).

48. D. M. Guzman, H. M. Alyahyaei, and R. A. Jishi, "Superconductivity in graphene-lithium," 2d Mater. **1**, 021005 (2014).

49. M. Chhowalla, H. S. Shin, G. Eda, L.-J. Li, K. P. Loh, and H. Zhang, "The chemistry of two-dimensional layered transition metal dichalcogenide nanosheets," Nat. Chem. **5**, 263–275 (2013).

50. K. S. Novoselov, D. Jiang, F. Schedin, T. J. Booth, V. V Khotkevich, S. V Morozov, and A. K. Geim, "Two-dimensional atomic crystals," Proc. Natl. Acad. Sci. **102**, 10451–10453 (2005).

51. Q. H. Wang, K. Kalantar-Zadeh, A. Kis, J. N. Coleman, and M. S. Strano, "Electronics and optoelectronics of two-dimensional transition metal dichalcogenides," Nat. Nanotechnol. **7**, 699–712 (2012).

52. W. S. Yun, S. W. Han, S. C. Hong, I. G. Kim, and J. D. Lee, "Thickness and strain effects on electronic structures of transition metal dichalcogenides: 2H-MX_2 semiconductors (M = Mo, W; X = S, Se, Te), " Phys. Rev. B **85**, 33305 (2012).

53. H. Li, X. Wu, H. Liu, B. Zheng, Q. Zhang, X. Zhu, Z. Wei, X. Zhuang, H. Zhou, W. Tang, X. Duan, and A. Pan, "Composition-Modulated Two-Dimensional Semiconductor Lateral Heterostructures via Layer-Selected Atomic Substitution," ACS Nano **11**, 961–967 (2017).

54. X. Duan, C. Wang, J. C. Shaw, R. Cheng, Y. Chen, H. Li, X. Wu, Y. Tang, Q. Zhang, A. Pan, J. Jiang, R. Yu, Y. Huang, and X. Duan, "Lateral epitaxial growth of two-dimensional layered semiconductor heterojunctions," Nat. Nanotechnol. **9**, 1024–1030 (2014).

55. X. Duan, C. Wang, Z. Fan, G. Hao, L. Kou, U. Halim, H. Li, X. Wu, Y. Wang, J. Jiang, A. Pan, Y. Huang, R. Yu, and X. Duan, "Synthesis of WS_2xSe_{2-2x} Alloy Nanosheets with Composition-Tunable Electronic Properties," Nano Lett. **16**, 264–269 (2016).

56. Y. D. Kim, H. Kim, Y. Cho, J. H. Ryoo, C.-H. Park, P. Kim, Y. S. Kim, S. Lee, Y. Li, S.-N. Park, Y. Shim Yoo, D. Yoon, V. E. Dorgan, E. Pop, T. F. Heinz, J. Hone, S.-H. Chun, H. Cheong, S. W. Lee, M.-H. Bae, and Y. D. Park, "Bright visible light emission from graphene," Nat. Nanotechnol. **10**, 676–681 (2015).

57. H. Zhou, S. Yuan, X. Wang, T. Xu, X. Wang, H. Li, W. Zheng, P. Fan, Y. Li, L. Sun, and A. Pan, "Vapor Growth and Tunable Lasing of Band Gap Engineered Cesium Lead Halide Perovskite Micro/Nanorods with Triangular Cross Section," ACS Nano **11**, 1189–1195 (2017).

58. H. Ago, H. Endo, P. Solís-Fernández, R. Takizawa, Y. Ohta, Y. Fujita, K. Yamamoto, and M. Tsuji, "Controlled van der Waals Epitaxy of Monolayer MoS_2 Triangular Domains on Graphene," ACS Appl. Mater. Interfaces **7**, 5265–5273 (2015).

59. Y. Tison, J. Lagoute, V. Repain, C. Chacon, Y. Girard, F. Joucken, R. Sporken, F. Gargiulo, O. V Yazyev, and S. Rousset, "Grain Boundaries in Graphene on SiC(000$\bar{1}$) Substrate," Nano Lett. **14**, 6382–6386 (2014).

60. Y. Shi, W. Zhou, A.-Y. Lu, W. Fang, Y.-H. Lee, A. L. Hsu, S. M. Kim, K. K. Kim, H. Y. Yang, L.-J. Li, J.-C. Idrobo, and J. Kong, "van der Waals Epitaxy of MoS_2 Layers Using Graphene as Growth Templates," Nano Lett. **12**, 2784–2791 (2012).

61. K. Kim, S. Coh, L. Z. Tan, W. Regan, J. M. Yuk, E. Chatterjee, M. F. Crommie, M. L. Cohen, S. G. Louie, and A. Zettl, "Raman Spectroscopy Study of Rotated Double-Layer Graphene: Misorientation-Angle Dependence of Electronic Structure," Phys. Rev. Lett. **108**, 246103 (2012).

62. N. G. Kalugin, L. Jing, E. S. Morell, G. C. Dyer, L. Wickey, M. Ovezmyradov, A. D. Grine, M. C. Wanke, E. A. Shaner, C. N. Lau, L. E. F. Foa Torres, M. V Fistul, and K. B. Efetov, "Photoelectric polarization-sensitive broadband photoresponse from interface junction states in graphene," 2d Mater. **4**, 015002 (2017).

63. J. Wang, P. Liu, B. Xia, H. Wei, Y. Wei, Y. Wu, K. Liu, L. Zhang, J. Wang, Q. Li, S. Fan, and K. Jiang, "Observation of Charge Generation and Transfer during CVD Growth of Carbon Nanotubes," Nano Lett. **16**, 4102–4109 (2016).

64. J. D. Cain, F. Shi, J. Wu, and V. P. Dravid, "Growth Mechanism of Transition Metal Dichalcogenide Monolayers: The Role of Self-Seeding Fullerene Nuclei," ACS Nano **10**, 5440–5445 (2016).

65. J. Mann, Q. Ma, P. M. Odenthal, M. Isarraraz, D. Le, E. Preciado, D. Barroso, K. Yamaguchi, G. von Son Palacio, A. Nguyen, T. Tran, M. Wurch, A. Nguyen, V. Klee, S. Bobek, D. Sun, Tony. F. Heinz, T. S. Rahman, R. Kawakami, and L. Bartels, "2-Dimensional Transition Metal Dichalcogenides with Tunable Direct Band Gaps: $MoS_{2(1-x)}Se_{2x}$ Monolayers," Adv. Mater. **26**, 1399–1404 (2014).

66. P. D. Cunningham, K. M. McCreary, A. T. Hanbicki, M. Currie, B. T. Jonker, and L. M. Hayden, "Charge Trapping and Exciton Dynamics in Large-Area CVD Grown MoS_2," J. Phys. Chem. C **120**, 5819–5826 (2016).

67. A. Govind Rajan, J. H. Warner, D. Blankschtein, and M. S. Strano, "Generalized Mechanistic Model for the Chemical Vapor Deposition of 2D Transition Metal Dichalcogenide Monolayers," ACS Nano **10**, 4330–4344 (2016).

68. J. N. Coleman, M. Lotya, A. O'Neill, S. D. Bergin, P. J. King, U. Khan, K. Young, A. Gaucher, S. De, R. J. Smith, I. V Shvets, S. K. Arora, G. Stanton, H.-Y. Kim, K. Lee, G. T. Kim, G. S. Duesberg, T. Hallam, J. J. Boland, J. J. Wang, J. F. Donegan, J. C. Grunlan, G. Moriarty, A. Shmeliov, R. J. Nicholls, J. M. Perkins, E. M. Grieveson, K. Theuwissen, D. W. McComb, P. D. Nellist, and V. Nicolosi, "Two-Dimensional Nanosheets Produced by Liquid Exfoliation of Layered Materials," Science (1979) **331**, 568–571 (2011).

69. G. Wang, A. Chernikov, M. M. Glazov, T. F. Heinz, X. Marie, T. Amand, and B. Urbaszek, "Colloquium: Excitons in atomically thin transition metal dichalcogenides," Rev. Mod. Phys. **90**, 21001 (2018).

70. G. H. Wannier, "The Structure of Electronic Excitation Levels in Insulating Crystals," Phys. Rev. **52**, 191–197 (1937).

71. J. Frenkel, "On the Transformation of Light into Heat in Solids. II," Phys. Rev. **37**, 1276–1294 (1931).

72. M. Koperski, M. R. Molas, A. Arora, K. Nogajewski, A. O. Slobodeniuk, C. Faugeras, and M. Potemski, "Optical properties of atomically thin transition metal dichalcogenides: observations and puzzles," Nanophotonics **6**, 1289–1308 (2017).

73. K. F. Mak, C. Lee, J. Hone, J. Shan, and T. F. Heinz, "Atomically Thin MoS_2: A New Direct-Gap Semiconductor," Phys. Rev. Lett. **105**, 136805 (2010).

74. G. Danan, B. Etienne, F. Mollot, R. Planel, A. M. Jean-Louis, F. Alexandre, B. Jusserand, G. Le Roux, J. Y. Marzin, H. Savary, and B. Sermage, "Optical evidence of the direct-to-indirect-gap transition in GaAs-AlAs short-period superlattices," Phys. Rev. B **35**, 6207–6212 (1987).

75. D. Xiao, W. Yao, and Q. Niu, "Valley-Contrasting Physics in Graphene: Magnetic Moment and Topological Transport," Phys. Rev. Lett. **99**, 236809 (2007).

76. W. Yao, D. Xiao, and Q. Niu, "Valley-dependent optoelectronics from inversion symmetry breaking," Phys. Rev. B **77**, 235406 (2008).

77. D. Xiao, G.-B. Liu, W. Feng, X. Xu, and W. Yao, "Coupled Spin and Valley Physics in Monolayers of MoS_2 and Other Group-VI Dichalcogenides," Phys. Rev. Lett. **108**, 196802 (2012).

78. Z. Ye, T. Cao, K. O'Brien, H. Zhu, X. Yin, Y. Wang, S. G. Louie, and X. Zhang, "Probing excitonic dark states in single-layer tungsten disulphide," Nature **513**, 214–218 (2014).

79. K. He, N. Kumar, L. Zhao, Z. Wang, K. F. Mak, H. Zhao, and J. Shan, "Tightly Bound Excitons in Monolayer WSe_2," Phys. Rev. Lett. **113**, 26803 (2014).

80. G.-H. Jung, S. Yoo, and Q.-H. Park, "Measuring the optical permittivity of two-dimensional materials without a priori knowledge of electronic transitions," Nanophotonics **8**, 263–270 (2019).

81. D. E. Aspnes and A. A. Studna, "Dielectric functions and optical parameters of Si, Ge, GaP, GaAs, GaSb, InP, InAs, and InSb from 1.5 to 6.0 eV," Phys. Rev. B **27**, 985–1009 (1983).

82. S. Butun, E. Palacios, J. D. Cain, Z. Liu, V. P. Dravid, and K. Aydin, "Quantifying Plasmon-Enhanced Light Absorption in Monolayer WS2 Films," ACS Appl. Mater. Interfaces **9**, 15044–15051 (2017).

83. Z. Chen, B. Guo, Y. Yang, and C. Cheng, "Metamaterials-based enhanced energy harvesting: A review," Physica. B Condens. Matter. **438**, 1–8 (2014).

84. N. Meinzer, W. L. Barnes, and I. R. Hooper, "Plasmonic meta-atoms and metasurfaces," Nat. Photonics **8**, 889–898 (2014).

85. S. Wang, P. C. Wu, V.-C. Su, Y.-C. Lai, C. Hung Chu, J.-W. Chen, S.-H. Lu, J. Chen, B. Xu, C.-H. Kuan, T. Li, S. Zhu, and D. P. Tsai, "Broadband achromatic optical metasurface devices," Nat. Commun. **8**, 187 (2017).

86. N. Yu, P. Genevet, M. A. Kats, F. Aieta, J.-P. Tetienne, F. Capasso, and Z. Gaburro, "Light Propagation with Phase Discontinuities: Generalized Laws of Reflection and Refraction," Science (1979) **334**, 333–337 (2011).

87. R. Paniagua-Domínguez, Y. F. Yu, E. Khaidarov, S. Choi, V. Leong, R. M. Bakker, X. Liang, Y. H. Fu, V. Valuckas, L. A. Krivitsky, and A. I. Kuznetsov, "A Metalens with a Near-Unity Numerical Aperture," Nano Lett. **18**, 2124–2132 (2018).

88. S. Wang, P. C. Wu, V.-C. Su, Y.-C. Lai, M.-K. Chen, H. Y. Kuo, B. H. Chen, Y. H. Chen, T.-T. Huang, J.-H. Wang, R.-M. Lin, C.-H. Kuan, T. Li, Z. Wang, S. Zhu, and D. P. Tsai, "A broadband achromatic metalens in the visible," Nat. Nanotechnol. **13**, 227–232 (2018).

89. D. Lin, A. L. Holsteen, E. Maguid, P. Fan, P. G. Kik, E. Hasman, and M. L. Brongersma, "Polarization-independent metasurface lens employing the Pancharatnam-Berry phase," Opt. Express **26**, 24835–24842 (2018).

90. M. Khorasaninejad, A. Y. Zhu, C. Roques-Carmes, W. T. Chen, J. Oh, I. Mishra, R. C. Devlin, and F. Capasso, "Polarization-Insensitive Metalenses at Visible Wavelengths," Nano Lett. **16**, 7229–7234 (2016).

91. E. Arbabi, S. M. Kamali, A. Arbabi, and A. Faraon, "Full-Stokes Imaging Polarimetry Using Dielectric Metasurfaces," ACS Photonics **5**, 3132–3140 (2018).

92. J. Kim, S. Choudhury, C. DeVault, Y. Zhao, A. V Kildishev, V. M. Shalaev, A. Alù, and A. Boltasseva, "Controlling the Polarization State of Light with Plasmonic Metal Oxide Metasurface," ACS Nano **10**, 9326–9333 (2016).

93. Z. Bomzon, V. Kleiner, and E. Hasman, "Pancharatnam–Berry phase in space-variant polarization-state manipulations with subwavelength gratings," Opt. Lett. **26**, 1424–1426 (2001).

94. W. Ye, F. Zeuner, X. Li, B. Reineke, S. He, C.-W. Qiu, J. Liu, Y. Wang, S. Zhang, and T. Zentgraf, "Spin and wavelength multiplexed nonlinear metasurface holography," Nat. Commun. **7**, 11930 (2016).

95. G. Zheng, H. Mühlenbernd, M. Kenney, G. Li, T. Zentgraf, and S. Zhang, "Metasurface holograms reaching 80% efficiency," Nat. Nanotechnol. **10**, 308–312 (2015).

96. C. Kuemin, L. Nowack, L. Bozano, N. D. Spencer, and H. Wolf, "Oriented Assembly of Gold Nanorods on the Single-Particle Level," Adv. Funct. Mater. **22**, 702–708 (2012).

97. E. Karimi, S. A. Schulz, I. De Leon, H. Qassim, J. Upham, and R. W. Boyd, "Generating optical orbital angular momentum at visible wavelengths using a plasmonic metasurface," Light Sci. Appl. **3**, e167–e167 (2014).

98. R. C. Devlin, A. Ambrosio, N. A. Rubin, J. P. B. Mueller, and F. Capasso, "Arbitrary spin-to–orbital angular momentum conversion of light," Science (1979) **358**, 896–901 (2017).

99. P. Genevet, N. Yu, F. Aieta, J. Lin, M. A. Kats, R. Blanchard, M. O. Scully, Z. Gaburro, and F. Capasso, "Ultra-thin plasmonic optical vortex plate based on phase discontinuities," Appl. Phys. Lett. **100**, 013101 (2012).

100. Y. Shen, X. Wang, Z. Xie, C. Min, X. Fu, Q. Liu, M. Gong, and X. Yuan, "Optical vortices 30 years on: OAM manipulation from topological charge to multiple singularities," Light Sci. Appl. **8**, 90 (2019).

101. L. Wang, S. Kruk, K. Koshelev, I. Kravchenko, B. Luther-Davies, and Y. Kivshar, "Nonlinear Wavefront Control with All-Dielectric Metasurfaces," Nano Lett. **18**, 3978–3984 (2018).

102. J. Lee, M. Tymchenko, C. Argyropoulos, P.-Y. Chen, F. Lu, F. Demmerle, G. Boehm, M.-C. Amann, A. Alù, and M. A. Belkin, "Giant nonlinear response from plasmonic metasurfaces coupled to intersubband transitions," Nature **511**, 65–69 (2014).

103. Y. Yang, W. Wang, A. Boulesbaa, I. I. Kravchenko, D. P. Briggs, A. Puretzky, D. Geohegan, and J. Valentine, "Nonlinear Fano-Resonant Dielectric Metasurfaces," Nano Lett. **15**, 7388–7393 (2015).

104. M. L. Solomon, J. Hu, M. Lawrence, A. García-Etxarri, and J. A. Dionne, "Enantiospecific Optical Enhancement of Chiral Sensing and Separation with Dielectric Metasurfaces," ACS Photonics **6**, 43–49 (2019).

105. D. Conteduca, I. Barth, G. Pitruzzello, C. P. Reardon, E. R. Martins, and T. F. Krauss, "Dielectric nanohole array metasurface for high-resolution near-field sensing and imaging," Nat. Commun. **12**, 3293 (2021).

106. A. S. Roberts, A. Pors, O. Albrektsen, and S. I. Bozhevolnyi, "Subwavelength Plasmonic Color Printing Protected for Ambient Use," Nano Lett. **14**, 783–787 (2014).

107. S. Yokogawa, S. P. Burgos, and H. A. Atwater, "Plasmonic Color Filters for CMOS Image Sensor Applications," Nano Lett. **12**, 4349–4354 (2012).

108. Y. Cho, Y. K. Choi, and S. H. Sohn, "Optical properties of neodymium-containing polymethylmethacrylate films for the organic light emitting diode color filter," Appl. Phys. Lett. **89**, 051102 (2006).

109. K. Kumar, H. Duan, R. S. Hegde, S. C. W. Koh, J. N. Wei, and J. K. W. Yang, "Printing colour at the optical diffraction limit," Nat. Nanotechnol. **7**, 557–561 (2012).

110. Y. Nagasaki, M. Suzuki, I. Hotta, and J. Takahara, "Control of Si-Based All-Dielectric Printing Color through Oxidation," ACS Photonics **5**, 1460–1466 (2018).

111. Y. Nagasaki, I. Hotta, M. Suzuki, and J. Takahara, "Metal-Masked Mie-Resonant Full-Color Printing for Achieving Free-Space Resolution Limit," ACS Photonics **5**, 3849–3855 (2018).

112. M. Miyata, H. Hatada, and J. Takahara, "Full-Color Subwavelength Printing with Gap-Plasmonic Optical Antennas," Nano Lett. **16**, 3166–3172 (2016).

113. R. Xu and J. Takahara, "Radiative loss control of an embedded silicon perfect absorber in the visible region," Opt. Lett. **46**, 805–808 (2021).

114. P. Genevet, F. Capasso, F. Aieta, M. Khorasaninejad, and R. Devlin, "Recent advances in planar optics: from plasmonic to dielectric metasurfaces," Optica **4**, 139–152 (2017).

115. R. Jiang, B. Li, C. Fang, and J. Wang, "Metal/Semiconductor Hybrid Nanostructures for Plasmon-Enhanced Applications," Adv. Mater. **26**, 5274–5309 (2014).

116. S. Song, Q. Chen, L. Jin, and F. Sun, "Great light absorption enhancement in a graphene photodetector integrated with a metamaterial perfect absorber," Nanoscale **5**, 9615–9619 (2013).

117. S. Jahani and Z. Jacob, "All-dielectric metamaterials," Nat. Nanotechnol. **11**, 23–36 (2016).

118. A. I. Kuznetsov, A. E. Miroshnichenko, M. L. Brongersma, Y. S. Kivshar, and B. Luk'yanchuk, "Optically resonant dielectric nanostructures," Science (1979) **354**, aag2472 (2016).

119. Y. Yang, I. I. Kravchenko, D. P. Briggs, and J. Valentine, "All-dielectric metasurface analogue of electromagnetically induced transparency," Nat. Commun. **5**, 5753 (2014).

120. Z. Wang, Z. Fu, F. Sun, C. Wang, J. Zhou, and H. Tian, "Simultaneous sensing of refractive index and temperature based on a three-cavity-coupling photonic crystal sensor," Opt. Express **27**, 26471–26482 (2019).

121. A. Vaskin, J. Bohn, K. E. Chong, T. Bucher, M. Zilk, D.-Y. Choi, D. N. Neshev, Y. S. Kivshar, T. Pertsch, and I. Staude, "Directional and Spectral Shaping of Light Emission with Mie-Resonant Silicon Nanoantenna Arrays," ACS Photonics **5**, 1359–1364 (2018).

122. G. Mie, "Beiträge zur Optik trüber Medien, speziell kolloidaler Metallösungen," Ann. Phys. **330**, 377–445 (1908).

123. M. Kerker, The Scattering of Light, and Other Electromagnetic Radiation (Academic Press), 16 (1969).

124. J. D. Jackson, Classical Electrodynamics, 3rd Edition (1998).

125. "Electromagnetic Theory," in Absorption and Scattering of Light by Small Particles (1998), 12–56.

126. "Light scattering by small particles. By H. C. van de Hulst. New York (John Wiley and Sons), London (Chapman and Hall), 1957. Pp. xiii, 470; 103 Figs.; 46 Tables. 96s," Quarterly Journal of the Royal Meteorological Society **84**, 198–199 (1958).

127. Y. H. Fu, A. I. Kuznetsov, A. E. Miroshnichenko, Y. F. Yu, and B. Luk'yanchuk, "Directional visible light scattering by silicon nanoparticles," Nat. Commun. **4**, 1527 (2013).

128. J. Cambiasso, G. Grinblat, Y. Li, A. Rakovich, E. Cortés, and S. A. Maier, "Bridging the Gap between Dielectric Nanophotonics and the Visible Regime with Effectively Lossless Gallium Phosphide Antennas," Nano Lett. **17**, 1219–1225 (2017).

129. M. Kerker, D.-S. Wang, and C. L. Giles, "Electromagnetic scattering by magnetic spheres," J. Opt. Soc. Am. **73**, 765–767 (1983).

130. X. Ming, X. Liu, L. Sun, and W. J. Padilla, "Degenerate critical coupling in all-dielectric metasurface absorbers," Opt. Express **25**, 24658–24669 (2017).

131. R. Xu and J. Takahara, "All-dielectric perfect absorber based on quadrupole modes," Opt. Lett. **46**, 3596–3599 (2021).

132. R. Xu and J. Takahara, "Radiative loss control of an embedded silicon perfect absorber in the visible region," Opt. Lett. **46**, 805–808 (2021).

133. J. Tian, H. Luo, Q. Li, X. Pei, K. Du, and M. Qiu, "Near-Infrared Super-Absorbing All-Dielectric Metasurface Based on Single-Layer Germanium Nanostructures," Laser Photon. Rev. **12**, 1800076 (2018).

134. Z.-X. Zhou, M.-J. Ye, M.-W. Yu, J.-H. Yang, K.-L. Su, C.-C. Yang, C.-Y. Lin, V. E. Babicheva, I. V Timofeev, and K.-P. Chen, "Germanium Metasurfaces with Lattice Kerker Effect in Near-Infrared Photodetectors," ACS Nano **16**, 5994–6001 (2022).

135. K. Fan, J. Y. Suen, X. Liu, and W. J. Padilla, "All-dielectric metasurface absorbers for uncooled terahertz imaging," Optica **4**, 601–604 (2017).

136. M. Decker, I. Staude, M. Falkner, J. Dominguez, D. N. Neshev, I. Brener, T. Pertsch, and Y. S. Kivshar, "High-Efficiency Dielectric Huygens' Surfaces," Adv. Opt. Mater. **3**, 813–820 (2015).

137. J. R. Piper, V. Liu, and S. Fan, "Total absorption by degenerate critical coupling," Appl. Phys. Lett. **104**, 251110 (2014).

138. J. M. Geffrin, B. García-Cámara, R. Gómez-Medina, P. Albella, L. S. Froufe-Pérez, C. Eyraud, A. Litman, R. Vaillon, F. González, M. Nieto-Vesperinas, J. J. Sáenz, and F. Moreno, "Magnetic and electric coherence in forward- and back-scattered electromagnetic waves by a single dielectric subwavelength sphere," Nat. Commun. **3**, 1171 (2012).

139. X. Ming, X. Liu, L. Sun, and W. J. Padilla, "Degenerate critical coupling in all-dielectric metasurface absorbers," Opt. Express **25**, 24658–24669 (2017).

140. J. van de Groep and A. Polman, "Designing dielectric resonators on substrates: Combining magnetic and electric resonances," Opt. Express **21**, 26285–26302 (2013).

141. P. D. Terekhov, V. E. Babicheva, K. V Baryshnikova, A. S. Shalin, A. Karabchevsky, and A. B. Evlyukhin, "Multipole analysis of dielectric metasurfaces composed of nonspherical nanoparticles and lattice invisibility effect," Phys. Rev. B **99**, 45424 (2019).

142. X. Liu, K. Fan, I. V Shadrivov, and W. J. Padilla, "Experimental realization of a terahertz all-dielectric metasurface absorber," Opt. Express **25**, 191–201 (2017).

143. C.-Y. Yang, J.-H. Yang, Z.-Y. Yang, Z.-X. Zhou, M.-G. Sun, V. E. Babicheva, and K.-P. Chen, "Nonradiating Silicon Nanoantenna Metasurfaces as Narrowband Absorbers," ACS Photonics **5**, 2596–2601 (2018).

144. J. Tian, H. Luo, Q. Li, X. Pei, K. Du, and M. Qiu, "Near-Infrared Super-Absorbing All-Dielectric Metasurface Based on Single-Layer Germanium Nanostructures," Laser Photon. Rev. **12**, 1800076 (2018).

145. K. Fan, J. Y. Suen, X. Liu, and W. J. Padilla, "All-dielectric metasurface absorbers for uncooled terahertz imaging," Optica **4**, 601–604 (2017).

146. J. Y. Suen, K. Fan, and W. J. Padilla, "A Zero-Rank, Maximum Nullity Perfect Electromagnetic Wave Absorber," Adv. Opt. Mater. **7**, 1801632 (2019).

147. R. Xu and J. Takahara, "Radiative loss control of an embedded silicon perfect absorber in the visible region," Opt. Lett. **46**, 805–808 (2021).

148. E. M. Purcell, H. C. Torrey, and R. V Pound, "Resonance Absorption by Nuclear Magnetic Moments in a Solid," Phys. Rev. **69**, 37–38 (1946).

149. E. T. Jaynes and F. W. Cummings, "Comparison of quantum and semiclassical radiation theories with application to the beam maser," Proc. IEEE **51**, 89–109 (1963).

150. M. Qin, S. Xiao, W. Liu, M. Ouyang, T. Yu, T. Wang, and Q. Liao, "Strong coupling between excitons and magnetic dipole quasi-bound states in the continuum in WS_2-TiO_2 hybrid metasurfaces," Opt. Express **29**, 18026–18036 (2021).

151. S. Lepeshov, A. Krasnok, and A. Alù, "Enhanced excitation and emission from 2D transition metal dichalcogenides with all-dielectric nanoantennas," Nanotech. **30**, 254004 (2019).

152. A. Krasnok, M. Caldarola, N. Bonod, and A. Alú, "Spectroscopy and Biosensing with Optically Resonant Dielectric Nanostructures," Adv. Opt. Mater. **6**, 1701094 (2018).

153. J. Sun, Y. Li, H. Hu, W. Chen, D. Zheng, S. Zhang, and H. Xu, "Strong plasmon–exciton coupling in transition metal dichalcogenides and plasmonic nanostructures," Nanoscale **13**, 4408–4419 (2021).

154. M. Qin, S. Xiao, W. Liu, M. Ouyang, T. Yu, T. Wang, and Q. Liao, "Strong coupling between excitons and magnetic dipole quasi-bound states in the continuum in WS_2-TiO_2 hybrid metasurfaces," Opt. Express **29**, 18026–18036 (2021).

155. K. Kinoshita, R. Moriya, M. Onodera, Y. Wakafuji, S. Masubuchi, K. Watanabe, T. Taniguchi, and T. Machida, "Dry release transfer of graphene and few-layer h-BN by utilizing thermoplasticity of polypropylene carbonate," NPJ 2D Mater. Appl. **3**, 22 (2019).

156. C. Cong, J. Shang, X. Wu, B. Cao, N. Peimyoo, C. Qiu, L. Sun, and T. Yu, "Synthesis and Optical Properties of Large-Area Single-Crystalline 2D Semiconductor WS2 Monolayer from Chemical Vapor Deposition," Adv. Opt. Mater. **2**, 131–136 (2014).

157. A. Gurarslan, Y. Yu, L. Su, Y. Yu, F. Suarez, S. Yao, Y. Zhu, M. Ozturk, Y. Zhang, and L. Cao, "Surface-Energy-Assisted Perfect Transfer of Centimeter-Scale Monolayer and Few-Layer MoS2 Films onto Arbitrary Substrates," ACS Nano **8**, 11522–11528 (2014).

158. H. Zeng, G.-B. Liu, J. Dai, Y. Yan, B. Zhu, R. He, L. Xie, S. Xu, X. Chen, W. Yao, and X. Cui, "Optical signature of symmetry variations and spin-valley coupling in atomically thin tungsten dichalcogenides," Sci. Rep. **3**, 1608 (2013).

159. J. Langer, D. Jimenez de Aberasturi, J. Aizpurua, R. A. Alvarez-Puebla, B. Auguié, J. J. Baumberg, G. C. Bazan, S. E. J. Bell, A. Boisen, A. G. Brolo, J. Choo, D. Cialla-May, V. Deckert, L. Fabris, K. Faulds, F. J. García de Abajo, R. Goodacre, D. Graham, A. J. Haes, C. L. Haynes, C. Huck, T. Itoh, M. Käll, J. Kneipp, N. A. Kotov, H. Kuang, E. C. Le Ru, H. K. Lee, J.-F. Li, X. Y. Ling, S. A. Maier, T. Mayerhöfer, M. Moskovits, K. Murakoshi, J.-M. Nam, S. Nie, Y. Ozaki, I. Pastoriza-Santos, J. Perez-Juste, J. Popp, A. Pucci, S. Reich, B. Ren, G. C. Schatz, T. Shegai, S. Schlücker, L.-L. Tay, K. G. Thomas, Z.-Q. Tian, R. P. Van Duyne, T. Vo-Dinh, Y. Wang, K. A. Willets, C. Xu, H. Xu, Y. Xu, Y. S. Yamamoto, B. Zhao, and L. M. Liz-Marzán, "Present and Future of Surface-Enhanced Raman Scattering," ACS Nano **14**, 28–117 (2020).

160. K. Frizyuk, M. Hasan, A. Krasnok, A. Alú, and M. Petrov, "Enhancement of Raman scattering in dielectric nanostructures with electric and magnetic Mie resonances," Phys. Rev. B **97**, 85414 (2018).

161. Zhao, W., Wang, S., Liu, B., Verzhbitskiy, I., Li, S., Giustiniano, F., Kozawa, D., Loh, K.P., Matsuda, K., Okamoto, K., Oulton, R.F. and Eda, G., "Exciton–Plasmon Coupling and

Electromagnetically Induced Transparency in Monolayer Semiconductors Hybridized with Ag Nanoparticles". Adv. Mater. **28**, 2709-2715 (2016).

162. P. A. Dmitriev, D. G. Baranov, V. A. Milichko, S. V Makarov, I. S. Mukhin, A. K. Samusev, A. E. Krasnok, P. A. Belov, and Y. S. Kivshar, "Resonant Raman scattering from silicon nanoparticles enhanced by magnetic response," Nanoscale **8**, 9721–9726 (2016).

163. A. Krasnok, S. Lepeshov, and A. Alú, "Nanophotonics with 2D transition metal dichalcogenides [Invited]," Opt. Express **26**, 15972–15994 (2018).

164. D. M. Coles, R. T. Grant, D. G. Lidzey, C. Clark, and P. G. Lagoudakis, "Imaging the polariton relaxation bottleneck in strongly coupled organic semiconductor microcavities," Phys. Rev. B **88**, 121303 (2013).

165. V. Kravtsov, E. Khestanova, F. A. Benimetskiy, T. Ivanova, A. K. Samusev, I. S. Sinev, D. Pidgayko, A. M. Mozharov, I. S. Mukhin, M. S. Lozhkin, Y. V Kapitonov, A. S. Brichkin, V. D. Kulakovskii, I. A. Shelykh, A. I. Tartakovskii, P. M. Walker, M. S. Skolnick, D. N. Krizhanovskii, and I. V Iorsh, "Nonlinear polaritons in a monolayer semiconductor coupled to optical bound states in the continuum," Light Sci. Appl. **9**, 56 (2020).

166. D. Sanvitto and S. Kéna-Cohen, "The road towards polaritonic devices," Nat. Mater. **15**, 1061–1073 (2016).

167. D. M. Coles, P. Michetti, C. Clark, A. M. Adawi, and D. G. Lidzey, "Temperature dependence of the upper-branch polariton population in an organic semiconductor microcavity," Phys. Rev. B **84**, 205214 (2011).

168. S. Liu, F. Deng, W. Zhuang, X. He, H. Huang, J.-D. Chen, H. Pang, and S. Lan, "Optical Introduction and Manipulation of Plasmon–Exciton–Trion Coupling in a Si/WS_2/Au Nanocavity," ACS Nano **16**, 14390–14401 (2022).

169. X. Wang, M. T. Pettes, Y. Wang, J.-X. Zhu, R. Dhall, C. Song, A. C. Jones, J. Ciston, and J. Yoo, "Enhanced Exciton-to-Trion Conversion by Proton Irradiation of Atomically Thin WS_2," Nano Lett. **23**, 3754–3761 (2023).

170. R. Sebait, C. Biswas, B. Song, C. Seo, and Y. H. Lee, "Identifying Defect-Induced Trion in Monolayer WS_2 via Carrier Screening Engineering," ACS Nano **15**, 2849–2857 (2021).

171. R. P. A. Emmanuele, M. Sich, O. Kyriienko, V. Shahnazaryan, F. Withers, A. Catanzaro, P. M. Walker, F. A. Benimetskiy, M. S. Skolnick, A. I. Tartakovskii, I. A. Shelykh, and D. N. Krizhanovskii, "Highly nonlinear trion-polaritons in a monolayer semiconductor," Nat. Commun. **11**, 3589 (2020).

Acknowledgement

Time has passed quickly, and the three and a half years of my doctoral study at Osaka University have gone by in a flash. During this period, I have received tremendous help, encouragement, and support from many people. I would like to express my heartfelt gratitude to all those who have cared for me, supported me, and accompanied my growth.

First and foremost, I wish to express my deepest appreciation to my supervisor, Professor Takahara Junichi. His excellent research environment, thoughtful guidance, and continuous patience have been invaluable to me. His pursuit of precision, his passion for scientific research, and his rigorous and dedicated attitude toward work have profoundly influenced me. I will carry his teachings with me into my future academic career and personal life. Here, I offer my sincere respect and gratitude once again.

I was supported by the China Scholarship Council (No. 202204910108). I am truly grateful for this support, which made it possible for me to study at Osaka University.

I would like to thank all those who contributed to my research. I am grateful to Dr. Xu Rongyang for his substantial assistance in experiments, his detailed guidance has benefited me greatly. My sincere thanks go to Mr. Kimino Kazuya for his insightful advice and support in metasurface fabrication. I also appreciate the help from Dr. Takuya Iwasaki at the National Institute for Materials Science (NIMS) regarding the transferring process, and from Professor Furube Akihiro of Tokushima University for his support in ultrafast microscopy measurements. I am also thankful to the laboratory secretaries and junior members for their support in maintaining the laboratory and for their help in daily life.

My gratitude extends to Professor Prabhat Verma, Professor Kazuyuki Sakamoto in our department, and Professor Koichi Okamoto of Osaka Metropolitan University, who served as members of my dissertation committee. Their guidance and valuable comments have been of great importance to the completion of this thesis.

I would also like to express my thanks to who have supported me, including my boyfriend, Su Yixiao, my parents, my dearest friends Hu Anqi, Li Yangjie, Zhou Yuxin, Xi Heqi, and Shi Liyu, for standing by me over the past three years.

Finally, I hope that our future path will be smooth and that I could find and persist in a direction where I truly belong.

List of Publications

Journal papers

1. **D. Chen** and J. Takahara, "Enhancement of excitonic absorption in WS_2 mediated by Huygens Si metasurfaces," Opt. Lett. 50, 4246-4249 (2025).
2. **D. Chen** and J. Takahara, “Demonstration of Miexciton: Enhancement of Light-matter Interaction in Monolayer WS_2 on Si Metasurface.” Opt. Lett. 50, 7508-7511 (2025).
3. **D. Chen**, A. Furube, J. Takahara, “Carrier Dynamics in a Miexciton by Ultrafast Microscopy. (tentative)” (in preparation).

Journal papers (not used in the thesis)

1. R. Xu*, **D. Chen***, Junichi Takahara, “Perfect absorption of violet light enabled by rotated Mie resonators.” J. Appl. Phys. 135, 243109 (2024).

* Equally contributed.

International Conferences

1. **D. Chen**, J. Takahara, “Absorption Enhancement of WS_2 with All-dielectric Metasurface Based on Mie Resonance and Degenerate Critical Coupling,” JSAP-Optica Joint Symposia, The 84th JSAP Autumn Meeting, 20a-A602-4, in Kumamoto-jo Hall, Kumamoto, Japan, September 20 (2023). (oral)
2. **D. Chen**, J. Takahara, “Absorption Enhancement of 2D Transition Metal Dichalcogenides on Silicon Metasurface by Degenerate Critical Coupling”, International Conference on Nanoscience and Nanotechnology (ICNN) 2024, OPTICS & PHOTONICS International Congress, ICNN5-02, in Pacifico Yokohama, Yokohama, Japan, April 23 (2024). (oral)
3. **D. Chen**, J. Takahara, “Absorption Enhancement of Exciton of WS_2 by Silicon Metasurface Based on Degenerate Critical Coupling”, 14th International Conference on Metamaterials, Photonic Crystals and Plasmonics (META2024), Session 1A31, SP22. 2D Materials and Plasmonics, in Toyama International Conference Center, Toyama, Japan, July 16 (2024). (oral)
4. **D. Chen**, J. Takahara, “Absorption Enhancement of Excitons in WS_2 by Silicon Huygens’ Metasurface”, JSAP-Optica Joint Symposia, The 85th JSAP Autumn Meeting, 17a-A35-2, in TOKI MESSE Niigata Convention Center, Niigata, Japan, September 17 (2024). (oral)
5. **D. Chen**, J. Takahara, “Absorption Enhancement of WS_2 by Silicon Huygens’ Metasurface Based on Multiple Coupling”, The 11th International Conference on Surface Plasmon Photonics

(SPP11), C000081, in Hitotsubashi Hall, National Center of Sciences Building, Tokyo, Japan, May 19 (2025). (poster)

Domestic conferences

1. J. Takahara, **D. Chen**, “Photothermal Effects and Hybridized 2D-Nanomaterials on Dielectric Metasurface”, Optics & Photonics Japan OSJ, 28pBS3, in 3F Sunrise Build II, Shinjuku, Tokyo, November 28 (2023). (oral)
2. **D. Chen**, J. Takahara, “Absorption Enhancement of WS_2 with All-dielectric Metasurface Based on Mie Resonance and Degenerate Critical Coupling”, Joint Seminar of Osaka University & University of Chinese Academy of Sciences, in Osaka University Icho Kaikan, Suita, Osaka, Japan, July 8 (2024). (poster)
3. **D. Chen**, J. Takahara, “Absorption Enhancement of WS_2 Exciton by Silicon Metasurface Based on Intermediate Coupling” 日本学術会議国際光デー記念シンポジウム， 18， 日本学術会議講堂，港区，東京都，日本, 7 月 7 日 (2025). (poster)